

CO₂ Foam Dynamics During CO₂ Enhanced Oil Recovery and CO₂ Storage

Aleksandra Magdalena Sæle

Thesis for the degree of Philosophiae Doctor (PhD)
University of Bergen, Norway
2023

UNIVERSITY OF BERGEN



CO₂ Foam Dynamics During CO₂ Enhanced Oil Recovery and CO₂ Storage

Aleksandra Magdalena Sæle



Thesis for the degree of Philosophiae Doctor (PhD)
at the University of Bergen

Date of defense: 09.10.2023

© Copyright Aleksandra Magdalena Sæle

The material in this publication is covered by the provisions of the Copyright Act.

Year: 2023

Title: CO2 Foam Dynamics During CO2 Enhanced Oil Recovery and CO2 Storage

Name: Aleksandra Magdalena Sæle

Print: Skipnes Kommunikasjon / University of Bergen

Acknowledgments

I wish to acknowledge the Research Council of Norway PETROMAKS2 program for financial support for the project “Optimizing CO₂ Foam EOR Mobility Control for Field Pilots”.

I want to express my gratitude to my supervisors Dr. Zachary Paul Alcorn, Prof. Arne Graue, and Prof. Geir Ermland at the Department of Physics and Technology at the University of Bergen, for the opportunity to work on an exciting research project. Thank you for the guidance, support, and valuable discussions. I would also like to thank Dr. Bergit Brattekkås and Dr. Jacquelin Cobos for experimental guidance, collaboration and for willingly sharing your experience and knowledge.

I want to thank my fellow students and colleagues in the Reservoir Physics Group for a memorable time at the University of Bergen. Thank you for many interesting discussions, daily lunch breaks, and a great time during conferences, seminars, and courses. Also, thanks to all the master students I got the opportunity to work with for collaboration and a fun time in the lab.

Finally, I want to express my deepest appreciation to my family for their endless love, inspiration, and encouragement. A special thanks to my husband, Chris Joakim, for his support, incredible patience, and for always lifting my spirits.

Bergen, June 2023

Aleksandra M. Sæle

Summary

The ever-growing population, increasing prosperity, and economic growth leads to increased energy demand. The combustion of fossil fuels accounts for 80% of the global energy mix, making it a valuable energy source. The global population is expected to increase by two billion in the next 30 years, and energy demand is predicted to increase by 1% a year to 2030. This rapid growth and increasing demand indicate that fossil fuels will remain important for society in the coming years. Consequently, humanity is threatened by human-induced climate change, with energy production accounting for three-quarters of global greenhouse gas emissions. A rapid change in the energy system is needed to supply the world with sufficient energy and mitigate climate change.

Carbon capture and storage (CCS) is an important measure to limit global warming and achieve the climate goals stated in the Paris Agreement. The technology includes capturing CO₂ from industrial and energy-related sources and permanently storing CO₂ isolated from the atmosphere. Large-scale implementation of CCS currently faces economic barriers. Utilization of CO₂ as a commodity can provide a financial incentive for large-scale CCS. Using CO₂ for enhanced oil recovery (EOR) is a well-established and promising technology that provides economic revenue while increasing oil production.

CO₂ EOR has been performed for over 50 years and is a proven technology contributing to the ongoing energy transition. However, the effectiveness of this technology is limited by challenges associated with high CO₂ mobility and reservoir heterogeneity. Foaming CO₂ is a technological solution where CO₂ and a foaming solution are mixed to reduce CO₂ mobility and improve sweep efficiency in EOR and CO₂ storage processes. Previous foam field tests have been reported as technical successes with evidence of foam generation, improved sweep efficiency, and enhanced oil recovery. Others were deemed unsuccessful due to injectivity problems and limited foam propagation in the reservoir. Thus, a more thorough understanding of foam dynamics, strength, stability, and size-dependent displacement mechanisms is needed to advance the technology.

This thesis is based upon six scientific papers, which together constitute a multi-scale study of CO₂ foam for mobility control for EOR and associated CO₂ storage. The study provides insight into the fundamental concepts of foam, investigates the influence of various factors, such as the presence of oil and foaming solution concentration, on CO₂ foam behavior, and evaluates the effectiveness of CO₂ foam in improving oil recovery and increasing CO₂ storage capacity.

Paper 1 presents a multi-scale investigation of CO₂ foam dynamics at reservoir conditions. High-pressure pore-scale experiments revealed foam generation and coalescence processes of CO₂ foam and provided real-time insights on *in-situ* foam behavior observed at the core-scale. Hybrid nanoparticle-surfactant foam for CO₂ mobility control in CO₂ EOR and CO₂ storage processes was investigated and compared to surfactant- and nanoparticle-based foams. In addition, the effect of residual oil on foam generation, strength, and stability was studied.

Paper 2 reveals pore-level foam coarsening and anti-coarsening mechanisms for a static CO₂ foam in a realistic pore structure at reservoir pressure. Ostwald ripening of CO₂ foam was studied using lab-on-a-chip technology. The effect of foaming solution on foam stability was evaluated. Foam generated with a hybrid nanoparticle-surfactant solution was compared to foam stabilized by only surfactant or nanoparticles.

Paper 3 extends on the work presented in Paper 1 and evaluates the efficiency of hybrid nanoparticle-surfactant foam for CO₂ mobility control at elevated salinities. A multi-scale approach spanning from pore- to core-scale was implemented to study foam generation and stability at harsh reservoir conditions. Displacement efficiency of hybrid-, surfactant- and nanoparticle-based foam for CO₂ storage applications was evaluated.

Paper 4 investigates the ability of CO₂ foam to increase oil recovery and associated CO₂ storage potential in experiments that deploy field-scale injection strategies. The efficiency of CO₂ foam was compared to pure CO₂ injection and water-alternating gas, a common CO₂ mobility control method. The impact of surfactant concentration on foam efficiency was investigated. Additionally, the effect of oil on CO₂ foam generation and stability was studied.

Paper 5 extends the work presented in Paper 4 and shows CO₂ foam for mobility control in different rock types at reservoir conditions. Foam generation, strength, and stability in sandstone and two carbonate rocks were evaluated. In addition, the effect of injection rate and residual oil on foam generation and displacement efficiency was investigated. The results provided valuable input data for foam modeling and numerical simulations.

Paper 6 presents a multi-scale experimental and numerical investigation of CO₂ foam generation, strength, and propagation during surfactant-alternating gas injection at reservoir conditions. Core-scale experimental results captured CO₂ foam behavior during surfactant-alternating gas injection and shed light on field-scale CO₂ foam flow in the near-wellbore region. A radial reservoir simulation model investigated foam propagation and foam behavior during a recently completed field pilot.

Sammendrag

Den stadig voksende befolkningen, økende velstand og økonomisk vekst fører til økende etterspørsel etter energi. Forbrenning av fossile brensler står for 80% av den globale energi produksjonen, noe som gjør det til en verdifull energikilde. Det forventes at verdensbefolkningen skal øke med to milliarder i løpet av de neste 30 årene, og energietterspørselen forventes å øke med 1% per år frem til 2030. Denne raske veksten og økende etterspørselen indikerer at fossile brensler forblir viktige for samfunnet i de kommende årene. Som en konsekvens trues menneskeheten av menneskeskapte klimaendringer, der energiproduksjonen står for tre fjerdedeler av de globale utslippene av klimagasser. En rask endring i energisystemet er nødvendig for å forsyne verden med tilstrekkelig energi og redusere klimaendringer.

Karbonfangst og -lagring (carbon capture and storage, CCS) er et viktig tiltak for å begrense global oppvarming og oppnå klimamålene erklært i Parisavtalen. Denne teknologien innebærer å fange CO₂ fra industrielle og energirelaterte kilder og permanent lagre CO₂ isolert fra atmosfæren. Storskala implementering av CCS står for øyeblikket over økonomiske utfordringer. Bruk av CO₂ som et produkt kan gi økonomisk støtte for storskala CCS. Bruk av CO₂ for økt olje utvinning (enhanced oil recovery, EOR) er en veletablert og lovende teknologi som bidrar til økt profitt og samtidig økt oljeproduksjon.

CO₂ EOR har blitt utført i over 50 år og er en velkjent teknologi som bidrar til den pågående energiomstillingen. Imidlertid er effektiviteten til denne teknologien begrenset av utfordringer knyttet til høy CO₂ mobilitet og reservoarheterogenitet. CO₂ skum er en teknologisk løsning hvor CO₂ og en surfaktantløsning blandes for å redusere mobiliteten til CO₂ og forbedre fortregningen i EOR og CO₂ lagring prosesser. Tidligere CO₂ skum testpiloter på feltskala har blitt rapportert som teknisk vellykket med bevis på skumdannelse, forbedret fortregningsevne og økt oljeutvinning. Andre tester derimot ble ansett som mislykket på grunn av injeksjonsproblemer og dårlig skumpropagering i reservoaret. Derfor er det et behov for en grundigere forståelse av skumdynamikk, styrke, stabilitet og størrelsesavhengige fortregningsmekanismer for å videreutvikle teknologien.

Denne avhandlingen er basert på seks vitenskapelige artikler som til sammen utgjør en flerskala studie av CO₂ skum for mobilitetskontroll for EOR og CO₂ lagring. Studien gir innsikt i grunnleggende konsepter innen skum, undersøker innflytelse av ulike faktorer, som tilstedeværelse av olje og konsentrasjon av surfaktantløsning, på CO₂ skum oppførsel og evaluerer effektiviteten av CO₂ skum for å forbedre oljeutvinning og øke CO₂ lagringskapasitet.

Artikkel 1 presenterer en flerskala undersøkelse av CO₂-skumdynamikk under reservoarforhold. Høytrykks pore-skala eksperimenter viste dannelses- og destabiliseringsprosesser av CO₂ skum og forbedret forståelse av skumatferd observert på kjerne-skala. Hybrid nanopartikkel-surfaktant-skum for CO₂ mobilitetskontroll i CO₂ EOR og CO₂ lagringsprosesser ble undersøkt og sammenlignet med skum basert på kun surfaktanter og nanopartikler. I tillegg ble effekten av residuell olje på skumdannelse, styrke og stabilitet studert.

Artikkel 2 avslørte pore-skala mekanismer bak skumforgroving og anti-forgroving for statisk CO₂ skum i en realistisk porestruktur ved reservoartrykk. Ostwald-ripening av skum ble undersøkt ved hjelp av lab-on-a-chip-teknologi. Effekten av surfaktantløsning på skumstabilitet ble evaluert. Skum dannet ved å bruke en hybrid nanopartikkel-surfaktant-løsning ble sammenlignet med skum stabilisert av bare surfaktant eller nanopartikler.

Artikkel 3 bygger videre på arbeidet presentert i Artikkel 1 og evaluerer effekten av hybrid nanopartikkel-surfaktant-skum på CO₂ mobilitetskontroll ved høye saltinnhold. En flerskala tilnærming som spenner fra pore- til kjerne-skala ble gjennomført for å studere skumdannelse og skumstabilitet under krevende reservoarforhold. Fortrengningsevnen til hybrid-, surfaktant- og nanopartikkelbasert skum for CO₂ lagring ble evaluert.

Artikkel 4 undersøker CO₂ skums evne til å øke oljeutvinning og tilhørende CO₂ lagringspotensialet i eksperimenter som representerer feltskala injeksjonsstrategier. Effekt av CO₂ skum ble sammenlignet med ren CO₂ injeksjon og vekselvis vann og gassinjeksjon (WAG), en vanlig metode for CO₂ mobilitetskontroll. Påvirkning av

surfaktantkonsentrasjonen på skumeffektivitet ble undersøkt. I tillegg ble effekten av olje på CO₂ skumdannelse og stabilitet studert.

Artikkel 5 bygger videre på arbeidet presentert i Artikkel 4 og viser CO₂ skum for mobilitetskontroll i ulike bergartstyper under reservoarforhold. Skumdannelse, styrke og stabilitet i sandstein og to karbonatbergarter ble evaluert. I tillegg ble effekten av injeksjonshastighet og tilstedeværelsen av residuell olje på skumdannelse og fortrenningsevne undersøkt. Resultatene ga verdifulle inndata for skummodellering og numeriske simuleringer.

Artikkel 6 presenterer en flerskala eksperimentell og numerisk undersøkelse av CO₂ skumdannelse, styrke og propagering under vekselvis surfaktant- og gassinjeksjon (SAG) under reservoarforhold. Eksperimentelle resultater på kjerne-skala fanget CO₂ skumatferd under SAG injeksjoner og kastet lys over CO₂ skumstrømning på feltskala i nærbrønnområdet. En radial reservoarmodell ble brukt for numerisk undersøkelse av skumpropagering og skumatferd under en nylig gjennomført feltpilot.

List of Publications

1. Alcorn, Z. P., Føyen, T., Gauteplass, J., Benali, B., **Soyke, A.**, & Fernø, M. (2020). Pore-and Core-Scale Insights of Nanoparticle-Stabilized Foam for CO₂-Enhanced Oil Recovery. *Nanomaterials*, 10(10). doi:10.3390/nano10101917
2. Benali, B., **Sæle, A.**, Liu, N., Fernø, M. A., Alcorn, Z. P. (2023). Pore-level Ostwald Ripening of CO₂ Foams at Reservoir Pressure. Accepted for publication in *Transport in Porous Media*, June 2023
3. **Soyke, A.**, Benali, B., Føyen, T., & Alcorn, Z. P. (2021). Hybrid Nanoparticle-Surfactant Stabilized Foams for CO₂ Mobility Control at Elevated Salinities. Paper presented at the IOR 2021 – 21st European Symposium on Improved Oil Recovery, April 2021. doi:10.3997/2214-4609.202133110
4. **Sæle, A.**, Graue, A., & Alcorn, Z. P. (2022). Unsteady-state CO₂ foam injection for increasing enhanced oil recovery and carbon storage potential. *Advances in Geo-Energy Research*, 6(6), 472-481. doi:10.46690/ager.2022.06.04
5. **Sæle, A. M.**, Graue, A., & Alcorn, Z. P. (2023). The Effect of Rock Type on CO₂ Foam for CO₂ EOR and CO₂ Storage. Paper presented at the International Petroleum Technology Conference, Bangkok, Thailand. March 2023. doi: 10.2523/iptc-22918-ms
6. Alcorn, Z. P., **Sæle, A.**, Karakas, M., & Graue, A. (2022). Unsteady-State CO₂ Foam Generation and Propagation: Laboratory and Field Insights. *Energies*, 15(18), 6551. doi:10.3390/en15186551

Additional Scientific Contributions

Hybrid Nanoparticle-Surfactant Stabilized Foams for CO₂ Mobility Control at Elevated Salinities. Poster presentation at the *IOR 2021 21st European Symposium on Improved Oil Recovery*, Virtual Conference. April 2021

CO₂ Foam for EOR and CO₂ Storage. Poster presentation at *Energy Norway 2022*, Stavanger, Norway. April 2022

The Effect of Rock Type on CO₂ Foam for CO₂ EOR and CO₂ Storage. Oral presentation at *International Petroleum Technology Conference (IPTC) 2023*, Bangkok, Thailand. March 2023

Alcorn, Z.P., Halsøy, H., **Sæle, A.**, Brattekkås, B., Graue, A. (2023). CO₂ Foam Flow Dynamics at Reservoir Conditions. Paper SPE-214973-MS, To be presented at the *SPE Annual Technical Conference and Exhibition*, San Antonio, Texas, US. October 2023

Table of Contents

Acknowledgments	3
Summary	5
Sammendrag	8
List of Publications	11
Additional Scientific Contributions	12
Table of Contents	13
1. Introduction and Theory	13
1.1 The Dual Challenge	15
1.2 Carbon Capture, Utilization and Storage	16
1.3 CO ₂ for Enhanced Oil Recovery and CO ₂ Storage	16
1.4 CO ₂ Foam Fundamentals	19
1.5 Real-Time Foam Visualization	25
1.6 CO ₂ Foam Field Pilot	27
2. Results and Discussion	31
2.1 CO ₂ Foam Generation and Destabilization	31
2.2 The Effect of Key Reservoir Properties on Foam	42
2.3 Nanoparticle-Stabilized Foams	55
2.4 CO ₂ Foam for EOR	63
2.5 Foam-Assisted CO ₂ Storage	69
3. Conclusions	79
4. Future Perspectives	81

Nomenclature	82
Abbreviations	83
References	84
Scientific Papers	93

1. Introduction and Theory

1.1 The Dual Challenge

Society today faces two severe challenges: the energy challenge, where the demand for more and cleaner energy is constantly increasing, and climate change, the most severe challenge in the 21st century. The ever-growing population, increased prosperity, and improved standards of living result in increasing energy demand. The total energy consumption in 2021 grew by 5.2%, the largest increase in history, and the energy demand is expected to increase by 1% a year to 2030 (IEA, 2022). Today, 770 million people live without electricity, and 2.6 billion people use insufficient cooking facilities that are polluting and harmful (IEA, 2022). Fossil fuels account for 80% of the energy supply, and 30% comes from oil combustion. The increasing demand dictates that fossil fuels will remain an important energy source in the following decades due to their crucial role in society, especially in the transportation and industrial sectors. In addition, fossil fuels have a high energy density and are easily transported and stored, making them cost efficient and convenient energy sources until cleaner renewable energy alternatives can fully meet the increasing global energy demand (IEA, 2020).

Consequently, the average temperature on Earth is increasing. There are changes in precipitation, rising sea levels, and shrinking mountain glaciers. The amount of CO₂ in the atmosphere is the highest in history (IPCC, 2018). Energy production is the largest driver of climate change and accounts for around 75% of global greenhouse gas emissions (Ritchie et al., 2022). To mitigate climate change and achieve the goals stated in the Paris Agreement while providing the world with sufficient energy, a rapid change in the energy system is needed. This change includes a shift towards renewable and sustainable energy, decarbonizing the energy systems, and permanent carbon sequestration.

Carbon capture, utilization, and storage (CCUS) is a promising technology to meet these challenges. In this work, utilization of CO₂ foam technology for enhanced oil recovery (EOR) and associated carbon storage was studied. This work aimed to gain a more thorough understanding of foam systems at reservoir conditions and improve the

understanding of foam displacement and trapping mechanisms to improve predictive modeling of CO₂ foam.

1.2 Carbon Capture, Utilization and Storage

Carbon capture, utilization, and storage (CCUS) is a viable technology to solve the dual challenge. CCUS involves capturing CO₂ from a source point, utilizing it for production processes, and injecting it into underground geological formations for permanent carbon sequestration. The use of CO₂ for EOR is a well-established technology, but new utilization pathways like CO₂-based chemical production, fuel production, and construction materials production are under development (Hepburn et al., 2019). The utilization of CO₂ as a commodity provides an economic incentive for large-scale carbon capture and storage (CCS), essential to mitigate climate change and achieve a net-zero carbon emission society (IPCC, 2018). Furthermore, CO₂ EOR helps meet the growing energy demand and provides energy security while transitioning towards new, cleaner energy solutions.

1.3 CO₂ for Enhanced Oil Recovery and CO₂ Storage

The injection of CO₂ for enhanced oil recovery (EOR) and CO₂ storage is a proven technology that has been successfully implemented for several decades (Eiken et al., 2011; Taber et al., 1997). CO₂ is a highly effective solvent for EOR applications due to its physical properties and ability to mix with oil. Physical properties of CO₂, like density and viscosity, vary with temperature and pressure. At reservoir conditions, CO₂ is typically in a supercritical or dense state, with higher density and viscosity compared to CO₂ gas and other compressed gases (Bachu et al., 2005). Injection of supercritical CO₂ alleviates gravity segregation and viscous fingering. Moreover, CO₂ is miscible with most crude oils, can swell the oil, and reduce its viscosity, leading to improved microscopic sweep efficiency (Lee & Kam, 2013).

Despite several benefits of CO₂ injection for EOR, the effectiveness of CO₂ EOR and CO₂ storage is limited by challenges associated with high CO₂ mobility and reservoir

heterogeneity (**Figure 1.1**) (Hanssen et al., 1994). The density and viscosity differences between CO₂ and other reservoir fluids can cause flow instabilities such as gravitational segregation and viscous fingering, resulting in poor sweep efficiency (Talebian et al., 2014). CO₂ injection into heterogeneous reservoirs can lead to gas channeling through high-permeability zones, resulting in early CO₂ breakthrough, reduced incremental oil recovery, and limited CO₂ storage capacity (Hanssen et al., 1994; Mo et al., 2012).

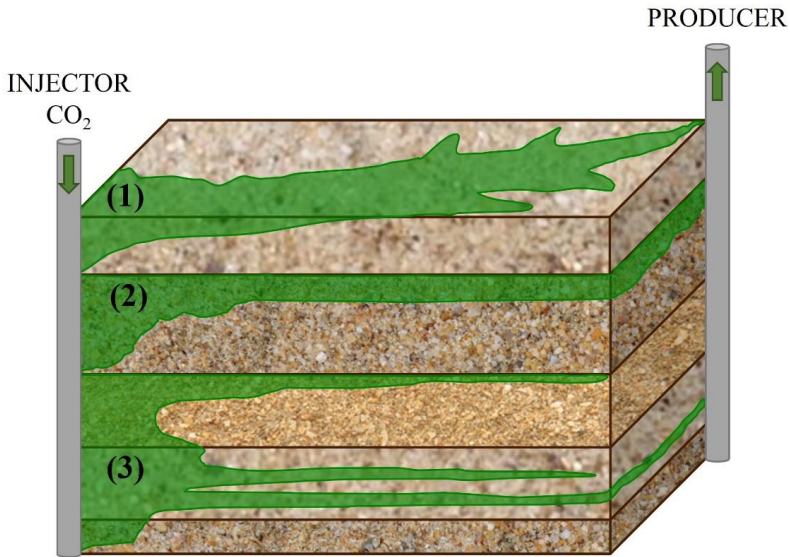


Figure 1.1. Flow instabilities during CO₂ injection associated with high CO₂ mobility and reservoir heterogeneity: (1) viscous fingering, (2) gravitational segregation and (3) gas channeling. These challenges lead to early CO₂ breakthrough, poor sweep efficiency, reduced oil recovery and limited CO₂ storage capacity. Modified from Hanssen et al. (1994).

Common CO₂ mobility control methods, including direct CO₂ thickeners, water-alternating gas (WAG), and CO₂ foams can mitigate the flow instabilities (Enick et al., 2012). CO₂ thickeners can improve microscopic displacement efficiency by increasing CO₂ viscosity, but their use is limited by drawbacks such as chemical retention and toxicity, as well as high costs (Pal et al., 2022). WAG is a common method where water and gas are injected into the reservoir in alternating slugs to reduce the relative permeability of the gas, delay gas breakthrough and improve volumetric sweep efficiency. However, gravitational segregation and water shielding effects at high water

saturations during WAG can significantly reduce displacement efficiency (Massarweh & Abushaikha, 2021). CO₂ foam is a promising and cost-efficient technology to improve CO₂ mobility control and prevent flow instabilities during CO₂ EOR and storage processes (Rossen, 1996; Talebian et al., 2014).

1.4 CO₂ Foam Fundamentals

Foaming CO₂ is an effective method to improve displacement efficiency for CO₂ EOR and CO₂ storage processes. Foam increases the gas viscosity by several orders of magnitude, thereby decreasing gas mobility and mitigating flow instabilities (Talebian et al., 2014). In addition, foam may block high-permeable layers and divert flow into un-swept regions of a reservoir (Prud'homme & Khan, 1996). Understanding the fundamental concepts of CO₂ foam is essential to advance CO₂ foam technology.

Foam Characteristics

Foam is a two-phase dispersion where the discontinuous gas phase is separated by continuous, thin liquid films called lamella (**Figure 1.2**) (Falls et al., 1989). Lamellae are thermodynamically unstable and easily collapse. Therefore a foaming agent is required to prolong the lifetime of the foam (Schramm & Wassmuth, 1994).

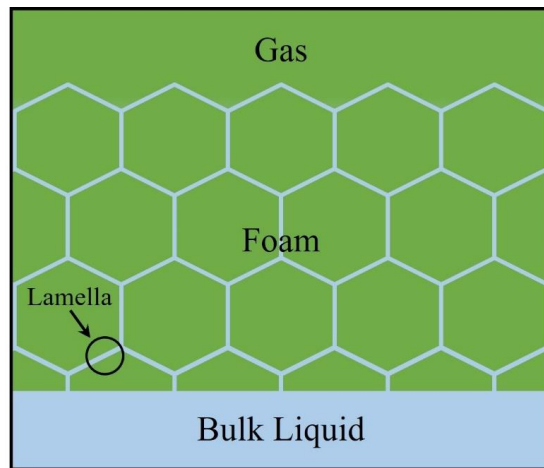


Figure 1.2. Illustration of foam system where gas (green) is dispersed in continuous liquid phase (blue) and gas bubbles are separated by thin liquid lamella. Modified from Schramm and Wassmuth (1994).

Foaming Agents

Surfactants are commonly used as foaming agents due to their ability to decrease the interfacial tension between two fluids, as well as their high availability and low costs. There are four major surfactant groups classified based on their electric charge: anionic,

cationic, non-ionic, and amphoteric. Selection of the optimal surfactant for CO₂ foam application requires careful consideration of several factors, including foaming ability, chemical stability at reservoir conditions with elevated temperatures and salinities, adsorption to reservoir rock, environmental impact, and costs. During this study, a non-ionic, water-soluble surfactant (Surfonic L24-22, *Indorama Ventures*) was used. At the experimental conditions, the surfactant was stable, had low adsorption in carbonate reservoirs (Jian et al., 2016), and low adsorption in sandstone reservoirs was anticipated. The surfactant has previously shown promising effects on CO₂ mobility reduction at laboratory- and field-scale (Alcorn et al., 2022).

Despite the wide use of surfactants as foaming agents, the long-term stability of surfactant-based foams is limited by surfactant adsorption, the presence of oil, and harsh reservoir conditions with elevated salinities and temperatures (Sheng, 2013). Adding silica nanoparticles may improve the stability of CO₂ foams due to their mechanical and thermal stability (Bennetzen & Mogensen, 2014). Nanoparticles are small colloidal particles composed of a core and chemically modified surface with well-defined properties. Spherical silica nanoparticles (Levasil CC3301, *Nouryon*) were used during this study (**Papers 1 and 3**). The particles are commonly used for EOR applications because of their low fabrication cost, flexible surface modification, and natural occurrence in the reservoir, making them environmentally friendly (Skauge et al., 2010; Talebian et al., 2014).

Foam Generation and Destabilization

Foam generation and destabilization are continuous, dynamic, and contrary processes. In order to generate foam, the rate of bubble generation must exceed the rate of bubble destabilization. In porous media, foam can be generated *in-situ* by two different injection methods: co-injection or cyclic injection in alternating slugs (Farajzadeh et al., 2012). Co-injection refers to the simultaneous injection of CO₂ and a foaming solution at desired injection rate and gas fraction. Co-injection is the most common injection strategy at the laboratory scale because of the ability to achieve a steady state for deriving foam model parameters. At the field scale, co-injection can be challenging to implement because of operational constraints (Hoefner & Evans, 1995). Some

limitations include rapid pressure increases during foam generation, extremely low injectivities, and challenges related to downhole corrosion. Therefore, cyclic injection of CO₂ and a foaming solution in alternating slugs, also known as surfactant-alternating gas (SAG), is the preferred injection strategy in field operations (Chou et al., 1992; Shan & Rossen, 2004).

Foam generation is driven by three distinct mechanisms: snap-off, lamella division, and leave-behind (Ransohoff & Radke, 1988). Foam generation mechanisms determine foam texture (size and number of bubbles), which affects foam strength and stability (Hirasaki & Lawson, 1985; Ransohoff & Radke, 1988).

Snap-off is the primary mechanism responsible for the generation of strong foam (**Figure 1.3a**). As gas flows through a narrow pore throat and enters a liquid-filled pore body, the local capillary pressure drops, resulting in liquid accumulation in the pore throat. At capillary pressures below a critical value, the liquid snaps off a new gas bubble. Snap-off can repeatedly occur at the same location resulting in increased discontinuity of the gas phase by generating separate gas bubbles that significantly reduce gas mobility (Ransohoff & Radke, 1988; Sheng, 2013).

Lamella division, also called secondary foam generation, occurs when an existing gas bubble exceeds the size of the pore body and approaches a branch-point with several pore throats (**Figure 1.3b**). As the bubble moves through the pore throats, it divides into several lamellae. Lamella division leads to strong foam because of the generation of separate bubbles that reduce gas mobility (Kovscek & Radke, 1994; Ransohoff & Radke, 1988).

Leave-behind occurs when gas enters a liquid-filled pore body from two directions and squeezes the liquid between two gas fronts into a lamella oriented in the flow direction (**Figure 1.3c**). Leave-behind occurs during drainage and generates continuous foam spanning across several pores. The foam generated by leave-behind is weaker than foam generated by snap-off and lamella division because gas remains a continuous and mobile phase, and separate bubbles are not created (Chen et al., 2004; Ransohoff & Radke, 1988). Although weak foam is generated by leave-behind, combining the three mechanisms results in strong foam generation.

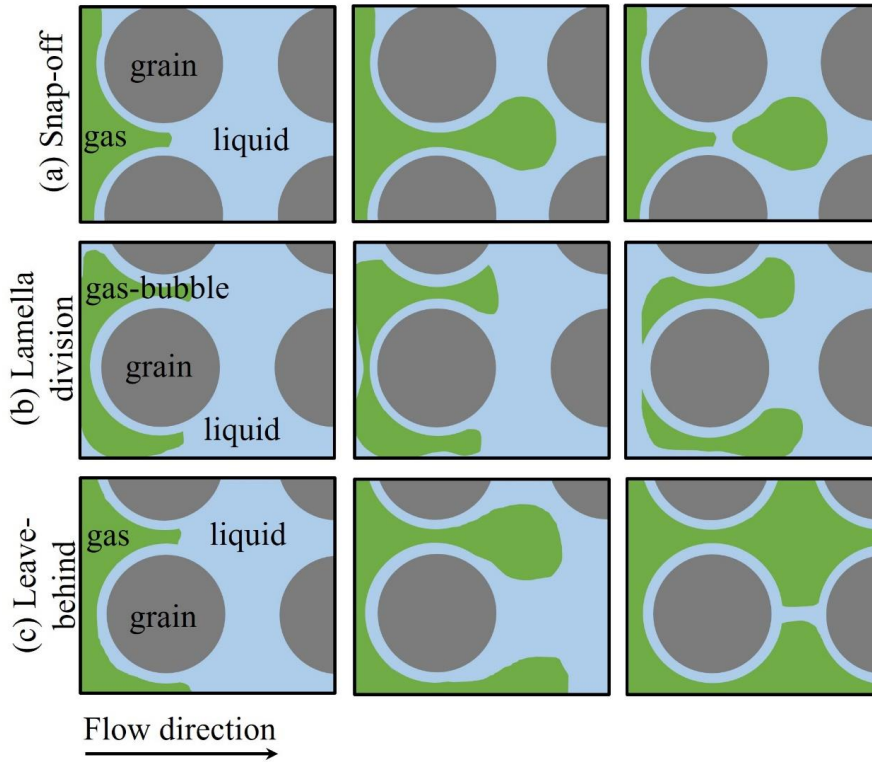


Figure 1.3. Foam generation mechanisms: a) snap-off, b) lamella division, c) leave-behind. The arrow indicates the flow direction of gas (green) into liquid-filled (blue) porous media (gray). Modified from Ransohoff and Radke (1988).

Foams are thermodynamically unstable and their stability relies on the stability of a single lamella. In porous media, lamellae move and rearrange to achieve minimum interfacial free energy resulting in changes in foam texture and foam destabilization (Kornev et al., 1999). The rate of foam destabilization strongly depends on the type, concentration, and retention of surfactant. Lamella instability is primarily driven by three mechanisms: drainage, coalescence, and coarsening (Wang et al., 2016). Liquid drainage occurs due to gravity, where liquid drains from lamella because of gravitational forces or due to capillary suction, where liquid saturation is reduced because the capillary pressure exceeds the maximum disjoining pressure of the lamella, resulting in lamella thinning (Kornev et al., 1999; Sheng, 2013). Bubble coalescence arises when lamella between two bubbles rupture resulting in bubbles merging (Yekeen

et al., 2018). Coarsening, known as Ostwald ripening, refers to bubble growth due to inter-bubble gas diffusion through lamella caused by capillary pressure differences. Coarsening by diffusion is the primary foam destabilization mechanism in porous media because of the more dominant effect of surface forces compared to volumetric forces (Yu & Kanj, 2022). Pore-level Ostwald ripening of CO₂ foams is presented in **Paper 2**.

Foam Strength and Stability

This dissertation aims to investigate the impact of distinct factors on the strength, stability, and efficiency of CO₂ foam for CO₂ EOR and associated CO₂ storage. The strength and stability of CO₂ foam are influenced by several factors, including the presence of oil, reservoir conditions (pressure and temperature), the petrophysical properties of the rock, and the salinity of the formation water. At the pore-scale, foam strength is quantified by foam texture. Fine-textured foam with a high number of small bubbles indicates stronger foam. At the core-scale, foam strength can be determined by its apparent viscosity. Foam apparent viscosity is based on Darcy's law and is a function of rock permeability, injection rate, and pressure gradient across the core:

$$\mu_{app} = \frac{k}{u_{gas} + u_{liquid}} \nabla p \quad (1)$$

where k is the absolute permeability of the core, u_{gas} and u_{liquid} is the superficial velocity of gas and liquid, respectively, and ∇p is the pressure gradient across the core (Jones et al., 2016). An increase in apparent viscosity indicates foam generation, and a higher apparent viscosity indicates stronger foam.

The Effect of Permeability

The absolute permeability of the porous media is a crucial property that affects foam stability due to its correlation with pressure gradient. To generate and sustain fine-textured foam, a minimum pressure gradient needs to be exceeded (Falls et al., 1988; Kovscek & Radke, 1994). As permeability increases, the pressure gradient decreases, generating stronger and more stable foams in high-permeable areas of a reservoir compared to lower-permeability areas (Gauglitz et al., 2002). This feature results in

foam blockage in high-permeable zones, flow diversion, and improved volumetric sweep efficiency in low-permeable zones (Farajzadeh et al., 2012). The effect of rock permeability on foam generation and strength is presented in **Paper 5**, where foam behavior in sandstone and carbonate core plugs was investigated.

The Effect of Oil

The presence of oil has an adverse effect on lamella generation and stability. Oil concentration and composition determine to which extent oil affects foam. High oil concentrations above a critical foaming oil saturation hinder foam generation, and lighter crude oils are more detrimental to foam than heavier oils because more viscous oils emulsify at lower rate (Friedmann & Jensen, 1986; Schramm & Novosad, 1992). Foam destabilization in the presence of oil can be caused by several mechanisms, including (1) partition of foaming agent in the oil phase resulting in reduced ability to generate foam, (2) spontaneous oil spreading on lamella causing rapid bubble rupture, (3) spontaneous oil emulsification resulting in lamella drainage and rupture and (4) occupancy of pore space where snap-off may occur hindering generation and regeneration of foam (Ross & McBain, 1944; Sheng, 2013). **Papers 1, 4, and 5** shed light on the influence of oil on CO₂ foam.

The Effect of Reservoir Conditions

Foam strength and stability are influenced by elevated temperatures and pressures in reservoirs. Elevated temperatures increase the aqueous solubility of surfactants, resulting in reduced surfactant concentration in the gas-liquid interface. Additionally, high temperatures accelerate liquid film drainage, destabilizing foam (Maini & Ma, 1986; Sheng, 2013). Conversely, increased pressure stabilizes the foam by reducing gas bubble size, increasing liquid film size, and slowing down liquid drainage. Foam stability increases with increasing pressure until a specific maximum value, known as the limiting capillary pressure, is reached. Exceeding this pressure subjects the gas bubbles to high stress, resulting in bubble rupture (Sheng, 2013).

1.5 Real-Time Foam Visualization

Real-time visualization of CO₂ foam generation and flow in porous media can provide insight into complex mechanisms that improve understanding of foam behavior. This work investigated foam generation, coalescence, and displacement processes through real-time pore- and core-scale visualization.

Lab-on-a-Chip Technology

Lab-on-a-chip (LoC) technology was initially developed for biomedical and chemical research but has adapted as a valuable tool to study fluid flow in porous media (Kim et al., 2013). LoC technology utilizes high-pressure microfluidic devices with realistic pore networks to provide insight into fundamental physical processes and complex mechanisms during fluid flow at reservoir conditions (Datta et al., 2023). LoC provides high-resolution *in-situ* images which enable qualitative and quantitative investigation of foam generation, coalescence, and flow dynamics at pore-scale (Benali et al., 2022). In addition, microfluidics provide a useful tool for studying pore-scale interactions between fluids and rock materials in CCUS research. Direct visualization contributes to a deeper understanding of CO₂ trapping mechanisms and the optimization of carbon sequestration processes (Datta et al., 2023; Gizzatov et al., 2021). Utilization of LoC in CCUS research has several advantages. Microfluidic experiments are conducted at a much smaller scale than traditional core-flooding experiments, reducing the volume of fluids and chemicals and the operational time. This reduces costs and allows faster data acquisition (Jian et al., 2021). Microfluidic chips can be tailored with desired pore structures, dimensions, and properties, which allows one to study the influence of various parameters on CO₂ foam behavior (Datta et al., 2023; Gizzatov et al., 2021).

This study used a 2D micromodel with a synthetic porous media similar to sandstone to directly visualize CO₂ foam in porous media (**Papers 1-3**). High-resolution images of the entire pore network were continuously captured by a microscope and analyzed using Python libraries OpenCV and skimage. Images obtained using LoC technology provided valuable information and understanding of core-scale events.

PET-CT *In-situ* Imaging

Advanced *in-situ* imaging by Positron Emission Tomography (PET) combined with Computed Tomography (CT) can be used to quantify and visualize fluid flow at the core-scale. The technology combines information about the porous structure obtained through CT imaging and fluid flow dynamics acquired from PET.

PET was primarily used as a clinical diagnostic tool. However, it has recently emerged as a highly useful tool for non-medical purposes, such as fluid flow visualization in porous structures (Zahasky et al., 2019). PET imaging is based on positron emission due to radioactive tracer decay, which annihilates a surrounding electron. Consequently, two photons with an energy of 511 keV are emitted in opposite directions and are detected by the PET scanner, which counts the number of events with high spatial and temporal accuracy (Bailey et al., 2005; Brattekås et al., 2021). Based on that, a 3D image of tracer distribution in the porous media is created without the influence of rock properties, mineralogy, or initial saturations (Brattekås & Haugen, 2020). A range of radioactive tracers can be used for PET fluid flow visualization. The most commonly used radioisotope is the water-soluble and widely available ^{18}F -fluorodeoxyglucose (^{18}F -FDG) with a half-life of $T_{1/2} = 109.8$ min (Zahasky et al., 2019). To track CO_2 , the radionuclide ^{11}C with a half-life of $T_{1/2} = 20.3$ min can be attached to CO_2 , making $^{11}\text{C}\text{CO}_2$ tracer (Fernø et al., 2015; Pini et al., 2016). Tracing CO_2 allows explicit visualization of CO_2 flow in porous media (Brattekås et al., 2021). In this study, ^{18}F -FDG was used to label the aqueous phase and capture CO_2 flow dynamics implicitly.

CT imaging was originally invented for medical purposes but is today widely used in the petroleum industry to characterize porous structures, measure their properties, observe the fluid flow and, measure fluid saturations (Akin & Kovscek, 2003). A CT scan utilizes X-rays that penetrate an object to visualize porous media and fluid flow. The fluids and solid components adsorb X-rays as they pass through a porous media, and an array of detectors measure X-ray attenuation. During the scan, multiple X-ray projections are captured from different angles, which enable the reconstruction of a detailed 3D image of the porous media and the containing fluids (Hirono et al., 2003).

1.6 CO₂ Foam Field Pilot

Pilot Overview

A CO₂ foam field pilot was recently conducted in East Seminole Field, a mature carbonate reservoir in the Permian Basin, USA, which suffered from poor CO₂ sweep efficiency due to reservoir heterogeneity and high CO₂ mobility. The primary objective of the pilot was to achieve *in-depth* CO₂ mobility control to increase oil recovery and CO₂ storage potential (Alcorn et al., 2019). The foam system was designed in the laboratory through surfactant screening, optimizing surfactant concentration, determining the optimal foam quality and verifying foam stability in the presence of residual oil (Sharma et al., 2017).

The pilot area was an inverted 40 acre five-spot pattern with a central injection well and four surrounding producers (Figure 1.4). Multi-cycle surfactant-alternating gas (SAG) injection strategy consisting of eleven cycles was performed during the pilot. Each cycle included 10 days of 0.50wt% non-ionic surfactant (Surfonic L24-22, *Indorama Ventures*) solution injection followed by 20 days of CO₂ injection (Alcorn et al., 2020b).

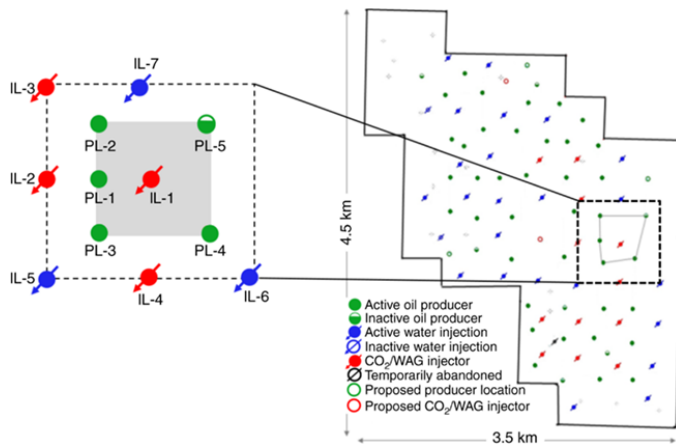


Figure 1.4. The inverted 40 acre five-spot pattern (gray area) with a central injection well (IL-1) and four surrounding producers (PL-1 – PL-5) in East Seminole Field. From Alcorn et al. (2019).

A baseline data collection and pilot monitoring plan were established to obtain a baseline from the pre-pilot injection periods and monitor field performance during SAG injections (Alcorn et al., 2022). Foam generation was confirmed during the pilot based upon delayed CO₂ breakthrough time compared to the baseline CO₂ breakthrough time, higher bottom hole pressure (BHP) values compared to the pre-pilot period, and an increase in oil production compared to pure CO₂ injection (Alcorn et al., 2020b). The collected data was used to improve reservoir modeling and study foam flow at the field-scale.

Field-Scale Modeling

Numerical modeling is a valuable tool to describe and understand fluid flow at the field-scale. Field-scale modeling combined with laboratory work and field experience can address challenges related to large-scale implementation of CO₂ foam EOR and CO₂ storage. There are two primary foam modeling approaches: a population-balance (PB) model, which explicitly represents the dynamics of lamella generation, propagation, and coalescence to quantify gas mobility reduction by foam, and a local-equilibrium (LE) model, which implicitly represents the effect of foam texture on gas mobility by introducing a mobility reduction factor (FM) (Farajzadeh et al., 2012; Sharma et al., 2017). Due to complex foam dynamics and challenges related to extracting foam model parameters for the PB model, the LE models are preferred for field-scale studies.

The LE model assumes foam is present anywhere gas, water, and sufficient surfactant concentration are present. The effect of foam on gas mobility reduction is accounted for in LE models by multiplying the gas relative permeability (k_{rg}^{nf}) in the absence of foam with a mobility reduction factor (FM), whereas the water relative permeability remains unchanged (Farajzadeh et al., 2012).

$$k_{rg}^f = k_{rg}^{nf} \times FM \quad (2)$$

FM includes the effect of various factors and defines by the expression:

$$FM = \frac{1}{1 + f_{mmob} \times F_{water} \times F_{shear} \times F_{surf} \times F_{oil}} \quad (3)$$

where $fmmob$ refers to the maximum gas mobility reduction that can be achieved and F_{water} , F_{shear} , F_{surf} and F_{oil} capture the water saturation, shear rate, surfactant concentration, and oil saturation dependence, respectively. The factors are functions of foam model parameters (e.g. $fmdry$, $epdry$, $fmcap$, $epcap$) determined from core-scale experimental data (Ma et al., 2013).

Different commercial simulators have adopted the LE model (Talebian et al., 2014). This work used a conventional finite-difference compositional reservoir simulator (ECLIPSE 300) to study foam generation and propagation (**Paper 6**). The compositional model was based on the Peng-Robinson (PR) equation of state (EoS) model with six components tuned to pressure-volume-temperature (PVT) data (Sharma et al., 2017).

2. Results and Discussion

CO₂ foam mobility control for CO₂ EOR and CO₂ storage is an important technology in the ongoing energy transition. A comprehensive understanding of foam dynamics, strength, and stability at reservoir conditions is essential to advance this technology. This dissertation provides insights into the fundamental concepts, including the influence of factors such as oil saturation, rock type, and foaming solution concentration on CO₂ foam behavior. Furthermore, the effectiveness of CO₂ foam in enhancing oil recovery and increasing CO₂ storage capacity was evaluated.

2.1 CO₂ Foam Generation and Destabilization

Foam Generation

Foam generation was studied through a multi-scale approach spanning from pore- to core-scale (**Papers 1-3**). Unsteady-state CO₂ injections into micromodels with a realistic porous network and core plugs pre-saturated with foaming solutions were performed to capture foam generation. Lab-on-a-chip technology which allowed direct visualization of fluid dynamics and foam morphology during CO₂ injections was used at pore-scale. At the core-scale, foam generation was determined based on apparent viscosity calculations (Eq. (1)).

Figure 2.1 shows the bubble number normalized to baseline as a function of pore volume (PV) of CO₂ injected into a micromodel saturated with three different foaming solutions: 0.15wt% silica nanoparticles (NP) (black), 0.50wt% nonionic surfactant (SF) + 0.15wt% NP (green) and 0.50wt% SF (red). The rapid increase in bubble number as CO₂ was injected into surfactant-saturated micromodel indicated foam generation for all experiments with surfactant (**Figure 2.1**, green and red curves). The number of bubbles increased by 10 to 11 times, compared to the baseline, indicating a finer textured foam. After approximately 9 PVs of CO₂ injection, the foam coalescence rate exceeded the foam generation rate indicated by the decrease in the number of bubbles. In the absence of surfactant, coarse foam with low bubble number was generated, indicating that surfactant was the main foam generator (**Figure 2.1**, black curve).

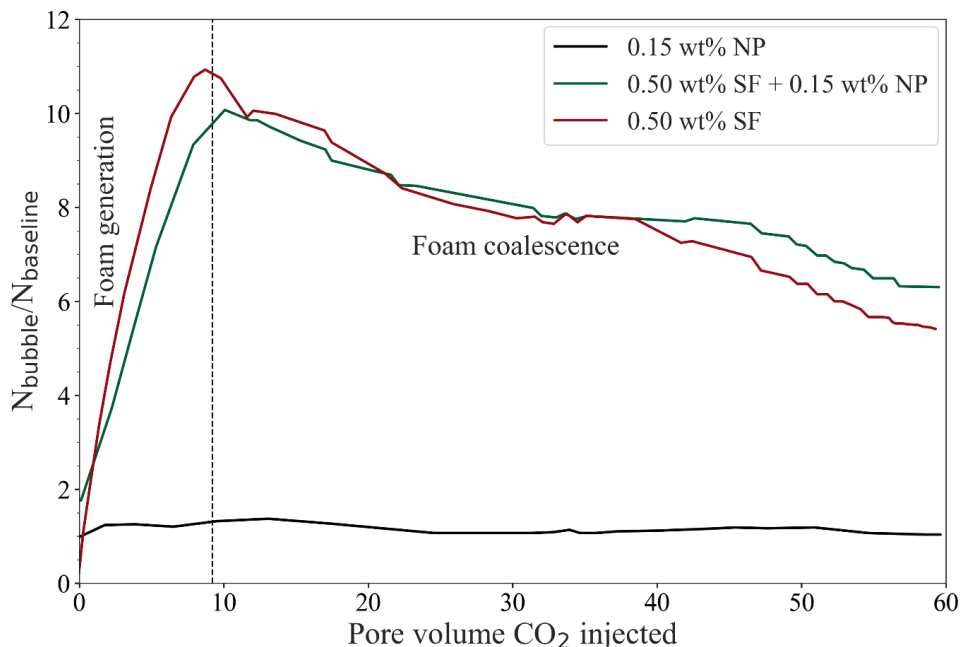


Figure 2.1. Bubble number (N_{bubble}) normalized to baseline (N_{baseline}) as a function of pore volume CO_2 injected for three different foaming solutions: 0.15wt% nanoparticles (NP) (black), 0.50wt% surfactant (SF) + 0.15wt% nanoparticles (NP) (green), and 0.50wt% surfactant (SF) (red). An increase in bubble number indicated foam generation and was observed using surfactant-based solutions. Modified from Paper 1.

Bubble generation in a focused field of view, representing the remainder of the micromodel, was investigated to gain a deeper understanding of foam generation processes. Studying the location, size, and number of bubbles can reveal the main generation mechanisms. Dynamic observations showed separate bubbles located near the ends of the pore throats, indicating snap-off as the primary foam generation mechanism (**Figure 2.2**, orange circles). Repeated snap-off was observed in the same location as multiple bubbles occupied individual pore bodies, a phenomenon also observed by Ransohoff and Radke (1988). Furthermore, lamellae spanned across several pore throats providing evidence of leave-behind as the secondary foam generation mechanism (**Figure 2.2**, green). Snap-off and leave-behind were the generation mechanisms likely due to drainage-like CO_2 injection, which increased capillary pressure as the gas entered the pores (Ransohoff & Radke, 1988).

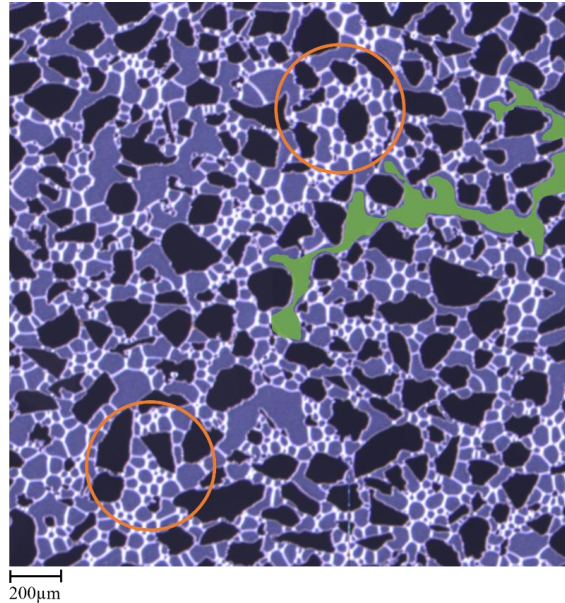


Figure 2.2. Pore-scale image of a focused field of view during CO₂ injection into surfactant-saturated micromodel. Repeated snap-off was the primary foam generation mechanism (orange circles) and leave-behind was the secondary generation mechanism (green). Black and purple areas represent grains and CO₂, respectively and the thin white films are lamellae. Modified from Paper 1.

Unsteady-state CO₂ injections into sandstone core plugs saturated with either a foaming solution or brine were performed to study foam generation at the core-scale. **Figure 2.3** shows the apparent viscosity as a function of PV of CO₂ injected using three different aqueous solutions: 0.35wt% surfactant (SF) + 0.15wt% nanoparticles (NP) (green), 0.50wt% surfactant (SF) (red) and brine (black). The rapid and linear increase in the apparent viscosity during CO₂ injection into a foaming solution-saturated core indicated foam generation. The increase in apparent viscosity was caused by increased flow resistance due to the generation of lamellae that impeded some of the pathways for CO₂ flow. Foam generation started after 0.2 PV of CO₂ injected and continued until reaching a maximum apparent viscosity of 59 ± 2 cP after approximately 0.5 PV of CO₂ injected. Beyond that point, foaming solution concentration in the core decreased, gas fraction increased, and foam collapsed, as shown by the decrease in apparent viscosity. Surfactant- (**Figure 2.3**, red curve) and hybrid-based (**Figure 2.3**, green

curve) foam showed similar foam dynamics which indicated that foam was not sensitive to changes in surfactant concentration and the presence of silica nanoparticles. The effect of foaming solution and nanoparticles on foam behavior are described in Chapters 2.2 and 2.3. In addition, the apparent viscosity results showed the importance of foaming solution on foam generation through comparison with the baseline, where the core was saturated with brine without a foaming agent (**Figure 2.3**, black dashed curve). During baseline, lamellae were not generated, and CO₂ was flowing through the pores as a continuous phase giving a low apparent viscosity (1.6 ± 0.1 cP).

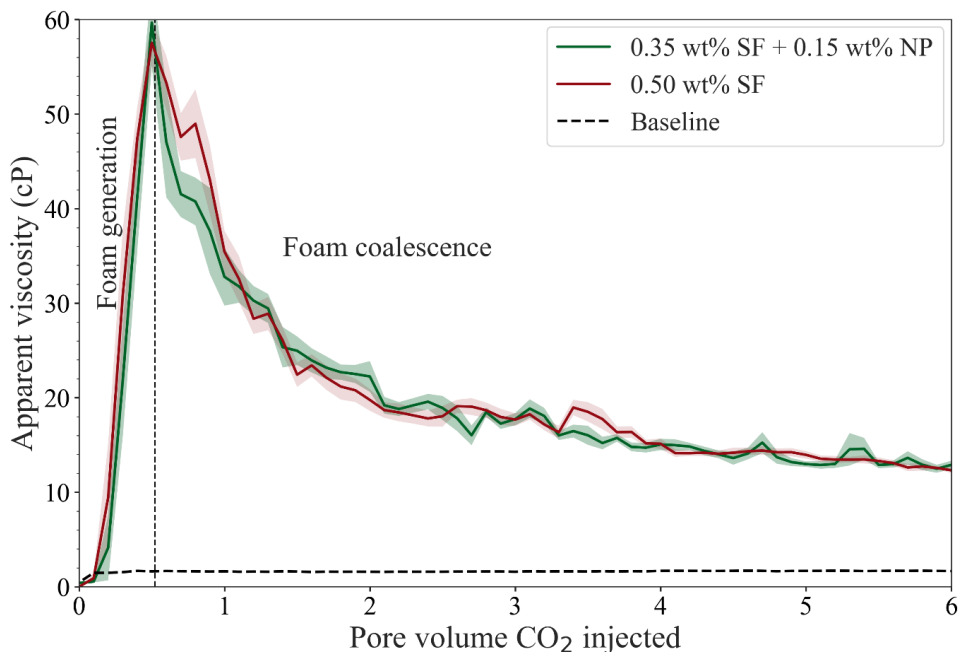


Figure 2.3. Apparent viscosity as a function of pore volume CO₂ injected for unsteady-state CO₂ injection into core plug saturated with 0.35wt% surfactant (SF) + 0.15wt% nanoparticles (NP) (green), 0.50wt% surfactant (SF) (red), and baseline without foaming agent (black). Foam was generated in the presence of foaming agent and similar behavior was observed for both solutions. The shaded areas represent the uncertainties. Modified from Paper 1.

Multi-scale study of foam generation revealed similarities across the pore- and core-scales during unsteady-state CO₂ injections into foaming solution saturated porous media. Foam generation at the pore-scale was characterized by a rapid increase in

bubble number corresponding to finer textured foam, which implies lower gas mobility (Kovscek & Radke, 1994). At the core-scale, foam generation during drainage-like CO₂ injection was characterized by a rapidly increasing apparent viscosity due to generation of fine-textured bubbles that impeded CO₂ flow and led to large flow resistance.

The generation and flow behavior of CO₂ foam can differ between 2D micromodels and 3D core plugs due to contrasting characteristics and limitations of each system. Micromodels are simplified representations of porous media that lack the complexity of real rock formations. Micromodels allow visualization of CO₂ foam flow and are ideal to study fundamental processes at the microscopic scale. In contrast, the core plugs capture the impact of rock heterogeneity and flow paths on foam and provide a more realistic representation of fluid flow. Although the foam behavior can differ between the two length scales, the pore-scale observations provided insights into foam generation mechanisms and *in-situ* foam behavior to help explain core-scale observations.

Foam Destabilization

Foam destabilization was investigated at the pore- and core-scale (**Papers 1 and 2**) and was identified by quantitative analysis of the changes in foam texture at the pore-scale and by the changes in apparent viscosity at the core-scale. Pore-level destabilization of CO₂ foam was investigated for dynamic (**Paper 1**) and static (**Paper 2**) CO₂ foam.

Direct visualization of dynamic CO₂ foam in a micromodel showed a steady decrease in the number of bubbles (**Figure 2.1**) and a change in bubble size with increasing gas saturation (**Figure 2.4**). **Figure 2.4a** shows a pore-scale image (2190 x 2190 μm) of a focused field of view after 1.3 PVs of CO₂ injected with corresponding bubble size distribution. Bubbles smaller than 10³ μm² were characterized as small (**Figure 2.4**, green bars), whereas bubbles greater than 10³ μm² were large small (**Figure 2.4**, blue bars). At 1.3 PVs of CO₂ injected, foam generation started and the majority of bubbles (approximately 70%) were large with bubble size greater than 10³ μm² (**Figure 2.4a**). As CO₂ injection continued, finer textured foam was generated indicated by increased bubble number by up to 170%, and decreasing bubble size from 10⁴ – 10⁶ μm² to ≤

$10^3 \mu\text{m}^2$. After approximately 10 PVs of CO_2 injected (**Figure 2.4b**), the maximum number of bubbles was reached and approximately 60% of the bubbles were characterized as small bubbles.

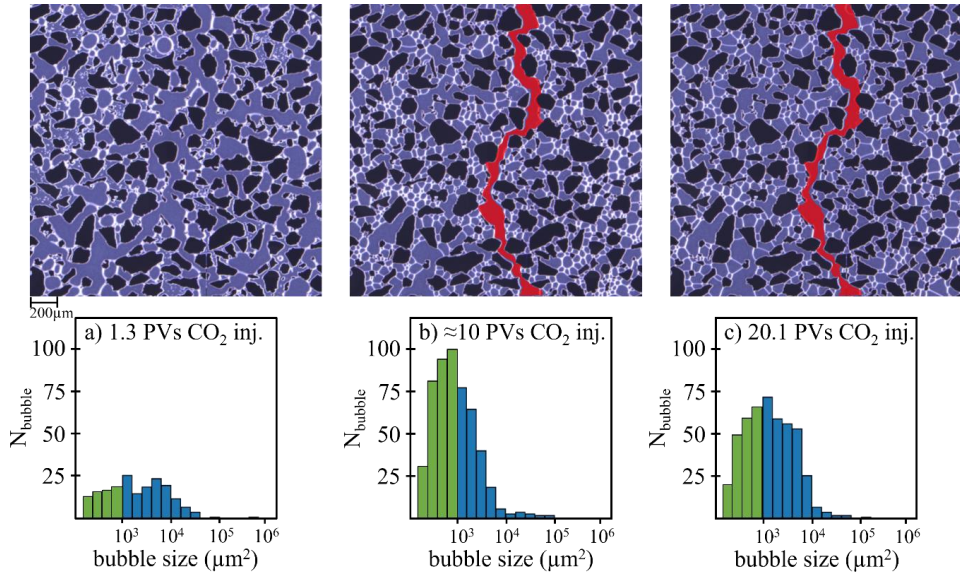


Figure 2.4. Pore-scale images of a focused field of view ($2190\mu\text{m} \times 2190\mu\text{m}$) during CO_2 injection into a micromodel saturated with hybrid nanoparticle-surfactant solution for three timesteps (a-c) and corresponding bubbles size distribution. Green bars represent small bubbles with size $\leq 10^3 \mu\text{m}^2$, and blue bars represent larger bubbles with size $> 10^3 \mu\text{m}^2$. Black and purple areas represent grains and CO_2 , respectively and the thin white films are lamellae. Bubble coarsening and generation of open flow channels (red) was observed. Modified from Paper 1.

Image analysis revealed two types of bubbles: discontinuous bubbles trapped in individual pores, and continuous bubbles or pathways spanning across several pores (red) that CO_2 freely flowed through. After 20.1 PVs of CO_2 injected (**Figure 2.4c**), the number of bubbles decreased by 10%, and the bubble size coarsened indicated by the change in bubble size. At this stage, approximately 40% of the bubbles were small and 60% were large. The changes in foam texture indicated the destabilization of foam with lamella coarsening as the primary mechanism. The open flow channels remained unchanged, and most of the CO_2 flowed through them, leaving a high number of

bubbles trapped in the remainder of the pore network. The discontinuous bubbles trapped in the pores reduced CO₂ relative permeability and continued to reduce CO₂ mobility.

Investigation of static CO₂ foam confirmed that bubble coarsening, known as Ostwald ripening, was the dominant destabilization mechanism. Calculations of the average bubble area through time determined the destabilization of static CO₂ foam, where increased bubble area indicated foam coarsening. The study revealed three types of bubble coarsening: (1) bubble coarsening unrestricted by the grains, (2) bubble coarsening restricted by the grains, and (3) equilibration of plateau borders.

Type 1 coarsening was characterized by the growth of large bubbles at the expense of smaller bubbles due to capillary pressure differences which resembled a bulk foam system because the coarsening was unrestricted by the porous media (**Figure 2.5a**). Type 1 coarsening was a slow process, as the presence of foaming solution stabilized the lamellae and reduced the coarsening rate. After nearly 60 hours, the equilibrium was still not reached and coarsening continued. Type 2 coarsening was characterized by large bubbles growing at the expense of small bubbles at low aqueous phase saturation, restricted by the grains. This coarsening was driven by lamella movement and rearrangement to achieve minimum energy configuration at the pore throats (**Figure 2.5b**) (Kornev et al., 1999). Type 2 coarsening resulted in the disappearance of small bubbles with high curvature due to CO₂ diffusion into larger bubbles (Yu & Kanj, 2022). **Figure 2.5b** shows the direction of CO₂ diffusion in a chosen focused field of view. The average area of the largest bubble increased by approximately 55% after 49.7 hours, and the coarsening continued. Type 3 coarsening referred to the equilibration of plateau borders and occurred when lamellae were located in the middle of a pore. The lamellae moved until the angles for all the interfaces between the bubbles in the plateau border equal 120 degrees (**Figure 2.5c**). The foam was unstable and triggered CO₂ diffusion until equilibrium was achieved.

A combination of all three types of coarsening led to the destabilization of foam. Type 2 coarsening was the dominant coarsening mechanism in the studied case because a majority of foam bubbles were restricted by the pore walls, and most lamellae were

located in the pore throats. Additionally, anti-coarsening was observed, a phenomenon where small bubbles grow at the expense of larger bubbles. Anti-coarsening occurred as lamella moved towards pore throats due to capillary suction (Xu et al., 2017; Yu & Kanj, 2022).

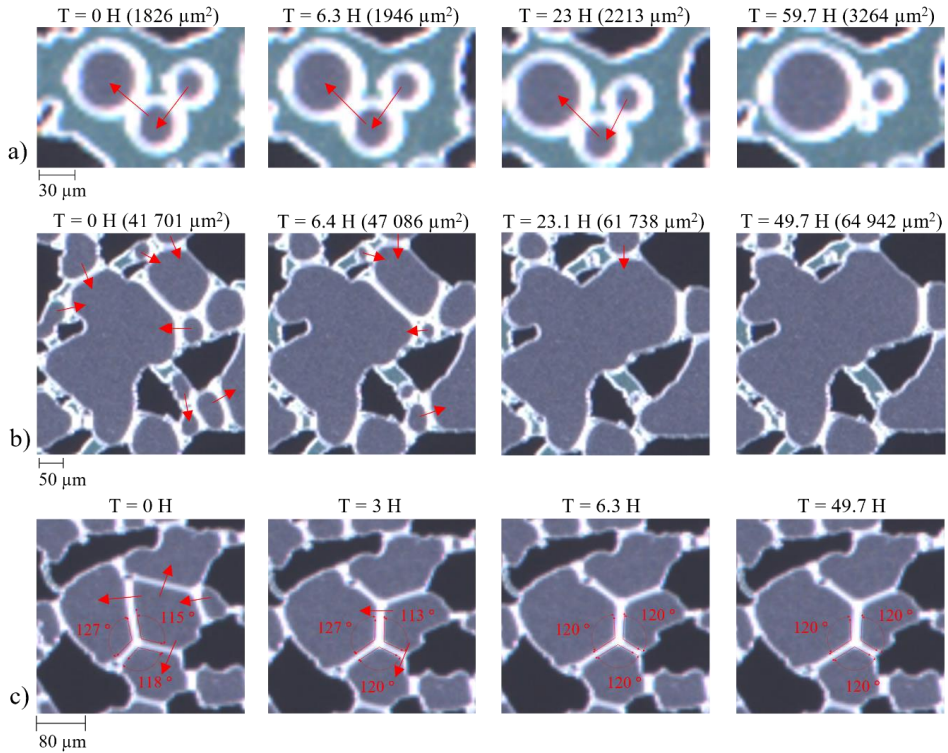


Figure 2.5 Three types of static foam coarsening: (a) coarsening unrestricted by the grains, (b) coarsening restricted by the grains and (3) equilibration of plateau borders. Black, purple, and blue areas represent grains, CO_2 and the aqueous phase, respectively. The red arrows indicate the direction of CO_2 diffusion. The average area of the largest bubble in (a) and (b) is shown above the images. Modified from Paper 2.

Foam destabilization was investigated at the core-scale based on the apparent viscosity during unsteady-state CO_2 injections into core plugs saturated with foaming solution, as described in the previous section. A decrease in apparent viscosity (**Figure 2.3**) indicated foam dry-out, a phenomenon where foam collapses because of decreasing foaming solution saturation and increasing gas fraction (Farajzadeh et al., 2015). In

addition, the development of open and continuous CO₂ flow paths not impeded by lamella, as observed at the pore-scale, led to decreased apparent viscosity. Despite rapid foam coalescence, the apparent viscosity remained higher than the viscosity of pure supercritical CO₂ after 6 PVs injected because the trapped and discontinuous CO₂ bubbles in the pores continued to reduce CO₂ mobility. Similar behavior was observed at the pore-scale, where the number of bubbles remained five to six times higher than baseline even after 60 PVs of CO₂ injected (**Figure 2.1**).

CO₂ Foam Generation at Field-Scale

Foam generation at the field-scale can be confirmed based on increased bottom hole pressure (BHP), delayed CO₂ breakthrough time, and improved sweep efficiency, indicated by increased oil and water production, compared to a baseline without foam. Foam generation and propagation during a recently completed CO₂ foam field pilot were investigated using a single injection well radial reservoir simulation model (**Paper 6**). The model was based on a sector scale model that was history matched to the historical water and CO₂ injection periods in the same field (Sharma et al., 2017). The field pilot was conducted in East Seminole Field, a mature and heterogeneous carbonate reservoir in Permian Basin, USA. Multi-cycle surfactant-alternating gas (SAG) injection strategy consisting of eleven cycles was performed during the pilot. Each cycle included 10 days of 0.50wt% surfactant solution injection followed by 20 days of CO₂ injection.

To assess foam generation, a baseline WAG case and a SAG case were simulated at injection rates consistent with the observed rates from the field pilot. The baseline WAG case was performed to establish a baseline and determine CO₂ relative permeability reduction during a WAG injection. For the SAG case simulation, CO₂ foam was modeled using an implicit texture local-equilibrium (LE) model with foam model parameters derived from experimental foam quality and rate scan data conducted on a reservoir core at reservoir conditions (Rognmo et al., 2019). The simulated cases were compared to the observed BHP response during the field pilot to determine CO₂ mobility reduction. **Figure 2.6** shows the simulated injection BHP for baseline WAG (blue) and SAG (red) cases and the observed BHP response from the field (black).

Comparison between the baseline WAG and SAG cases showed foam generation in the presence of surfactant indicated by increased BHP. Foam generation was also observed during the field pilot, indicated by higher observed BHP response than in the simulated baseline WAG case. Injection BHP for the SAG case was considerably higher than the observed BHP, especially after the fourth cycle, which indicated weaker foam during the pilot compared to laboratory and simulation studies. Furthermore, the simulated BHP did not match the observed pressure fall-off after the seventh cycle, as the single injector radial model did not account for the influence of nearby production wells on injection BHP.

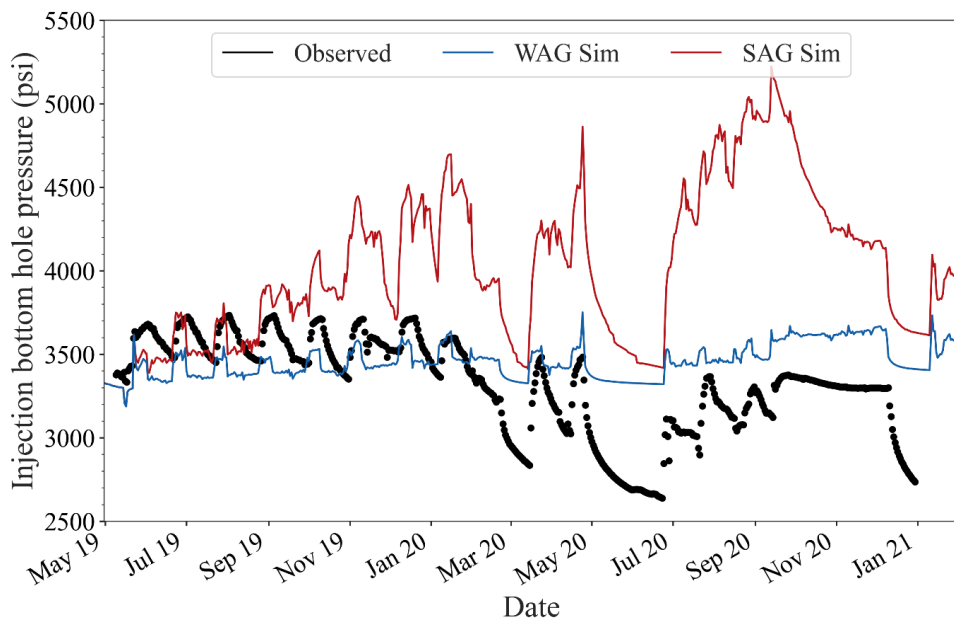


Figure 2.6. Simulated injection bottom hole pressure (BHP) for water-alternating gas (WAG, blue) and surfactant-alternating gas (SAG, red) cases and the observed BHP response during SAG field pilot (black). Modified from Paper 6.

A foam model sensitivity study investigated the impact of different experimentally derived foam model parameters on foam generation. Three SAG cases with different sets of foam model parameters were performed and showed a significant effect of foam mobility reduction factor ($fmmob$) on foam strength. $fmmob$ refers to the maximum gas mobility reduction that can be achieved and is obtained from laboratory

measurements (foam quality and rate scans, described in Chapter 2.2). As $fmmob$ increased, the foam strength increased. The SAG case foam model parameter $fmmob$ was adjusted to match the observed BHP data. Reducing the $fmmob$ value from 192 to 1.9 brought the simulated BHP into closer agreement with the observed BHP (Figure 2.7). The adjusted SAG case was used to gain insight into field-scale foam generation and propagation during the field pilot.

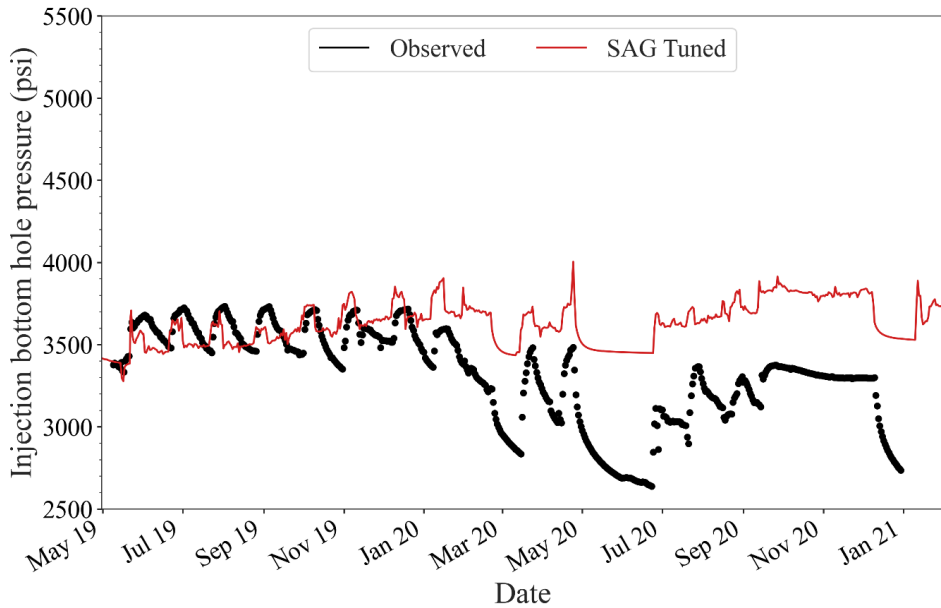


Figure 2.7. Simulated injection bottom hole pressure (BHP) for surfactant-alternating gas (SAG) case (red) adjusted to match the observed BHP data (black) from the field pilot. Modified from Paper 6.

The numerical simulations showed the generation of significantly weaker foam at the field-scale compared to laboratory observations, as $fmmob$ was reduced by two orders of magnitude. Foam generation and propagation are scale dependent as different forces dominate fluid flow at different scales. Gravitational segregation and reservoir heterogeneity considerably impact fluid flow at field-scale, whereas diffusion, dispersion, capillarity, and viscous forces dominate flow at the pore- and core-scale (Alcorn et al., 2020a).

2.2 The Effect of Key Reservoir Properties on Foam

Foam strength and stability are two key factors that highly influence the effectiveness of CO₂ foam for CO₂ EOR and CO₂ storage applications. These parameters, in turn, are influenced by several factors, such as injection rate, the concentration of foaming solution, the presence of oil, rock type, and conditions. The following chapter extends on the results presented in Chapter 2.1 and assesses the foam strength and stability at different reservoir conditions.

The Effect of Gas Fraction and Injection Rate

Foam strength and stability depend on the gas fraction (foam quality) and injection rate (**Papers 4 and 5**). Steady-state co-injections of CO₂ and foaming solution were performed as gravity-assisted injections to determine the optimal gas fraction (f_g) to generate strong foam, to study the effect of injection rate on foam rheology and to provide input data for local-equilibrium (LE) foam modeling. **Figure 2.8a** shows apparent viscosity as a function of gas fraction during co-injections of CO₂ and 1 wt% non-ionic surfactant foaming solution into sandstone (solid curves), limestone (dashed curves), and dolomite (dotted curves) core plugs. The injections were performed at a constant injection rate of 2 ft/day with a monotonically increasing gas fraction from 0.3 to 1.0. Foam quality scans (**Figure 2.8a**) showed a transition from low-quality (wet) to high-quality (dry) foam regimes as the gas fraction increased, also observed by Chang and Grigg (1999). In the low-quality regime, the foam behavior was dominated by bubble trapping and mobilization and the foam apparent viscosity increased with increasing gas fraction until reaching a maximum apparent viscosity (Alvarez et al., 2001). Beyond this point, a limiting capillary pressure was reached and foam entered the high-quality regime. In high-quality regime foam behavior was dominated by coalescence and the apparent viscosity decreased with increasing gas fraction (Alvarez et al., 2001; Kahrobaei et al., 2017; Khatib et al., 1988). In sandstone, foam was in the low-quality regime at f_g ranging from 0.3 to 0.5 and transitioned to high-quality regime at f_g 0.5 to 0.6. In limestone and dolomite, the transition from low- to high-quality regime occurred at f_g 0.6 to 0.7 and 0.75, respectively. The transition gas fraction depends on the limiting capillary pressure above which the foam becomes unstable and

varies with the surfactant type and concentration, gas flow rate, and permeability of the porous media (Alvarez et al., 2001). Therefore, determining the optimal gas fraction for specific field projects is necessary for successful CO₂ foam mobility control.

Despite foam destabilization at high gas fractions, the apparent viscosity at a gas fraction equal to one remained two orders of magnitude higher than that of supercritical CO₂, which demonstrated continued CO₂ mobility reduction by foam. In total, 20 PVs of CO₂ were injected, showing a long-term CO₂ mobility control at the given reservoir conditions.

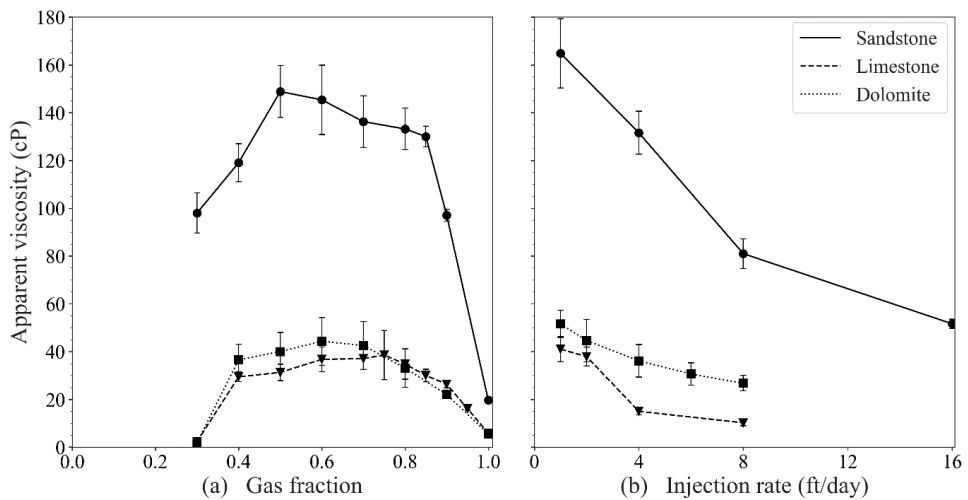


Figure 2.8. (a) Apparent viscosity versus gas fraction and (b) apparent viscosity versus injection rate during steady-state co-injections of CO₂ and surfactant-based foaming solution into sandstone (solid), limestone (dashed), and dolomite (dotted). Modified from Paper 5.

Co-injections of CO₂ and foaming solution at a constant gas fraction (0.6 in sandstone and 0.7 in carbonates) determined from foam quality scan (**Figure 2.8a**) with decreasing injection rates (16 ft/day to 2 ft/day in sandstone, 8 ft/day to 1 ft/day in limestone) were performed to study the effect of injection rate on CO₂ foam strength. **Figure 2.8b** shows apparent viscosity as a function of the injection rate for the three core plugs. Shear-thinning foam behavior, where apparent viscosity decreased with increasing injection rate, was observed. Foams are non-Newtonian fluids with stress-dependent viscosity (Kahrobaei et al., 2017). At high injection rates, the shear rate increases, leading to large pressure drops and lamella rupture, reducing foam stability

and decreasing apparent viscosity (Khan et al., 1988). Shear-thinning foam rheology is favorable for field applications because it mitigates injectivity loss near the wellbore where the injection rates typically are high and contribute to *in-depth* mobility control because the injection rate decreases as the foam propagates into the reservoir (Alvarez et al., 2001).

The Effect of Rock Type

The effect of rock type on CO₂ foam strength and stability was evaluated through steady- and unsteady-state CO₂ injections. Stronger foam was generated in sandstone core plugs compared to carbonate cores based on apparent viscosity calculations during steady-state CO₂ injections (**Figure 2.8**). Due to absolute permeability differences, the apparent viscosity in sandstone was approximately three times higher than in limestone and dolomite. The sandstone cores had an average absolute permeability of 1400 mD, whereas limestone and dolomite had permeabilities of 38 mD and 22 mD, respectively. As permeability increases, the minimum pressure gradient required to generate foam decreases, and stronger foams tend to generate (Falls et al., 1989; Gauglitz et al., 2002). In addition, stronger and finer textured foams tend to generate in porous media with larger pores and pore throats and a lower aspect ratio (Adebayo, 2021). Measurements of T₂ relaxation using *in-situ* nuclear magnetic resonance (NMR) showed larger pore body and pore throat size in Bentheimer sandstone compared to Edwards limestone (Johannesen et al., 2007; Peksa et al., 2015), resulting in a lower aspect ratio in sandstone than limestone.

Foam behavior in the three rocks was characterized by two foam quality regimes and shear-thinning rheology discussed above (**Figure 2.8**). In carbonates, foam generation did not occur at a low gas fraction of 0.3, likely due to not exceeding the minimum pressure gradient to generate foam. The optimal gas fraction varied for the three rocks. It was higher in carbonates ($fg = 0.60 - 0.75$) than in sandstone ($fg = 0.5$) due to a lower limiting capillary pressure in sandstone, which led to foam destabilization at lower gas fractions. Previous studies reported both increasing and decreasing limiting capillary pressure with increasing permeability (Alvarez et al., 2001; Farajzadeh et al., 2015; Khatib et al., 1988). Although foam may transition from low- to high-quality earlier in

high permeability rock, the trend is still that stronger foam tends to generate in rock with greater permeability (Farajzadeh et al., 2015). Differences in the optimal gas fraction, foam apparent viscosity and foam rheology between limestone and dolomite were insignificant in the corefloods reported here.

Unsteady-state injections of CO₂ into sandstone and carbonate cores saturated with the same surfactant solution showed higher apparent viscosity and earlier foam generation in sandstone compared to limestone (**Figure 2.9**), consistent with observations during the co-injections discussed above. Despite the stronger foam generation in sandstone, increased foam stability was observed in limestone based upon stable apparent viscosity for approximately 4.5 PVs of CO₂ injected. The increased stability in limestone compared to sandstone could be related to lower lamellae coalescence rate at lower pressure drop (lower apparent viscosity) compared to high pressure drop (high apparent viscosity) (Huh & Handy, 1989). In sandstone, foam rapidly collapsed after 0.6 PV of CO₂ injected. The dry-out was likely caused by an abrupt decrease in foaming solution saturation and increased gas fraction.

Calcite dissolution occurred during CO₂ injection into limestone core plugs due to the chemical reactions between CO₂ and the aqueous solution, which resulted in acidic conditions in the core. The dissolution led to changes in permeability and porosity and the generation of new high-permeable pathways. Rock dissolution can positively and negatively impact CO₂ foam flow and will be discussed in Chapter 2.5.

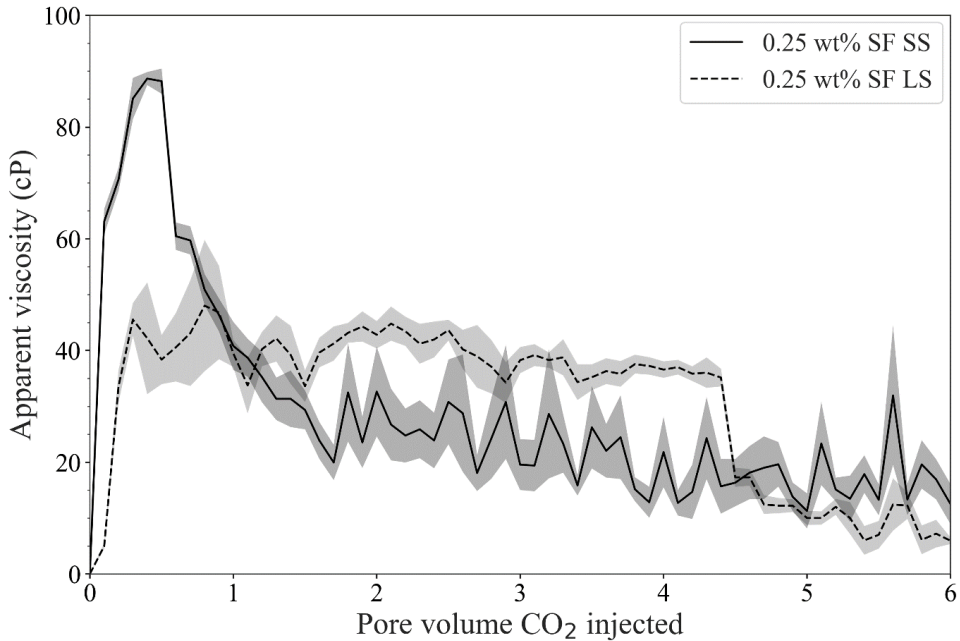


Figure 2.9. Apparent viscosity versus pore volume CO₂ injected in sandstone (solid) and limestone (dashed) saturated with 0.25wt% surfactant solution. The shaded areas represent the uncertainties. Stronger foam was generated in sandstone indicated by higher apparent viscosity. Foam was more stable in limestone as apparent viscosity remained high for six pore volumes injected. Modified from Paper 5.

Foam generation and propagation were also studied using a single injection well radial reservoir simulation model. The foam model parameters of the SAG simulation case were tuned to match the observed pressure response during a recently completed field pilot. The model was then used to evaluate field-scale foam propagation. **Figure 2.10** shows the simulated foam concentration in a 2D slice of the radial model after 1, 5, and 11 SAG cycles. In addition, **Figure 2.10a** shows the permeability distribution in the model derived from history matched sector model (Sharma et al., 2017). The model was heterogeneous, with an average permeability of 13.5 mD and a high permeability layer with permeabilities up to 200 mD. After the first cycle (**Figure 2.10b**), foam propagated nearly 200 ft through the high permeability layer. Foam continued to

propagate until a maximum distance of 400 ft from the injection well, more than halfway to the nearest producer (**Figure 2.10d**).

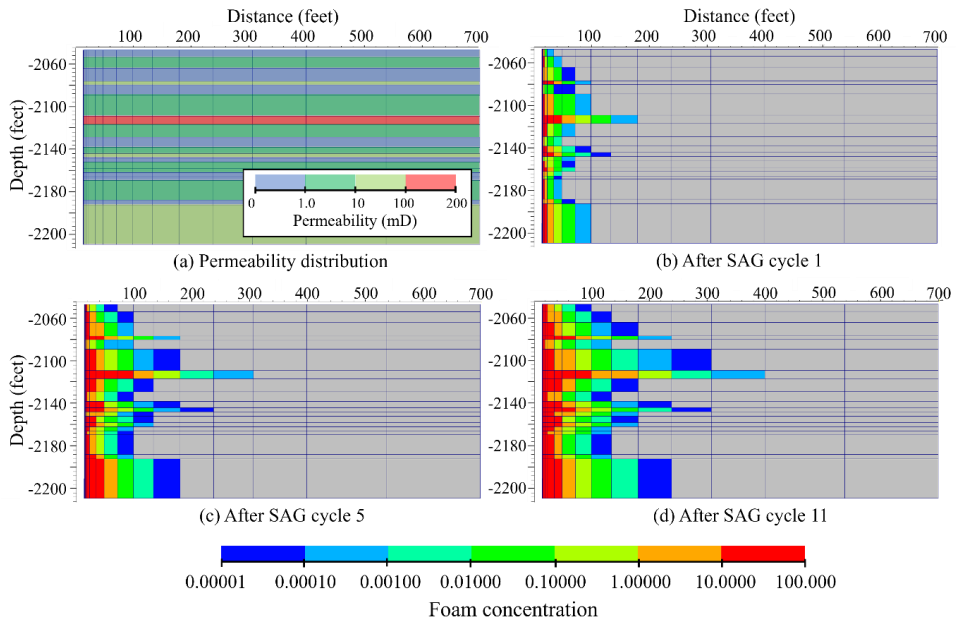


Figure 2.10. (a) Permeability distribution of a 2D slice of the radial simulation model and foam concentration (b) after one surfactant-alternating gas (SAG) cycle, (c) after five SAG cycles and (d) after eleven SAG cycles. Foam propagated through the reservoir from the injection well (left) and 400 ft into the reservoir. Modified from Paper 6.

Foam concentration profiles showed a relation between foam generation, propagation, and rock permeability. CO₂ foam was more readily generated in the higher permeability zones where it propagated furthest because of the lower minimum pressure gradient that had to be exceeded to generate foam (Falls et al., 1989).

The Effect of Surfactant Concentration

Foam generation and stabilization rely on surfactant as a vital component, as it reduces the interfacial tension between CO₂ and brine and stabilizes the lamellae. Selecting a suitable surfactant and its concentration is essential for successful and cost-efficient CO₂ foam application. Generally, stronger foams tend to generate at higher surfactant concentrations (AlYousif et al., 2018). However, increasing the concentration affects

the profitability of large-scale foam processes significantly. Therefore, it is important to determine the impact of surfactant concentration on foam strength and stability.

In this study, the effect of surfactant concentration on foam was investigated through steady- and unsteady-state CO₂ injections at core-scale. A non-ionic, water-soluble surfactant (Surfonic L24-22, *Indorama Ventures*) was dispersed in brine to desired concentrations ranging from 0.10wt% to 0.05wt%. The concentrations exceeded the critical micelle concentration (CMC) of 0.01wt% (Sharma, 2019). The selected surfactant has shown promising effects on foam generation and CO₂ mobility reduction at the laboratory- and field-scale (Alcorn et al., 2022; Rognmo et al., 2019). The surfactant has proven to be flexible because it is applicable in both sandstone and carbonate rocks at a range of reservoir conditions with elevated salinities and temperatures. The Surfonic L24-22 is commercially available and poses no serious threat to the environment (Talmage, 2020).

Steady-state co-injections of CO₂ and foaming solution showed weaker foam with reduced surfactant concentration, indicated by the calculated apparent viscosities (**Figure 2.11**). Reduction of the surfactant concentration from 0.50wt% (red) to 0.25wt% (orange) weakened the foam by approximately 50% at the given experimental conditions. The differences in apparent viscosity were most evident in the low-quality foam regime at gas fractions ranging from 0.3 to 0.6. At gas fractions between 0.5 and 0.6 foam transitioned to the high-quality regime for both solutions, indicating neglectable effect of the studied concentrations on the optimal gas fraction. As the gas fraction increased, the impact of surfactant concentration became less significant and eventually equalized during pure gas injection (gas fraction = 1). A comparison between 0.25wt% foaming solution (orange) and the baseline (black), without foaming agent, showed an increase in apparent viscosity by one order of magnitude. The increased apparent viscosity using 0.25wt% foaming solution compared to baseline and the similar foam strength using 0.25wt% and 0.50wt% solutions at high gas fractions suggest that using a 0.25wt% foaming solution could be adequate for achieving CO₂ mobility reduction at the field-scale.

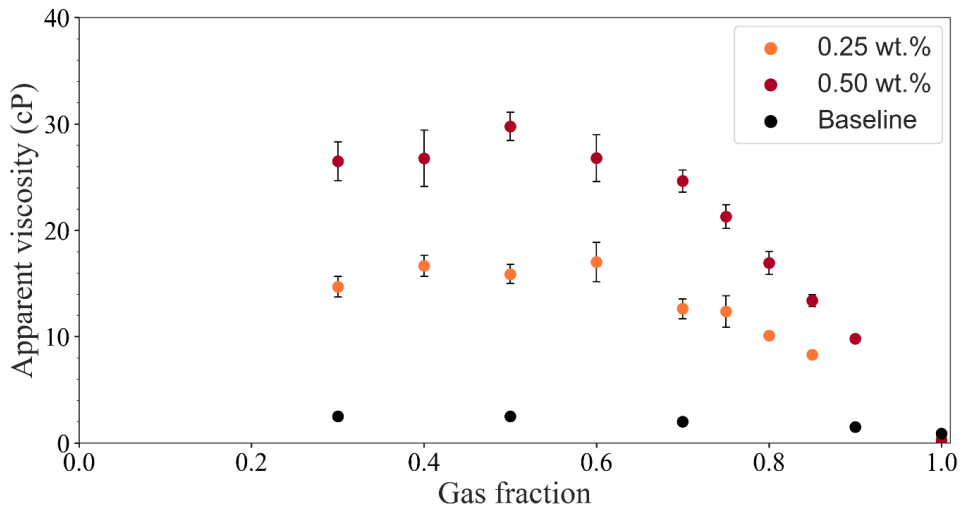


Figure 2.11. Apparent viscosity versus gas fraction during co-injections of CO₂ and brine (black), 0.25wt% (orange) and 0.50wt% (red) surfactant solution at constant injection rate of 4 ft/day at the same experimental conditions. Higher apparent viscosity using higher surfactant concentration indicated generation of stronger foam. Modified from Paper 4.

Unsteady-state CO₂ injections revealed a similar effect of surfactant concentration on foam strength. **Figure 2.12** shows the apparent viscosity versus PV of CO₂ injected for four different surfactant concentrations. An increase in surfactant concentration increased foam strength based upon higher apparent viscosities with more concentrated solutions. Using 0.10wt% solution (**Figure 2.12**, yellow), weak foam with a maximum apparent viscosity of 5 cP was generated, likely because of surfactant adsorption on rock surfaces. The depletion of the surfactant from the liquid phase to the rock surface reduces the concentration of surfactant available to stabilize the foam, resulting in weak foam with lower stability (Jones et al., 2016). Using 0.25, 0.35, and 0.50wt% solutions, the maximum apparent viscosity was 35, 49, and 57 cP, respectively. Yekeen et al. (2017) have also shown increasing foam strength with increasing surfactant concentration due to the increased availability of surfactant molecules at the gas-liquid interface.

Although stronger foam was generated at higher surfactant concentration, it had an insignificant effect on foam stability. Foam rapidly collapsed after reaching a

maximum apparent viscosity at approximately 0.5 PV of CO₂ injected independent of the concentration. After six PVs of CO₂ injected, the apparent viscosities reached similar values for all experiments, indicating a minor influence of surfactant concentration on longer-term mobility reduction. A comparison of foam strength between experiments with 0.50wt% and 0.25wt% solutions demonstrated that foam generation and mobility reduction could be achieved at lower concentrations, which benefit large-scale field operations.

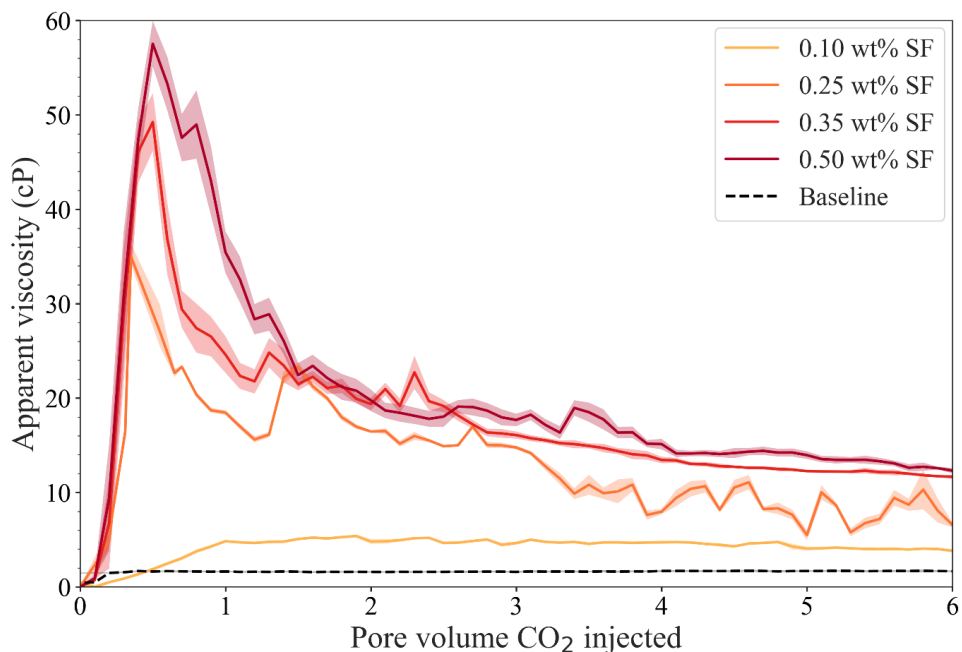


Figure 2.12. Foam strength indicated by apparent viscosity versus pore volume CO₂ injected using four different surfactant concentrations (SF). Baseline (black) was plotted for comparison. The shaded areas represent the uncertainties. The strongest foam was generated using more concentrated solutions, but increased concentration did not improve longer-term CO₂ mobility reduction.

The Effect of Oil

The presence of oil can hinder or delay CO₂ foam generation and reduce foam stability. To assess the impact of oil on foam, pore- and core-scale unsteady-state CO₂ injections were conducted at reservoir conditions. Before CO₂ injections, the porous media was saturated with first-contact miscible mineral oil, n-Decane, followed by brine or surfactant injection to displace the oil and reach desired residual oil saturation.

Pore-scale CO₂ injections were performed at 100 bars and 25°C. At these conditions CO₂ was in liquid phase and was miscible with n-Decane. Three stages of CO₂ injection into a micromodel saturated with hybrid nanoparticle-surfactant solution and oil are shown in **Figure 2.13**. Before CO₂ injection, the porous media was filled with a continuous liquid phase consisting of a foaming solution and isolated oil droplets (**Figure 2.13a**). As the CO₂ injection started, the oil droplets faded due to miscibility between CO₂ and oil (**Figure 2.13b**). During CO₂ injection, most of the oil was displaced by CO₂, and foam was generated in areas without oil present. In addition, oil-in-water emulsions were generated in oil-filled pores without foam present. Foam and oil-in-water emulsions were distinguished based on lamella thickness. Bubbles with thinner lamellae characterized oil-in-water emulsions, whereas thicker lamellae indicated CO₂ foam. Visual image analysis showed that residual oil did not hinder CO₂ foam generation. Images did not show generation of open flow channels, as observed during injections without oil (**Figure 2.4**), suggesting that the combination of CO₂ foam and oil-in-water emulsion impeded CO₂ flow pathways and contributed to CO₂ mobility reduction.

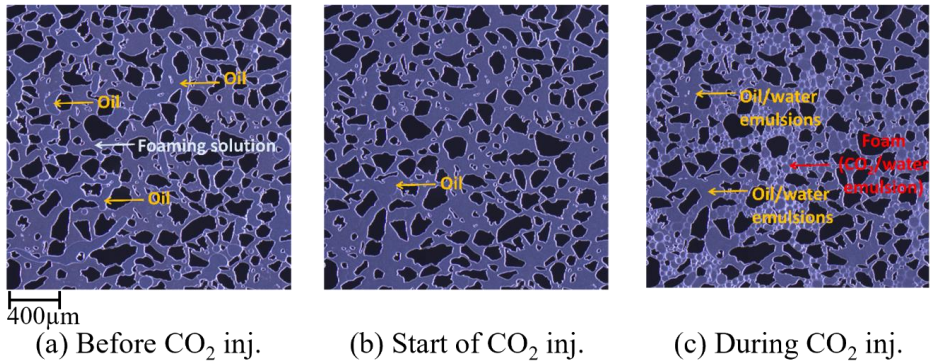


Figure 2.13. Pore-scale images of a focused field of view during CO₂ injection into a micromodel saturated with hybrid foaming solution (0.50wt% surfactant + 0.15wt% nanoparticles) and n-Decane. Three stages of the injection are shown: (a) before CO₂ injection, (b) start of CO₂ injection, and (c) during CO₂ injection. The black and purple areas are grains and pore space, respectively. The thin white films are the lamellae. Modified from Paper 1.

The residual oil did not hinder foam generation during unsteady state CO₂ injection into a core saturated with 0.50wt% surfactant solution and n-Decane, indicated by a rapid increase in apparent viscosity (**Figure 2.14**). In the presence of residual oil (red curve), the apparent viscosity was two times higher than without oil (black dashed curve). The combined effect of oil-in-water emulsions and CO₂ foam increased CO₂ flow resistance and increased the apparent viscosity. The oil-in-water emulsions were observed in the effluent and were consistent with pore-scale observations.

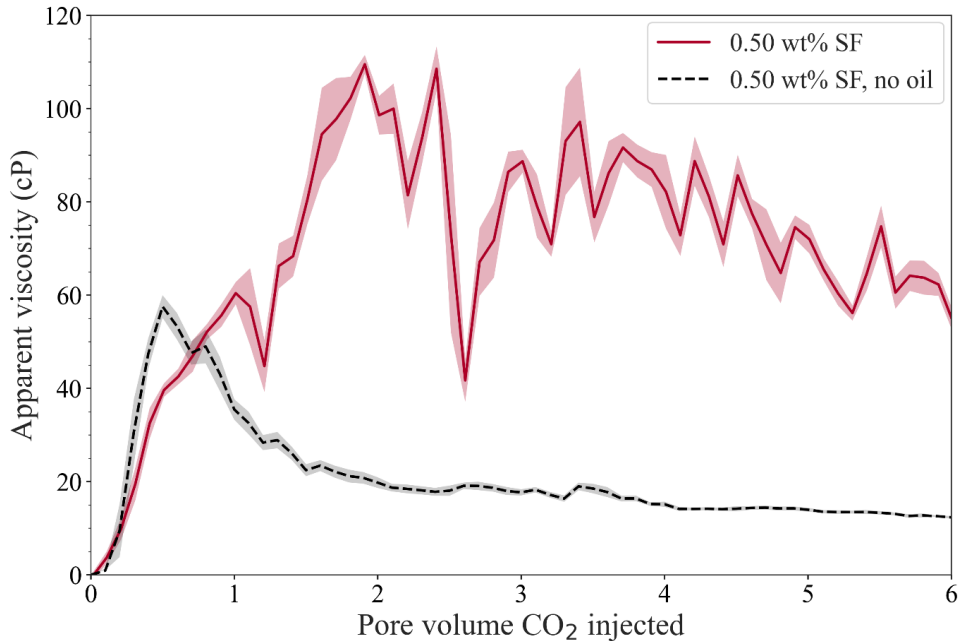


Figure 2.14. Apparent viscosity versus pore volume CO_2 injected during single-cycle CO_2 injection into sandstone core plug saturated with surfactant foaming solution (SF) and residual oil saturation of 30% (red). A similar experiment without oil present (dashed curve) was plotted for comparison. The shaded areas represent uncertainties. Modified from Paper 1.

Pore- and core-scale observations showed that a residual oil saturation of approximately 30% did not hinder or destabilize CO_2 foam. At the field-scale, generation of oil-in-water emulsion in addition to CO_2 foam may enhance oil recovery and increase CO_2 storage capacity by increasing the viscous displacement forces and reducing interfacial tension, hence increasing the capillary number (Simjoo et al., 2012).

The effect of higher oil saturation on foam was also evaluated through cyclic CO_2 and surfactant injections (SAG) into sandstone core plugs with oil saturations of approximately 60 to 70%. For comparison, cyclic injection of brine and CO_2 (WAG) was also performed. **Figure 2.15** shows apparent viscosity versus PVs injected for WAG (blue) and SAG (red) injection processes. A total of 18 cycles consisting of one brine or foaming solution slug and one CO_2 slug with a volumetric ratio of 0.60 were

performed, followed by a prolonged CO₂ injection period. During the first five cycles, the apparent viscosity fluctuated between 1 and 4.5 cP in both experiments. The fluctuation was due to the difference in viscosities of the alternating fluids. During gas injection, the apparent viscosity increased up to 4.5 cP because of gas relative permeability reduction at high water saturations. During WAG injection, oil-in-water emulsions were generated indicated by two times higher apparent viscosities compared to WAG in the absence of oil (**Paper 6**). Foam was not generated during WAG because of lack of foaming solution.

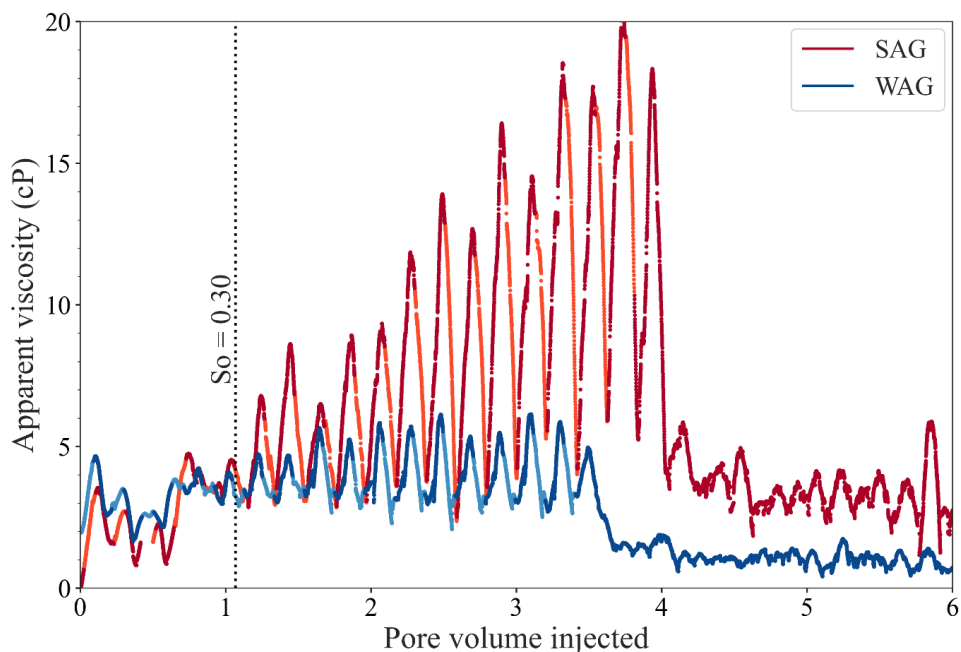


Figure 2.15. Apparent viscosity versus pore volume CO₂ injected during water-alternating gas (WAG, blue) and surfactant-alternating gas (SAG, red) injection into core plugs with 60 to 70% oil saturation. Light and dark colors represent brine/foaming solution and CO₂ slugs, respectively. Modified from Paper 4.

During SAG injection (**Figure 2.15**, red), foam generation started during the sixth cycle, indicated by a gradual increase in apparent viscosity. Most of the oil was displaced after 1 PV injected, and the oil saturation was reduced from 68% to 30% before foam generation started. The high amount of mobile oil in the core hindered

foam generation until the oil saturation was below a critical limiting saturation, as previously reported by Friedmann and Jensen (1986) and Mannhardt et al. (1998). The limiting n-Decane saturation was 0.30 during SAG injections into Bentheimer sandstone at 180 bars, 40°C and using a non-ionic surfactant as foaming solution. In addition to foam, oil-in-water emulsions stabilized by the foaming agent were generated.

2.3 Nanoparticle-Stabilized Foams

The addition of silica nanoparticles to the surfactant-based foam has gained attention for increasing its strength and stability and improving CO₂ EOR and CO₂ storage (Mo et al., 2012). Pore- and core-scale CO₂ injections representative of field-scale injections in the near-wellbore area investigated the effect of nanoparticles on foam at different reservoir conditions (**Papers 1 and 3**).

Nanoparticles as Foam Stabilizers

Silica nanoparticles and a combination of silica nanoparticles and a non-ionic, water-soluble surfactant were used as foaming agents to study the stabilizing effect of nanoparticles on foam at reservoir conditions. Pore-scale experiments gained insight into foam generation and coalescence dynamics compared to surfactant-based foam. **Figure 2.16** shows the normalized number of bubbles versus PVs of CO₂ injected during CO₂ injection into a micromodel saturated with four foaming solutions at pore-scale. The bubble generation and destabilization were similar using 0.50wt% surfactant solution and hybrid solutions containing 0.50wt% surfactant with 0.015wt% (light green curve) or 0.15wt% (dark green curve) nanoparticles. For all solutions containing surfactant, the bubble number increased approximately ten to eleven times compared to the baseline. After reaching the maximum foam generation after 7-10 PVs of CO₂ injected, the bubble number decreased due to bubble coarsening. After 60 PVs of CO₂ injected, the number of bubbles remained slightly higher using the hybrid solutions. The impact of silica nanoparticles on bubble number and stability was considered limited.

Furthermore, a comparison between the two hybrid solutions demonstrated that the nanoparticle concentration had a negligible effect on the bubble texture and foam stability when combined with the selected surfactant. Using only nanoparticles (**Figure 2.16**, black curve) as the foaming agent did not generate foam, indicated by the low number of bubbles and continuous distribution of open CO₂ flow paths. As a result, CO₂ mobility remained high, similar to the baseline without foaming solution. The observations indicated that surfactant was the main foam generator, whereas nanoparticles could be more important for foam stabilization.

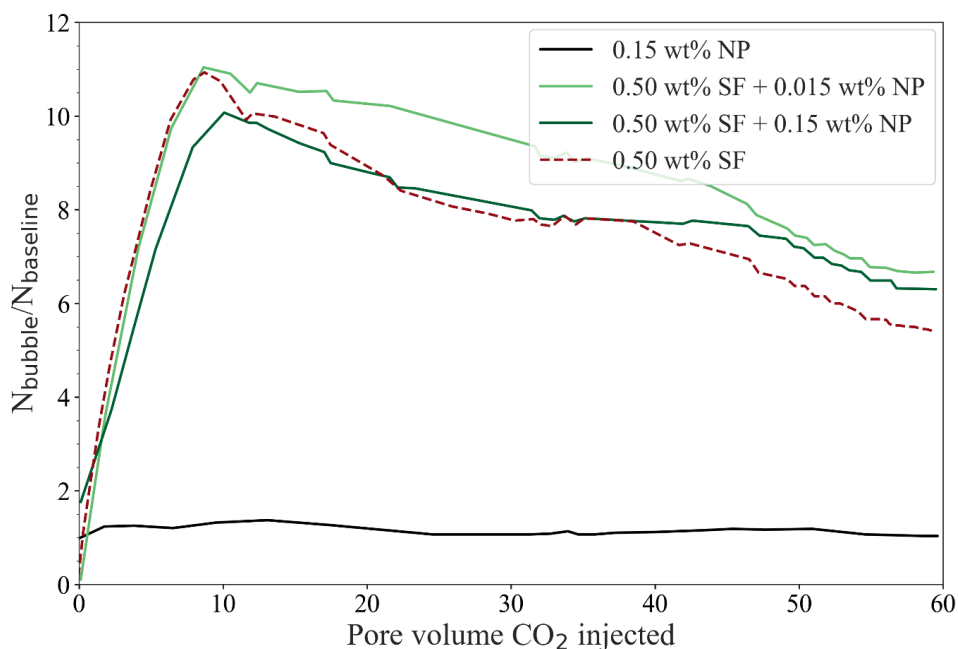


Figure 2.16. Bubble number (N_{bubble}) normalized to baseline (N_{baseline}) as a function of PV CO₂ injected for nanoparticle (black) and two hybrid foaming solutions: 0.50wt% surfactant (SF) + 0.015wt% nanoparticles (NP) (light green) and 0.50wt% surfactant + 0.15wt% nanoparticles (dark green). 0.50wt% surfactant solution (red dashed) was plotted for comparison. The presence of nanoparticles had a minor impact on the number of bubbles and their stability. The nanoparticle-based solution did not generate foam based on the low number of bubbles. Modified from Paper 1.

Core-scale CO₂ injections revealed similar observations as at the pore-scale and showed insignificant effects of nanoparticles on foam strength and stability. **Figure 2.17** shows the apparent viscosity versus PVs of CO₂ injected for two hybrid solutions (green curves) and a surfactant solution for comparison (red dashed curve). Foam generation rate, apparent viscosity, and foam destabilization rate were similar for all three solutions, suggesting a negligible impact of nanoparticles when combined with the selected surfactant. Foam strength was also unaffected by nanoparticle concentration, as increasing the concentration from 0.015wt% to 0.15wt% did not show significant differences. A more evident effect of nanoparticles is expected at harsh reservoir conditions at which the stability of the surfactant solution is reduced.

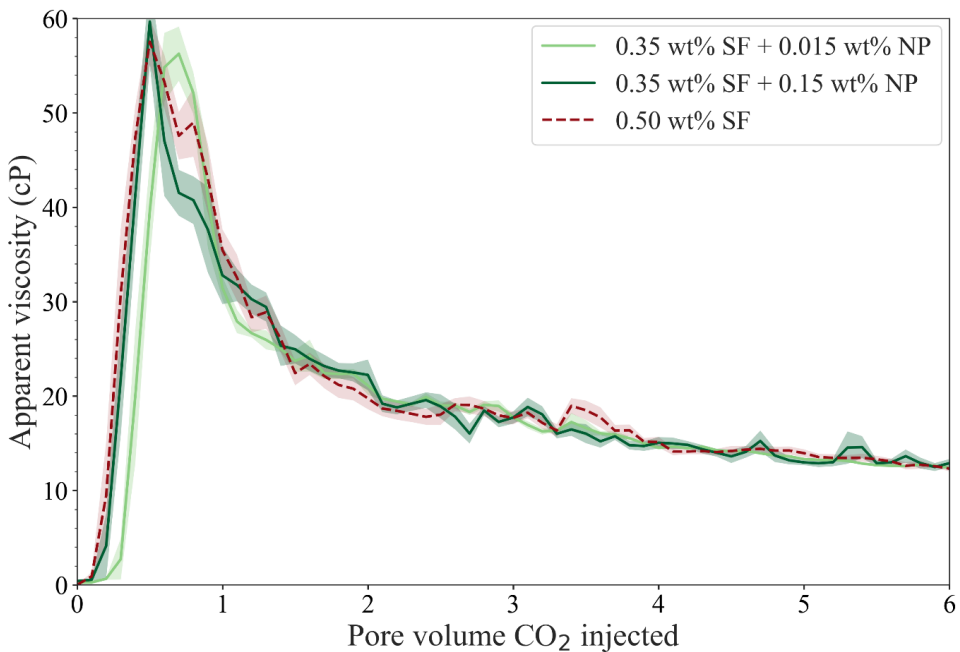


Figure 2.17. Apparent viscosity versus pore volume CO₂ injected during unsteady-state CO₂ injection into core saturated with hybrid nanoparticle-surfactant foaming solution. Two hybrid solutions were tested: 0.35wt% surfactant (SF) + 0.015wt% nanoparticles (NP) (light green) and 0.35 wt% surfactant + 0.15wt% nanoparticles (dark green). Surfactant solution was plotted for comparison (red). The shaded areas represent the uncertainties. Modified from Paper 1.

The hybrid solution containing 0.35wt% surfactant and 0.015wt% nanoparticles generated equally strong and stable foam as the other solutions with higher total concentrations. This observation indicated that the concentration of the foaming solution can be reduced without affecting foam strength. Reducing concentration is advantageous for large-scale applications as the chemical costs may be reduced.

Nanoparticle Stabilized Foam at Elevated Salinities

The ability to generate and stabilize surfactant-based foam decreases with increasing salinity, primarily due to the chemical instability of surfactant solutions. The addition of nanoparticles may prolong the lifetime of surfactant-based foam at harsh reservoir conditions with elevated temperatures and salinities. Therefore, hybrid nanoparticle-surfactant stabilized foam was evaluated at high salinity of 15wt% NaCl and compared to results at lower salinity of 3.5wt% NaCl (**Paper 3**).

The aqueous stability of hybrid, surfactant, and nanoparticle solutions in bulk was evaluated at 25 and 40 °C and a range of pH values before injections into porous media (**Paper 3**). Surfactant and nanoparticle solutions demonstrated stability throughout the testing duration at both low and high salinity, irrespective of temperature and pH. However, the stability of hybrid solutions was influenced by the elevated salinities. At low salinity, the hybrid solution remained stable for three months, regardless of temperature or pH values. Over time, irreversible precipitation in the hybrid solution occurred, possibly due to particle aggregation.

In contrast, at high salinities, the hybrid solution was unstable at pH values below nine indicated by rapid precipitation. The instability may have resulted from interactions between the ethylate oxide (EO) parts of the non-ionic surfactant and the nanoparticles (Bharti, 2014). However, as pH increased or the salinity decreased, the aggregates were redispersed, suggesting that the precipitation stemmed from flocculation rather than aggregation. Only stable solutions were used during pore- and core- scale foam experiments to prevent clogging of the porous media.

The influence of salinity on CO₂ foam stabilized by surfactant and hybrid solutions was examined through qualitative and quantitative pore-scale image analysis. The results revealed stronger foam generation at high salinity compared to low salinity, indicated

by a higher number of bubbles (**Figure 2.18**). Comparing surfactant-stabilized (red curves) and hybrid-stabilized (green curves) foams showed similar generation dynamics and stability at low salinity, indicated by a similar number of bubbles. However, at high salinity, the hybrid solution showed a minor impact on foam strength as the number of bubbles increased by 20% compared to only the surfactant solution.

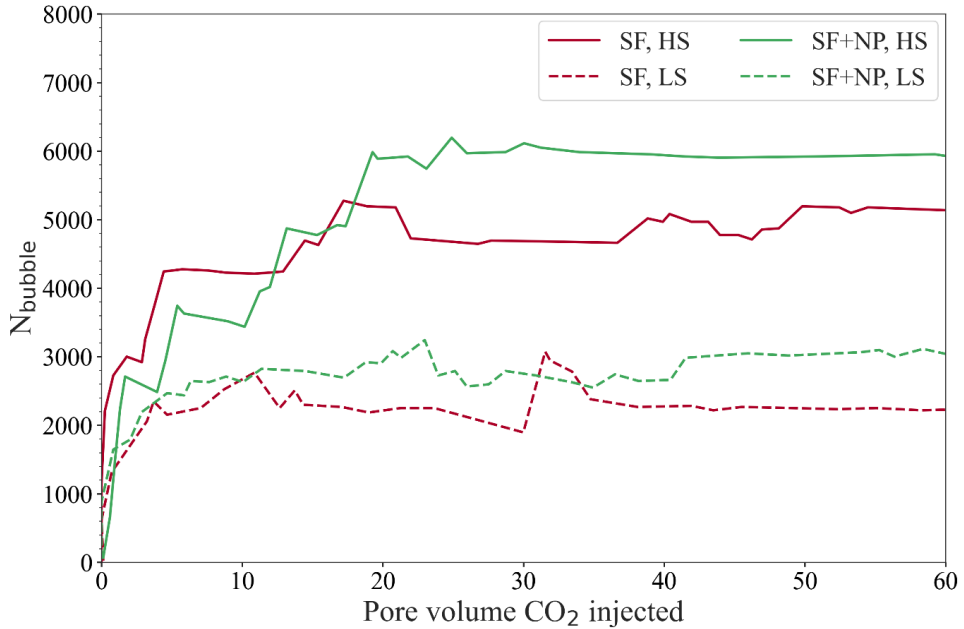


Figure 2.18. The number of bubbles versus pore volume CO₂ injected using surfactant (SF, red) and hybrid (SF + NP, green) foaming solution at low and high salinities. Solid and dashed lines represent 15wt% and 3.5wt% NaCl, respectively. Modified from Paper 3.

Observations of a focused field of view showed that for both solutions at high salinity, smaller isolated bubbles were generated (**Figure 2.19a**, orange), and several small bubbles accumulated in individual pores (**Figure 2.19a**, orange circle). The isolated bubbles reduced CO₂ relative permeability, diverted CO₂ flow, and improved sweep efficiency, as observed during core-scale CO₂ foam injections (**Figure 2.20**). At low salinity, a few large bubbles spanning across several pores were observed (**Figure 2.19b**, green). The continuous bubbles provided little flow resistance, and the gas remained a continuous phase, which resulted in poor sweep efficiency. The difference in bubble size was likely caused by the changes in the surface tension of water as

salinity increased (Behera et al., 2014). Finer-textured foam was generated at 15wt% compared to 3.5wt% salinity, indicating that increased salinity did not hinder foam generation or have a detrimental effect on foam stability.

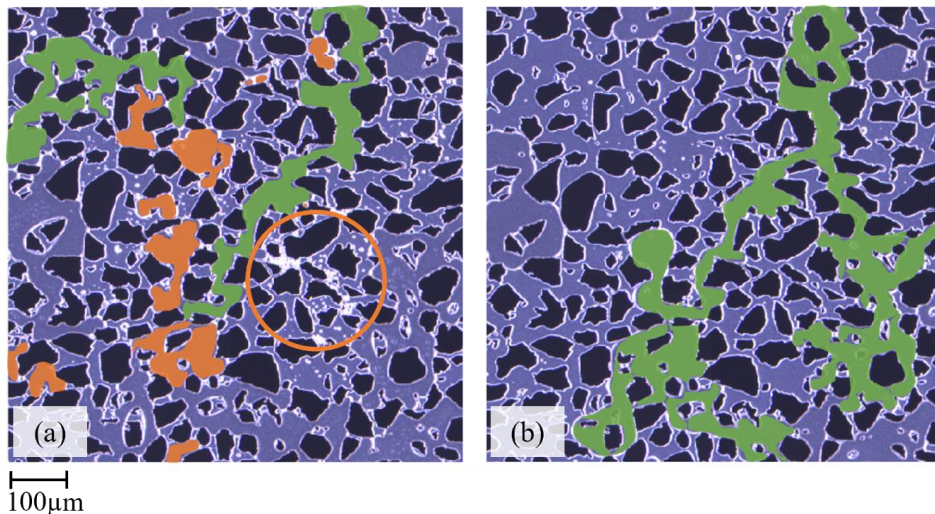


Figure 2.19. Pore-scale images of a focused field of view ($2200\mu\text{m} \times 2200 \mu\text{m}$) at (a) high salinity and (b) low salinity. Orange areas represent smaller isolated bubbles. The green areas represent large continuous bubbles spanning across several pores. At high salinity, accumulation of small bubbles in several pores was observed, marked with the circle. Only a fraction of continuous bubbles was colored for visualization. Modified from Paper 3.

The impact of salinity on foam was assessed through core-scale CO_2 injections performed in Bentheimer sandstone cores saturated with low or high salinity brine. Prior to CO_2 injection, 0.4 PV of either surfactant or hybrid solution, dispersed in low or high salinity brine, was injected into the core. The injection scheme followed a single-cycle SAG injection representative of near-wellbore injections at the field-scale. The effect of salinity on hybrid- and surfactant-based foams was evaluated based on the apparent viscosity and water displacement efficiency.

Figure 2.20 shows the end-point water saturation for surfactant- and hybrid-based foams at low and high salinity conditions and the baseline. A lower end-point water saturation compared to the baseline indicated improved displacement efficiency, whereas a higher water saturation indicated poor sweep efficiency. Weak foams were

generated at low salinity indicated by low maximum apparent viscosity of approximately 7 cP for both solutions. Increased salinity hindered the generation of hybrid-based foam, indicated by the low apparent viscosity (2.8 ± 0.3 cP), similar to the baseline (1.9 ± 0.1 cP). The lack of foam generation was likely caused by interactions between the ethylene oxide (EO) components of the surfactant and the silica nanoparticles, leading to precipitation and an unstable aqueous solution. In contrast, high salinity did not destabilize the surfactant-based foam, indicated by maximum apparent viscosity of 21.2 ± 0.5 cP. Furthermore, the increased salinity improved water displacement for surfactant- and hybrid-based foams. The improved water displacement using the hybrid solution could be attributed to increased viscous forces resulting from the precipitation of the chemicals.

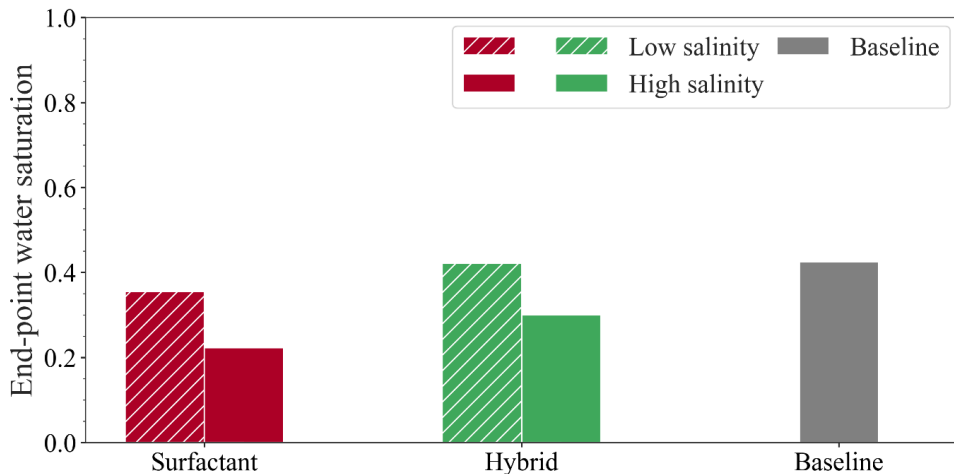


Figure 2.20. End-point water saturation for unsteady-state CO₂ injections at low (dashed) and high (solid) salinities using surfactant (red) and hybrid (green) foaming solution. The baseline was performed at low salinity (gray). Increased salinity improved water displacement. Modified from Paper 3.

Comparing the performance of surfactant- and hybrid-stabilized foams revealed similar generation dynamics and stability, suggesting that the nanoparticles had an insignificant effect on foam properties. The non-ionic surfactant demonstrated stability under experimental conditions and was considered the main foam generator. The limited contribution of nanoparticles to stabilize foam may be related to the surfactant

concentration, as high concentrations tend to displace nanoparticles from the air-water interface (Pichot et al., 2012). In addition, Ma et al. (2008) reported that adding silica nanoparticles to non-ionic surfactant solutions had minimal impact on reducing the surface tension of the air-water interface due to weak interactions between the non-ionic surfactant and the negatively charged nanoparticles. Combining silica nanoparticles with anionic surfactant could enhance foam stability due to repulsive forces that promote surfactant adsorption at the air-water interface, effectively reducing the surface tension (Ma et al., 2008).

2.4 CO₂ Foam for EOR

CO₂ foam for EOR provides several benefits, such as reduced CO₂ mobility, improved sweep efficiency, improved economic viability of the process, and the opportunity for simultaneous storage of CO₂, contributing to greenhouse gas reduction (Enick et al., 2012; Rossen et al., 2022). This work investigated the efficiency of different CO₂ injection methods and the impact of surfactant concentration and rock permeability on EOR.

CO₂ Injection Methods

Six different unsteady-state CO₂ injection methods at the core-scale were performed and compared to study their efficiency in enhancing oil recovery. Pure CO₂ injection, WAG, single-cycle SAG, and multi-cycle SAG were implemented after waterflood, at residual oil saturation of approximately 30%, and after drainage, at oil saturation of approximately 70%. Oil recovery for the different injections is shown in **Figure 2.21**.

Pure CO₂ injection after waterflood (**Figure 2.21**, light blue) resulted in the lowest oil recovery because of an unfavorable mobility ratio between CO₂ and other fluids, which led to early gas breakthrough and poor sweep efficiency. 45% of OOIP was recovered during the initial waterflood, and an additional 8% was recovered during CO₂ injection. At the experimental conditions, CO₂ was first-contact miscible with n-Decane, and higher recovery was expected (Song et al., 2011). The low recovery was likely a result of water shielding, a phenomenon where oil droplets are trapped within the water phase and are not in contact with CO₂ (Müller & Lake, 1991; Shelton & Schneider, 1975). The relatively short injection period did not allow enough time for CO₂ to diffuse through the water phase, swell the oil and increase the recovery.

Implementation of WAG after the initial waterflood (**Figure 2.21**, dark blue) enhanced oil recovery, with an additional 15% of oil being recovered. The cyclic injections of brine and CO₂ improved mobility control by reducing CO₂ relative permeability in the presence of high water saturation, thereby mitigating gas channeling and delaying gas breakthrough. Furthermore, alternating between two fluids with varying densities and viscosities improved the macroscopic sweep efficiency. WAG was also implemented

directly after drainage (**Figure 2.21**, dark blue, dashed), without an initial waterflood, at an oil saturation of approximately 70%. This injection method resulted in oil recovery of $71 \pm 3\%$ compared to $66 \pm 6\%$ for WAG after the waterflood. Increased oil recovery was due to generation of weak oil-in-water emulsions which improved the displacement. The results indicated that implementing WAG at the early stage of oil production improved the recovery. However, the operational constraints and costs compared to the revenue from increased production should be considered before choosing the optimal injection procedure.

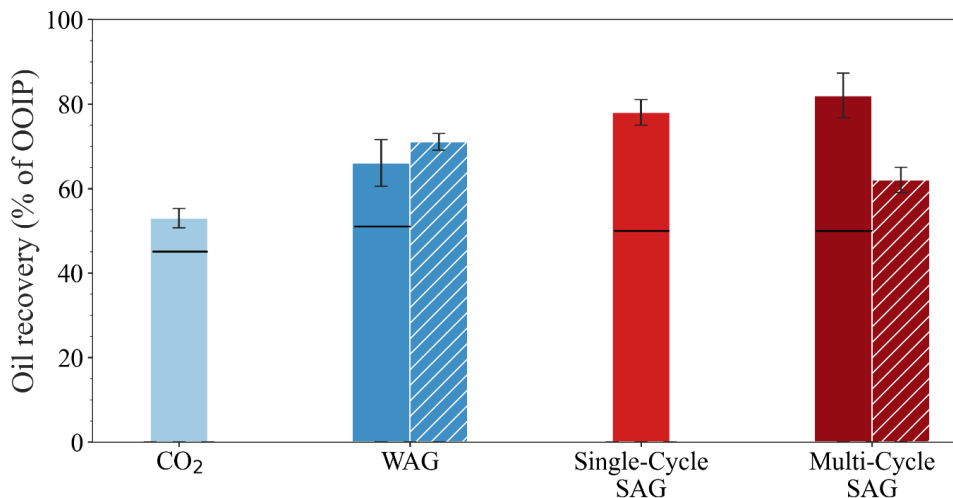


Figure 2.21. Oil recovery factors pure CO₂ injection, water-alternating gas (WAG) and surfactant-alternating gas (SAG) after waterflood (solid bars) and after drainage (dashed bars). The black horizontal lines mark oil recovery during waterflood. Recovery above the line represents additional recovery governed by implementing an EOR method.

Oil recovery was further increased with CO₂ foam during single- and multi-cycle SAG injections. During single-cycle SAG (**Figure 2.21**, light red), one slug of foaming solution was injected (1 PV) into the core prior to CO₂ injection. Approximately 50% of OOIP was recovered during surfactant injection, resulting in an oil saturation of 30% at the start of CO₂ injection. As CO₂ injection started, the foam rapidly generated, leading to reduced CO₂ mobility, improved displacement efficiency, and increased oil recovery. In total, $78 \pm 3\%$ of OOIP was recovered. Comparing single-cycle SAG with

pure CO₂ injection showed a nearly 50% increase in oil recovery due to foam generation.

Multi-cycle SAG included 18 cycles, each consisting of a foaming solution slug and a CO₂ slug with a volumetric ratio (foam quality) between the slugs of 0.60. Multi-cycle SAG was performed after the initial waterflood (**Figure 2.21**, dark red) at an oil saturation of approximately 30% and directly after drainage (**Figure 2.21**, dark red, dashed) at a higher oil saturation of approximately 70%. Strong foam generation during multi-cycle SAG improved oil recovery and $82 \pm 3\%$ OOIP was recovered. Performing multi-cycle SAG directly after drainage did not improve oil recovery and resulted in lower oil recovery, likely due to delayed foam generation at high oil saturation observed and discussed in Chapter 2.2.

Overall, multi-cycle SAG performed after the initial waterflood proved to be the most effective method to increase oil recovery at the experimental conditions, followed by single-cycle SAG and WAG. WAG and multi-cycle SAG followed the same procedure with the same number and size of cycles. The presence of surfactant and foam generation during SAG led to improved oil recovery by approximately 24%.

The Effect of Foam Strength on CO₂ EOR

Foam strength and stability is influenced by the surfactant concentration. Core-flood experiments showed that stronger foam could be generated with higher surfactant concentration (**Figure 2.12**). **Figure 2.22** shows oil recovery for two multi-cycle SAG injections performed after waterflood, one with 0.25wt% (orange) surfactant and one with 0.50wt% (red) surfactant and corresponding apparent viscosities on the secondary y-axis. Using 0.50wt% solution, apparent viscosity reached a maximum value of 48 cP, whereas using 0.25wt% the maximum apparent viscosity was 15 cP. Despite stronger foam generation using higher surfactant concentration, the difference in oil recovery was insignificant and within the uncertainty range. $85 \pm 5\%$ and $82 \pm 4\%$ of OOIP was recovered using high and low surfactant concentration, respectively. Similar has been observed by Alcorn et al. (2019) where reducing surfactant concentration from 1 wt% to 0.50 wt% did not reduce the efficiency of foam for CO₂ EOR.

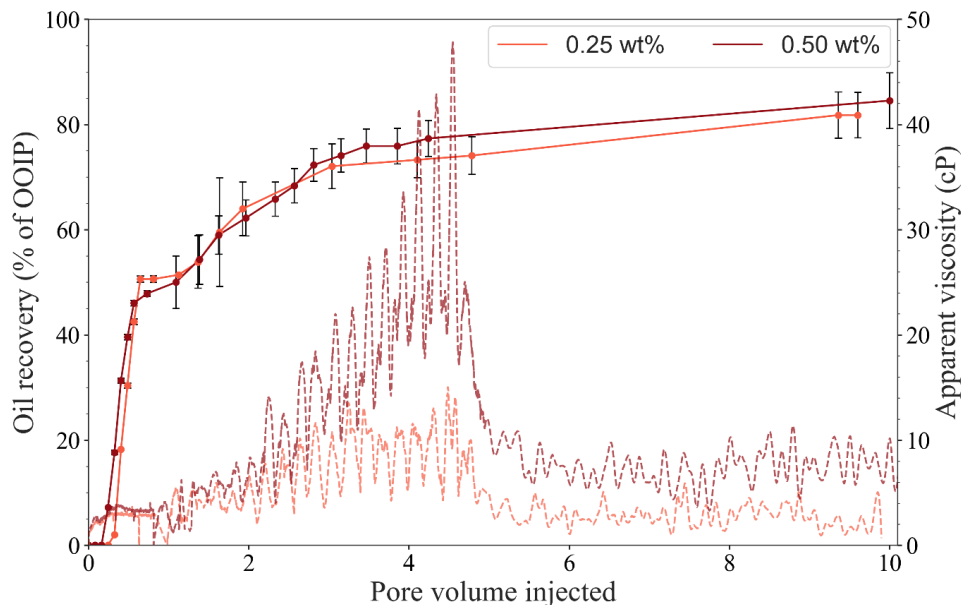


Figure 2.22. Oil recovery during multi-cycle SAG injection using 0.25wt% (orange) and 0.50wt% (red) foaming solution. Corresponding apparent viscosity was plotted on secondary y-axis. Similar amount ($85 \pm 5\%$ and $82 \pm 4\%$) of oil was recovered using low and high concentrated surfactant solutions despite differences in apparent viscosity. Modified from Paper 4.

At the field-scale, stronger foam might improve oil recovery compared to weaker foam as the fluid flow is impacted by gravitational segregation and reservoir heterogeneity, phenomena not accounted for at the core-scale. For optimal CO_2 foam EOR application at the field-scale, surfactant type and concentration should be carefully selected. Reducing the surfactant concentration without reducing the efficiency of foam is economically beneficial for designing field-scale foam systems as the operational costs may be reduced.

CO₂ Foam EOR in Sandstone and Carbonate

The efficiency of CO₂ foam on enhanced oil recovery depends on the petrophysical properties of the rock. Oil displacement is challenged by reservoir heterogeneity as the injected fluids flow through high permeability zones and leave behind large amount of oil in the unswept lower permeability zones (Ding et al., 2017). Foaming CO₂ may block the high permeability zones, divert flow into unswept regions of the reservoir and improve the displacement. Previous results showed the effect of rock permeability on foam strength and stability, where stronger foam was generated in homogeneous sandstone core compared to heterogeneous limestone core (**Figure 2.9**). Pure CO₂ injection and single-cycle SAG were performed in sandstone and limestone cores to investigate oil displacement differences in the two rocks.

The oil recovery versus PV of CO₂ injected is presented in **Figure 2.23**. Prior to CO₂ injection, a waterflood or surfactant injection was performed to displace the oil and reach a residual oil saturation. In sandstone, approximately 1.3 PVs of brine or surfactant solution were injected, and $45 \pm 2\%$ of OOIP was recovered, whereas in limestone, approximately 2.3 PVs of brine or surfactant solution were injected, resulting in $42 \pm 2\%$ of OOIP recovered. During pure CO₂ injection, low oil recovery was observed in both rocks and only 7 – 8% of additional oil was recovered, resulting in a total oil recovery of $53 \pm 1\%$ and $49 \pm 2\%$ in sandstone (**Figure 2.23**, red dashed) and limestone (**Figure 2.23**, orange dashed), respectively. Poor displacement was caused by unfavorable mobility ratio between CO₂ and other reservoir fluids, which led to gas channeling and early CO₂ breakthrough. In addition, the cores were strongly water-wet and oil droplets were likely trapped within the water phase and not in contact with CO₂ (Müller & Lake, 1991; Shelton & Schneider, 1975). The effect of rock type showed a minor effect on oil displacement during pure CO₂ injection. Lower total oil recovery in limestone compared to sandstone was mainly caused by lower displacement during the initial waterflood due to more heterogeneities in the limestone core.

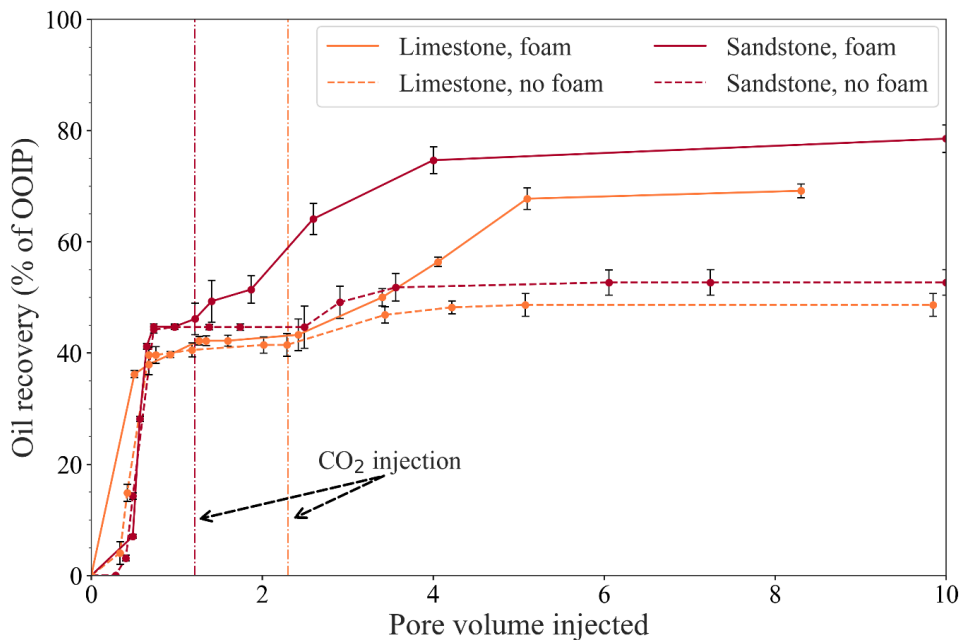


Figure 2.23. Oil recovery factor versus pore volume injected for pure CO₂ injection (dashed) and single-cycle SAG (solid) in limestone (orange) and sandstone (red) core plugs. The vertical lines represent the start of CO₂ injection after waterflood or surfactant injection. Modified from Paper 5.

Mobility control by CO₂ foam improved oil recovery in both cores and approximately 30% of additional oil was recovered. The total oil recovery during CO₂ foam EOR was $79 \pm 2\%$ and $69 \pm 1\%$ in sandstone (**Figure 2.23**, red) and limestone (**Figure 2.23**, orange), respectively. The difference in the total recovery was a result of lower oil displacement during the initial waterflood in limestone compared to sandstone. In addition, generation of stronger foam in sandstone compared to limestone likely improved the sweep efficiency. Comparison between pure CO₂ injection and CO₂ foam EOR showed an increase in oil recovery by 50% in sandstone and 42% in limestone.

2.5 Foam-Assisted CO₂ Storage

Mobility control using CO₂ foam can increase the potential CO₂ storage capacity in underground geological formations compared to pure CO₂ injection. Core-scale CO₂ storage capacity was estimated based on measurements of fluid production and mass-balance equation during various CO₂ EOR injections (**Papers 4 and 5**). CO₂ storage capacity for pure CO₂ injection, WAGs, and SAGs after waterflood and after drainage is shown in **Figure 2.24**. The values are the minimum estimated capacities as the calculations did not consider CO₂ dissolved in water- and oil-phase (Zhang & Song, 2014). An increase in the potential CO₂ storage capacity was observed when CO₂ mobility control technique was implemented, compared to pure CO₂ injection.

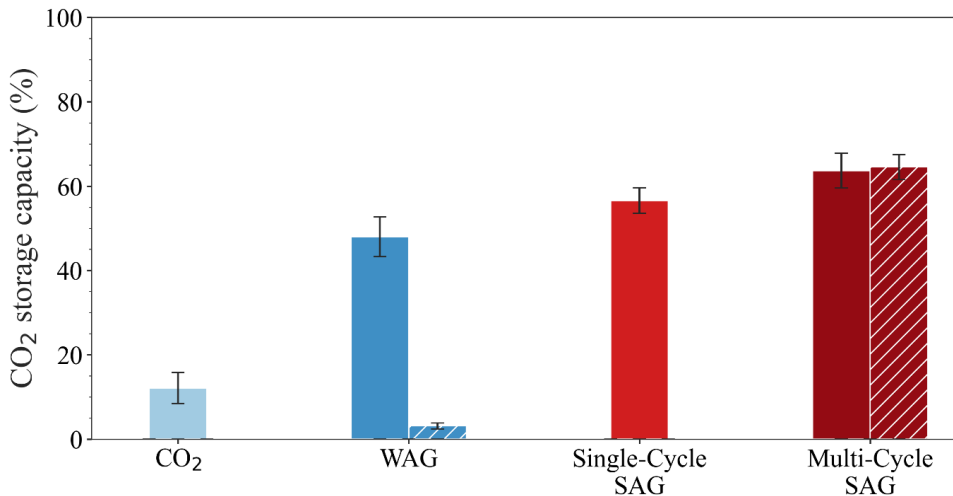


Figure 2.24. CO₂ storage capacity of various CO₂ injection methods. The experiments were performed after waterflood (solid bars) and after drainage (dashed bars). Low storage capacity was achieved during pure CO₂ injection, whereas decreasing CO₂ mobility through WAG and SAG increased the storage capacity.

During pure CO₂ injection (**Figure 2.24**, light blue), 12% of pore volume was occupied by CO₂, which was considered as low storage capacity. The low storage capacity was related to the high mobility ratio between CO₂ and other fluids which led to early gas breakthrough and generation of open CO₂ flow paths. Implementation of WAG after waterflood (**Figure 2.24**, dark blue) for mobility control increased the storage capacity

by 300%, corresponding to a storage capacity of approximately 50%. Performing WAG after drainage (**Figure 2.24**, blue dashed), only small amount of CO₂ remained trapped in the core and the estimated storage potential was 3%. The low storage capacity was related to poor water displacement. The water saturation in the core increased from 0.33 after drainage to 0.78 after completed WAG and most of the injected CO₂ was produced with the oil.

Single-cycle SAG injection (**Figure 2.24**, light red) showed increased CO₂ storage capacity and $56 \pm 3\%$ of PV was saturated with CO₂ after the experiments. Foam generation during SAG improved the displacement efficiency of oil and water, leaving more pore space available to store CO₂. Changing the injection strategy to multi-cycle SAG (**Figure 2.24**, dark red) resulted in further improvement of the storage capacity to $64 \pm 4\%$, because of stronger foam generation, which improved water displacement. Performing multi-cycle SAG after drainage SAG (**Figure 2.24**, red dashed) showed similar results as multi-cycle SAG after the waterflood indicated by the estimated CO₂ storage capacity of $66 \pm 3\%$. The minor increase in storage capacity during SAG after drainage compared to SAG after waterflood was due to the generation of oil-in-water emulsions which increased the viscous forces and improved the displacement (Simjoo et al., 2012).

Overall, foam generation increased the storage capacity up to 420% compared to pure CO₂ injection. The increase in storage capacity was related to the generation of trapped CO₂ bubbles during SAG injections, as observed at the pore-scale (**Figure 2.2**), which remained immobile in the pores for several pore volumes of CO₂ injected. In addition, the trapped bubbles diverted CO₂ flow, reduced CO₂ relative permeability and improved water and oil displacement resulting in more pore space available for storage. During pure CO₂ injection, CO₂ remained a mobile and continuous phase which resulted in poor displacement and limited CO₂ storage capacity.

***In-Situ* Imaging – CO₂ Displacement Efficiency for CO₂ Storage**

Advanced PET-CT imaging was deployed during pure CO₂ injection and single-cycle SAG to study CO₂ flow behavior and dynamic saturation development in sandstone cores. The injections were performed at 90 bars and ambient temperature. During the PET-CT scan, a radioactive and water-soluble tracer, fluorodeoxyglucose (¹⁸F-FDG), was used to trace the aqueous solution in the core. The PET signal showed the position of the traced fluid in three dimensions as a function of time. As CO₂ was injected and propagated through a brine or surfactant-saturated core, the aqueous phase was displaced and the PET signal decreased. The absence of signal indicated the location of CO₂.

Figure 2.25a shows 3D images of dynamic water saturation development during CO₂ injection into brine saturated core at four timesteps and corresponding quantitative 1D water saturation profiles obtained from the PET signal. The white color represents areas without signal, and red represents areas with the strongest signal. Prior to CO₂ injection, 2 PVs of traced brine were injected into a brine-saturated core to implicitly observe CO₂ flow through the core. At PV =0, the PET signal was not equally distributed through the core due to capillary end effects and rock heterogeneity in the core (Cheng et al., 2015; Pini et al., 2013). A higher signal was observed near the outlet, whereas some pores near the inlet were not saturated with the tracer.

As CO₂ was injected, brine saturation in the core decreased, indicated by PET signal reduction. The traced water saturation profiles showed changes in water saturation during CO₂ injection. At PV = 0.24, the water saturation near the inlet decreased due to water displacement by CO₂. After approximately 0.50 PV of CO₂ injected, CO₂ broke through, and minor changes in water saturation were observed beyond that point due to the generation of continuous CO₂ flow paths. 3D images and 1D traced water saturation profiles at PV =0.48 and PV =0.84 were similar and indicated insignificant changes in water saturation after gas breakthrough. The average water saturation after 1 PV of CO₂ injected was approximately 0.70, with significant variations along the core length. Near the inlet and in the first 1/3 of the core, the traced water saturation

decreased from $S_w = 1$ to $S_w \sim 0.55$, whereas near the outlet, the water saturation remained high ($S_w \sim 0.90$).

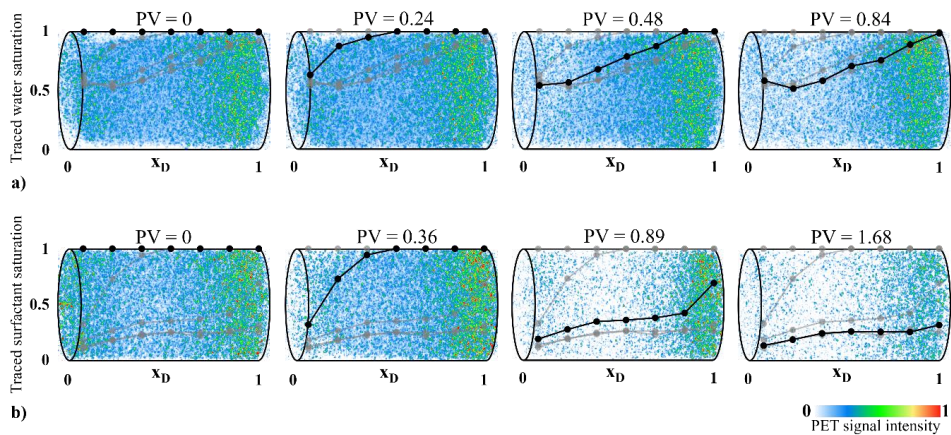


Figure 2.25. 3D PET images of dynamic water saturation development during CO_2 injection into (a) brine and (b) surfactant saturated sandstone core. Traced water/surfactant saturation versus dimensionless core length for each timestep overlay the images. White color indicates no PET signal whereas red color indicates a strong PET signal.

3D PET images of a single-cycle SAG, where CO_2 was injected into surfactant saturated core are shown in **Figure 2.25b**. At $\text{PV} = 0$, the core was fully saturated with the surfactant solution, although the water tracer was not uniformly distributed in the core, as described above. After 0.36 PV of CO_2 injected, the surfactant solution was displaced by CO_2 near the inlet of the core indicated by decreased PET signal intensity and reduced traced surfactant saturation from $S_w = 1$ to $S_w \sim 0.33$. During single-cycle SAG, the gas breakthrough was delayed compared to pure CO_2 injection and occurred after approximately 0.70 PV of CO_2 injected. Traced water saturation in the entire core decreased by 47% between 0 and 0.70 PV of CO_2 injected, which indicated improved sweep efficiency and decreased CO_2 mobility due to foam generation. After the breakthrough, the displacement rate decreased, indicated by minor changes in the PET signal intensity and saturation profiles for $\text{PV} = 0.89$ and $\text{PV} = 1.68$. After 1.68 PVs of CO_2 injected, most of the aqueous phase was displaced ($S_w \sim 0.24$). Near the inlet, the

water saturation was reduced to $S_w \sim 0.11$, whereas near the outlet, the water saturation remained higher ($S_w \sim 0.27$) due to capillary end effects (Cheng et al., 2015).

Comparison between CO_2 injection and single-cycle SAG showed a significant improvement in sweep efficiency due to foam generation during the single-cycle SAG. Increased water displacement was beneficial for CO_2 storage as more pores became available for CO_2 storage. Based on water saturation measurements, 160% more CO_2 was trapped in the core using foam compared to pure CO_2 injection. The increase in CO_2 storage is related to the capillary trapping of CO_2 within the pores during fine-textured foam generation, as described in the previous section.

Carbon Footprint Reduction

CO_2 foam EOR and simultaneous CO_2 storage may reduce the carbon footprint related to oil production if the amount of carbon stored exceeds the produced carbon from oil combustion and operations (Núñez-López et al., 2019). Carbon balance during different CO_2 EOR injections at the core-scale was evaluated based on the ratio between carbon atoms stored and carbon atoms produced (**Figure 2.26**). Mineral oil, n-Decane, was used to estimate carbon balance during CO_2 EOR and CO_2 storage. Carbon-negative oil recovery was achieved if more carbon was stored than produced and the ratio was above 1, whereas the oil recovery was considered carbon-positive if the ratio was less than 1.

The ratio between the amount of carbon stored and the amount of carbon produced was 0.97 ± 0.04 during single-cycle SAG (**Figure 2.26**, light red), indicating carbon-neutral oil production. Pure CO_2 injection (**Figure 2.26**, light blue) and implementing WAG (**Figure 2.26**, blue dashed) and multi-cycle SAG (**Figure 2.26**, red dashed) after drainage resulted in carbon-positive oil production, where more carbon was produced than stored. The ratio was significantly lower during WAG (0.36 ± 0.04) and multi-cycle SAG (0.55 ± 0.07) after drainage compared to the other injection methods. Therefore, the implementation of WAG and multi-cycle SAG after drainage was considered less favorable for achieving carbon footprint reduction. WAG and multi-cycle SAG performed after the initial waterflood (**Figure 2.26**, blue and red) resulted

in carbon-negative oil displacement due to generation of fine-textured foam, which enhanced capillary trapping of CO₂ and improved water and oil displacement.

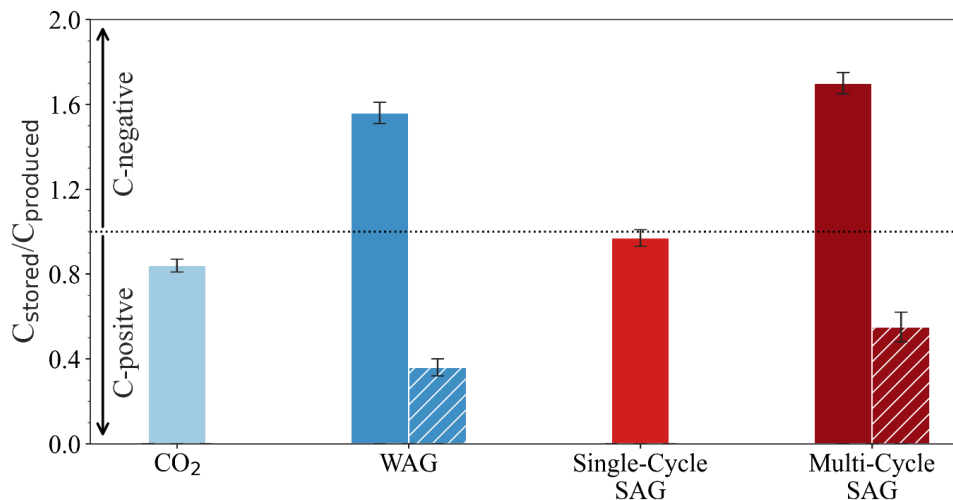


Figure 2.26. Carbon balance during CO₂ EOR and associated CO₂ storage processes. CO₂ injection, WAG and SAG were performed after waterflood (solid bars) and after drainage (dashed bars). Carbon-negative oil displacement was achieved if the ratio between stored and produced carbon was larger than one.

Mineral oil, n-Decane, containing 10 carbon atoms per molecule was used to evaluate carbon balance during the different CO₂ EOR injections. In the field, the composition of crude oil varies depending on the oil field and region. Crude oil is composed of hydrocarbon compounds with different carbon chain lengths. The average carbon number in crude oil is typically within the range of 20 to 40 carbon atoms per molecule. Oil composition impacts the estimated carbon footprint reduction during CO₂ EOR and CO₂ storage processes. Still, CO₂ EOR contributes to decarbonization of energy systems and provides an economic incentive for large-scale carbon capture and storage (CCS) (Núñez-López et al., 2019).

CO₂ Storage in Carbonate Reservoirs

Carbonate reservoirs are attractive CO₂ storage sites when combined with EOR operations, as majority of the remaining oil reserves reside in these rock types (Seyyedi et al., 2020). However, CO₂ injection into brine-saturated carbonates results in acidic conditions in the reservoir, which can lead to the dissolution of the rock matrix, which threatens formation integrity, injectivity, and storage security (Jones et al., 2022; Seyyedi et al., 2020). Carbon storage potential in Edwards limestone core was investigated during CO₂ EOR injections and compared to performance in Bentheimer sandstone (**Paper 5**). Two CO₂ EOR injections were performed a pure CO₂ injection into a core with residual oil saturation of approximately 30% and a single-cycle SAG injection at the same experimental conditions. **Figure 2.27** shows the estimated CO₂ storage capacity for the two rock types. Foam was not generated during pure CO₂ injection due to lack of foaming solution which resulted in low storage capacity in both cores. Improved sweep efficiency during single-cycle SAG increased storage capacity from $15 \pm 2\%$ to $67 \pm 2\%$ in limestone and from $12 \pm 3\%$ to $57 \pm 3\%$ in sandstone. Comparison between the two rocks showed higher storage capacity in limestone, likely because of the generation of more stable foam compared to sandstone which increased water displacement (**Figure 2.9**).

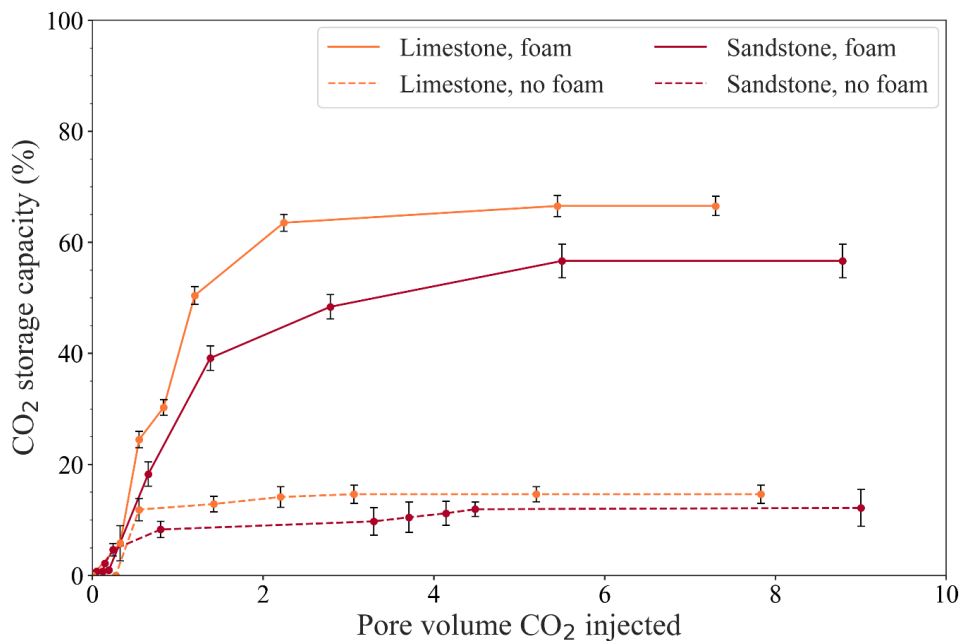


Figure 2.27. CO₂ storage capacity in limestone (orange) and sandstone (red) core plugs during CO₂ injection (dashed) and single-cycle SAG (solid). Higher CO₂ storage capacity was estimated in limestone compared to sandstone during SAG injections. Modified from Paper 5.

Dissolution of calcite was observed in the limestone core which could threaten formation integrity, injectivity, and storage security (Jones et al., 2022; Seyyedi et al., 2020) or benefit the storage capacity as additional pore space became available for storage (Noiriel & Daval, 2017). Calcite dissolution during CO₂ foam injections resulted in changes in the porosity and permeability of the rocks. Both increase and reduction of the absolute permeability were observed in different experiments. The increase in permeability was due to the dissolution and displacement of calcite, whereas the decrease in permeability occurred due to the re-depositing of calcite inside the core, which likely plugged the pore network and impeded fluid flow. **Figure 2.28** shows PET images of a coronal cross section along two limestone core plugs saturated with brine. A limestone core at the initial state without evidence of calcite dissolution is shown in **Figure 2.28a**. The water saturation was uniformly distributed in the core, indicated by the PET signal intensity. **Figure 2.28b** shows a similar limestone core saturated with brine after CO₂ foam injection and calcite dissolution.

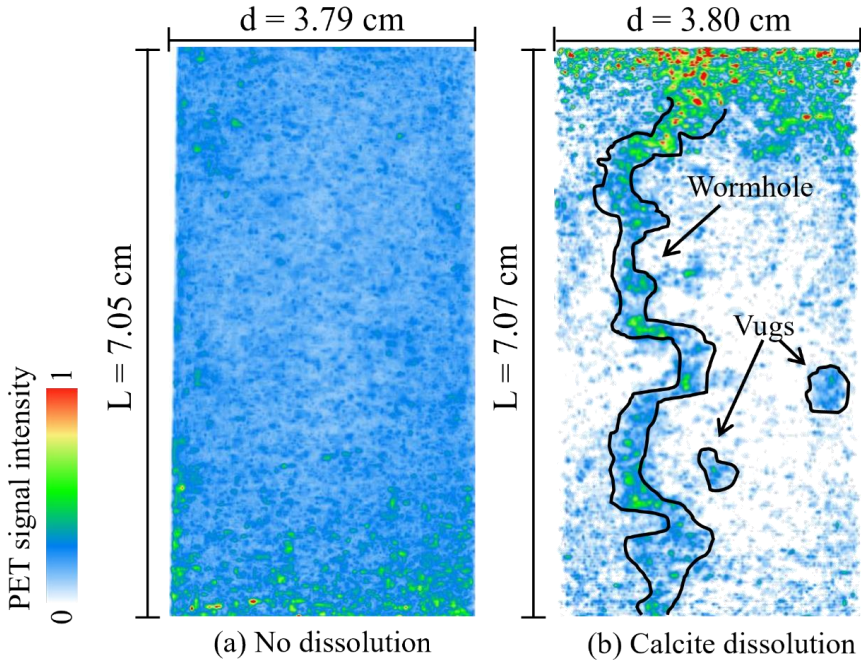


Figure 2.28. PET image of an Edward limestone core plug. (a) Brine-saturated core without dissolution and (b) brine-saturated core after foam injection and calcite dissolution. The formation of wormholes and vugs was observed. White color indicates no PET signal, whereas red color indicates a strong PET signal.

The formation of high permeability channels, known as wormholes, was observed. The wormholes stretched through the length of the core and created preferred flow paths. Additionally, calcite dissolution led to the formation of vugs, small cavities inside the rock, indicated by areas with high water saturation. The increased signal intensity near the inlet indicated compact dissolution, a cylindrical dissolution pattern near the injector typical for two-phase flow, which affects the mechanical integrity of the rock around the wellbore (Ott & Oedai, 2015). Determining the effect of foam on calcite dissolution in carbonate reservoirs is needed for effective and secure CO₂ EOR and CO₂ storage processes (Rossen et al., 2022).

3. Conclusions

Understanding multi-scale CO₂ foam behavior in porous media is important for the successful implementation of CO₂ EOR and CO₂ storage at the field-scale. Therefore, the objective of this work was to study foam dynamics, strength and stability at different reservoir conditions. A multi-scale approach spanning from pore- to field-scale was implemented to gain a more thorough understanding of foam systems and displacement mechanisms to improve predictive modeling of CO₂ foam. Experimental methods that deployed field-scale injection strategies were developed. In addition, advanced real-time *in-situ* CO₂ foam visualization at pore- and core-scale was utilized to gain insight into complex mechanisms and improve the knowledge of saturation development during CO₂ foam flow. The main conclusions are:

- Direct pore-scale visual observations revealed real-time insights on *in-situ* foam behavior at the core-scale, which improved the understanding of foam flow physics. Visual investigation of foam generation and destabilization revealed snap-off and leave-behind as the primary foam generation mechanisms, whereas foam coarsening, also known as Ostwald ripening, was the main contributor to foam destabilization. The improved understanding of foam flow dynamics can improve field-scale foam modeling.
- Multi-scale investigation of foam strength and stability provided a deeper understanding of the effect of various factors on CO₂ foam. Foam was highly affected by the reservoir permeability, foaming solution concentration, and the presence of oil.
 - In general, stronger and more stable foams were generated in high-permeability rocks.
 - The study demonstrated CO₂ mobility reduction at low surfactant concentrations (0.25 wt%) which is economically beneficial for field-scale implementation.
 - Foam generation was sensitive to oil saturation. High oil saturation of 0.70 hindered foam generation. At oil saturations below a critical value

of 0.30, foam and oil-in-water emulsions were generated and contributed to increasing the viscous forces and improving sweep efficiency.

- Pore- and core-scale studies showed that the addition of silica nanoparticles to non-ionic surfactant-based foam had an insignificant effect on foam strength and stability at the tested conditions.
- The efficiency of CO₂ foam for CO₂ EOR and CO₂ storage was investigated and compared to other CO₂ injection methods. Results revealed that foaming CO₂ improved sweep efficiency resulting in increased oil recovery and increased CO₂ storage capacity. Laboratory observations showed carbon neutral and carbon negative oil displacement using foam.
- Advanced *in-situ* PET-CT imaging visualized CO₂ flow and dynamic saturation development during foam injections providing an improved understanding of foam flow behavior in porous media. In addition, PET-CT imaging shed light on the changes in rock matrix due to calcite dissolution, which is important for effective and secure CO₂ EOR and CO₂ storage processes.
- Numerical simulations and foam model sensitivity studies were performed to match the observed bottom hole pressure data from a recently completed field pilot to study field-scale foam generation and propagation. Results revealed weaker foam generation during the pilot compared to laboratory observations. This provided important insights for the optimization of future field-scale applications.

4. Future Perspectives

This work demonstrated the benefits of using CO₂ foam for EOR and CO₂ storage and gained a deeper understanding of foam generation, strength, and stability at reservoir conditions. To optimize CO₂ foam EOR and storage for large-scale field application, continued research into fundamental foam mechanisms is necessary. The experimental multi-scale work presented in this thesis should be extended to improve the understanding of the size-dependent foam behavior. The suggestions for future work are:

- Emphasize the use of reservoir rocks with varying properties (e.g., permeability, mineralogy, wettability) and reservoir fluids including crude oils to gain better understanding of the effect of key reservoir properties on foam.
- Investigate different foaming solutions, including a variety of surfactants and nanoparticles, on foam generation and stability at realistic reservoir conditions for optimal CO₂ mobility control.
- Utilize PET-CT *in-situ* imaging during steady- and unsteady-state injections at different reservoir conditions to provide valuable knowledge of fluid flow, foam propagation and displacement mechanisms at core-scale and gain input data to improve numerical modeling.
- Apply *in-situ* visualization using magnetic resonance imaging (MRI) in combination with PET and/or CT to better understand the impact of oil on foam generation and stability and generation of oil-in-water emulsions.
- Develop and optimize mathematical methods to investigate multiphase foam flow on the pore- and core-scale with a detailed description of the foam generation and stability mechanisms.
- Improve predictive modeling of CO₂ foam using realistic laboratory data to advance the technology for CO₂ EOR and CO₂ storage at the field-scale.

Nomenclature

cP	Centipoise
f_g	Gas fraction
f_{mmob}	Foam model, maximum gas mobility reduction factor
ft/day	Foot per day
k	Absolute permeability of the porous media
k_{rg}^f	Gas relative permeability without foam
k_{rg}^{nf}	Gas relative permeability with foam
mD	Millidarcy
R_f	Recovery factor
S_o	Oil saturation
S_w	Water saturation
u_{gas}	Superficial velocity of gas
u_{liquid}	Superficial velocity of liquid
μ_{appv}	Apparent viscosity
∇p	Pressure gradient

Abbreviations

BHP	Bottom hole pressure
CCS	Carbon capture and storage
CCUS	Carbon capture, utilization and storage
CMC	critical micelle concentration
CT	Computed Tomography
EO	ethylate oxide
EOR	Enhanced oil recovery
EoS	Equation of state
FDG	fluorodeoxyglucose
FM	Mobility reduction factor
LE	Local-equilibrium
LOC	Lab-on-a-chip
MRI	Magnetic Resonance Imaging
NP	Nanoparticles
OOIP	Original oil in place
OWIP	Original water in place
PB	Population-balance
PET	Positron Emission Tomography
PR	Peng-Robinson
PV	Pore volume
PVT	Pressure-volume-temperature
SAG	Surfactant-alternating gas
SF	Surfactant
WAG	Water-alternating gas
Wt%	Weight percent

References

- Adebayo, A. R. (2021). Foam Flow in Different Pore Systems—Part 1: The Roles of Pore Attributes and Their Variation on Trapping and Apparent Viscosity of Foam. *SPE Journal*, 26(06), 3908-3925. doi:10.2118/206719-pa
- Akin, S., & Kovsky, A. R. (2003). Computed tomography in petroleum engineering research. In *Applications of X-ray Computed Tomography in the Geosciences* (Vol. 215, pp. 0). doi:10.1144/GSL.SP.2003.215.01.03
- Alcorn, Z. P., Fernø, M. A., & Graue, A. (2020a). *Upscaling CO2 Foam for EOR as CCUS from On-To Offshore*. Paper presented at the Offshore Technology Conference.
- Alcorn, Z. P., Fredriksen, S. B., Sharma, M., Rognmo, A. U., Føyen, T. L., Fernø, M. A., & Graue, A. (2019). An Integrated Carbon-Dioxide-Foam Enhanced-Oil-Recovery Pilot Program With Combined Carbon Capture, Utilization, and Storage in an Onshore Texas Heterogeneous Carbonate Field. *SPE Reservoir Evaluation & Engineering*, 22(04), 1449-1466. doi:10.2118/190204-pa
- Alcorn, Z. P., Føyen, T., Zhang, L., Karakas, M., Biswal, S. L., Hirasaki, G., & Graue, A. (2020b). *CO2 Foam Field Pilot Design and Initial Results*. Paper presented at the SPE Improved Oil Recovery Conference, Virtual. 31 August. doi:10.2118/200450-ms
- Alcorn, Z. P., Graue, A., & Karakas, M. (2022). *CO2 Foam Pilot in a Heterogeneous Carbonate Reservoir: Analysis and Results*. 2022. doi:10.2118/209359-ms
- Alvarez, J. M., Rivas, H. J., & Rossen, W. R. (2001). Unified Model for Steady-State Foam Behavior at High and Low Foam Qualities. *SPE Journal*, 6(03), 325-333. doi:10.2118/74141-pa
- AlYousif, Z., Kokal, S., Alabdulwahab, A., & Gizzatov, A. (2018). *CO2-Foam Rheology: Effect of Surfactant Concentration, Shear Rate and Injection Quality*. Paper presented at the SPE Kingdom of Saudi Arabia Annual Technical Symposium and Exhibition. doi:10.2118/192361-MS
- Bachu, S., Freund, P., Gupta, M., Simbeck, D., & Thambimuthu, K. (2005). Annex I: properties of CO₂ and carbon-based fuels. *IPCC special report on carbon dioxide capture and storage*. Cambridge University Press, New York.
- Bailey, D. L., Maisey, M. N., Townsend, D. W., & Valk, P. E. (2005). *Positron emission tomography* (Vol. 2): Springer.
- Behera, M. R., Varade, S. R., Ghosh, P., Paul, P., & Negi, A. S. (2014). Foaming in Micellar Solutions: Effects of Surfactant, Salt, and Oil Concentrations. *Industrial & Engineering Chemistry Research*, 53(48), 18497-18507. doi:10.1021/ie503591v
- Benali, B., Føyen, T. L., Alcorn, Z. P., Haugen, M., Gauteplass, J., Kovsky, A. R., & Fernø, M. A. (2022). Pore-scale bubble population dynamics of CO₂-foam at

-
- reservoir pressure. *International Journal of Greenhouse Gas Control*, 114, 103607. doi:10.1016/j.ijggc.2022.103607
- Bennetzen, M. V., & Mogensen, K. (2014). *Novel Applications of Nanoparticles for Future Enhanced Oil Recovery*. Paper presented at the International Petroleum Technology Conference, Kuala Lumpur, Malaysia. 10-12 December. doi:10.2523/IPTC-17857-MS
- Bharti, B. (2014). Introduction, Interaction of Nanoparticles with Nonionic Surfactants. In B. Bharti (Ed.), *Adsorption, Aggregation and Structure Formation in Systems of Charged Particles: From Colloidal to Supracolloidal Assembly* (pp. 3-14). Cham: Springer International Publishing.
- Brattekkås, B., Fernø, M. A., Haugen, M., Føyen, T., Steinsbø, M., Graue, A., . . . Espedal, H. (2021). *Ofrats and rocks: Using pre-clinical PET imaging facilities in core analysis*. Paper presented at the Proceedings of the Annual symposium of the Society of Core Analysts, Virtual.
- Brattekkås, B., & Haugen, M. (2020). Explicit tracking of CO₂-flow at the core scale using micro-Positron Emission Tomography (μ PET). *Journal of Natural Gas Science and Engineering*, 77, 103268. doi:10.1016/j.jngse.2020.103268
- Chang, S.-H., & Grigg, R. B. (1999). Effects of Foam Quality and Flow Rate on CO₂-Foam Behavior at Reservoir Temperature and Pressure. *SPE Reservoir Evaluation & Engineering*, 2(03), 248-254. doi:10.2118/56856-pa
- Chen, M., Yortsos, Y. C., & Rossen, W. R. (2004). *A Pore-Network Study of the Mechanisms of Foam Generation*. Paper presented at the SPE Annual Technical Conference and Exhibition. 26-29 September. doi:10.2118/90939-ms
- Cheng, Y.-c., Di, Q.-f., Gu, C.-y., Ye, F., Hua, S., & Yang, P.-q. (2015). Visualization study on fluid distribution and end effects in core flow experiments with low-field mri method. *Journal of Hydrodynamics, Ser. B*, 27(2), 187-194. doi:10.1016/S1001-6058(15)60471-1
- Chou, S. I., Vasicek, S. L., Pizio, D. L., Jasek, D. E., & Goodgame, J. A. (1992). *CO₂ Foam Field Trial at North Ward-Estes*. Paper presented at the 67th Annual Technical Conference and Exhibition of the Society of Petroleum Engineers, Washington, DC. 4-7 October. doi:10.2118/24643-ms
- Datta, S. S., Battiato, I., Fernø, M. A., Juanes, R., Parsa, S., Prigiobbe, V., . . . Sinton, D. (2023). Lab on a chip for a low-carbon future. *Lab on a Chip*, 23(5), 1358-1375. doi:10.1039/D2LC00020B
- Ding, M., Yuan, F., Wang, Y., Xia, X., Chen, W., & Liu, D. (2017). Oil recovery from a CO₂ injection in heterogeneous reservoirs: The influence of permeability heterogeneity, CO₂-oil miscibility and injection pattern. *Journal of Natural Gas Science and Engineering*, 44, 140-149. doi:10.1016/j.jngse.2017.04.015
- Eiken, O., Ringrose, P., Hermanrud, C., Nazarian, B., Torp, T. A., & Høier, L. (2011). Lessons learned from 14 years of CCS operations: Sleipner, In Salah and Snøhvit. *Energy Procedia*, 4, 5541-5548. doi:10.1016/j.egypro.2011.02.541

-
- Enick, R. M., Olsen, D. K., Ammer, J., & Schuller, W. (2012). *Mobility and Conformance Control for Carbon Dioxide Enhanced Oil Recovery (CO₂-EOR) via Thickeners, Foams, and Gels – A Detailed Literature Review of 40 Years of Research*. Paper presented at the SPE Improved Oil Recovery Symposium, Tulsa, Oklahoma. 14-18 April. doi:10.2118/154122-MS
- Falls, A. H., Hirasaki, G. J., Patzek, T. W., Gauglitz, D. A., Miller, D. D., & Ratulowski, T. (1988). Development of a Mechanistic Foam Simulator: The Population Balance and Generation by Snap-Off. *SPE Reservoir Engineering*, 3(03), 884-892. doi:10.2118/14961-pa
- Falls, A. H., Musters, J. J., & Ratulowski, J. (1989). The Apparent Viscosity of Foams in Homogeneous Bead Packs. *SPE Reservoir Engineering*, 4(02), 155-164. doi:10.2118/16048-PA
- Farajzadeh, R., Andrianov, A., Krastev, R., Hirasaki, G., & Rossen, W. R. (2012). Foam-Oil Interaction in Porous Media: Implications for Foam Assisted Enhanced Oil Recovery. *Advances in Colloid and Interface Science*, 183-184, 1-13. doi:10.1016/j.cis.2012.07.002.
- Farajzadeh, R., Lotfollahi, M., Eftekhari, A. A., Rossen, W. R., & Hirasaki, G. J. H. (2015). Effect of Permeability on Implicit-Texture Foam Model Parameters and the Limiting Capillary Pressure. *Energy & Fuels*, 29(5), 3011-3018. doi:10.1021/acs.energyfuels.5b00248
- Fernø, M. A., Hauge, L. P., Uno Rognmo, A., Gautepluss, J., & Graue, A. (2015). Flow visualization of CO₂ in tight shale formations at reservoir conditions. *Geophysical Research Letters*, 42(18), 7414-7419. doi:10.1002/2015GL065100
- Friedmann, F., & Jensen, J. A. (1986). *Some Parameters Influencing the Formation and Propagation of Foams in Porous Media*. Paper presented at the SPE California Regional Meeting, Oakland, California. 2-4 April. doi:10.2118/15087-MS
- Gauglitz, P. A., Friedmann, F., Kam, S. I., & Rossen, W. R. (2002). *Foam Generation in Porous Media*. Paper presented at the SPE/DOE Improved Oil Recovery Symposium, Tulsa, Oklahoma. 13-17 April. doi:10.2118/75177-MS
- Gizzatov, A., Pierobon, S., AlYousef, Z., Jian, G., Fan, X., Abedini, A., & Abdel-Fattah, A. I. (2021). High-temperature high-pressure microfluidic system for rapid screening of supercritical CO₂ foaming agents. *Scientific Reports*, 11(1), 3360. doi:10.1038/s41598-021-82839-4
- Hanssen, J. E., Holt, T., & Surguchev, L. M. (1994). *Foam Processes: An Assessment of Their Potential in North Sea Reservoirs Based on a Critical Evaluation of Current Field Experience*. Paper presented at the SPE/DOE Improved Oil Recovery Symposium, Tulsa, Oklahoma. 17-20 April. doi:10.2118/27768-ms
- Hepburn, C., Adlen, E., Beddington, J., Carter, E. A., Fuss, S., Mac Dowell, N., . . . Williams, C. K. (2019). The technological and economic prospects for CO₂ utilization and removal. *Nature*, 575(7781), 87-97. doi:10.1038/s41586-019-1681-6

-
- Hirasaki, G. J., & Lawson, J. B. (1985). Mechanisms of Foam Flow in Porous Media: Apparent Viscosity in Smooth Capillaries. *Society of Petroleum Engineers Journal*, 25(02), 176-190. doi:10.2118/12129-PA
- Hirono, T., Takahashi, M., & Nakashima, S. (2003). In situ visualization of fluid flow image within deformed rock by X-ray CT. *Engineering Geology*, 70(1), 37-46. doi:10.1016/S0013-7952(03)00074-7
- Hoefner, M. L., & Evans, E. M. (1995). CO₂ Foam: Results From Four Developmental Field Trials. *SPE Reservoir Engineering*, 10(04), 273-281. doi:10.2118/27787-pa
- Huh, D. G., & Handy, L. L. (1989). Comparison of Steady- and Unsteady-State Flow of Gas and Foaming Solution in Porous Media. *SPE Reservoir Engineering*, 4(01), 77-84. doi:10.2118/15078-pa
- IEA. (2020). *The Oil and Gas Industry in Energy Transitions*, IEA. Paris <https://www.iea.org/reports/the-oil-and-gas-industry-in-energy-transitions>, License: CC BY 4.0
- IEA. (2022). *World Energy Outlook 2022*, IEA. Paris <https://www.iea.org/reports/world-energy-outlook-2022>, License: CC BY 4.0 (report); CC BY NC SA 4.0 (Annex A)
- IPCC. (2018). *Global Warming of 1.5° C: An IPCC Special Report on the Impacts of Global Warming of 1.5° C Above Pre-industrial Levels and Related Global Greenhouse Gas Emission Pathways, in the Context of Strengthening the Global Response to the Threat of Climate Change, Sustainable Development, and Efforts to Eradicate Poverty*: Intergovernmental Panel on Climate Change.
- Jian, G., Gizatov, A., Kawelah, M., AlYousef, Z., & Abdel-Fattah, A. I. (2021). Simply built microfluidics for fast screening of CO₂ foam surfactants and foam model parameters estimation. *Applied Energy*, 292, 116815. doi:10.1016/j.apenergy.2021.116815
- Jian, G., Puerto, M. C., Wehowsky, A., Dong, P., Johnston, K. P., Hirasaki, G. J., & Biswal, S. L. (2016). Static Adsorption of an Ethoxylated Nonionic Surfactant on Carbonate Minerals. *Langmuir*, 32(40), 10244-10252. doi:10.1021/acs.langmuir.6b01975
- Johannesen, E., Riskedal, H., Tipura, L., Howard, J., & Graue, A. (2007). *Wettability characterization by NMR T₂ measurements in Edwards limestone rock*. Paper presented at the International Symposium of the Society of Core Analysts.
- Jones, S. A., Kahrobaei, S., Van Wageningen, N., & Farajzadeh, R. (2022). CO₂ Foam Behavior in Carbonate Rock: Effect of Surfactant Type and Concentration. *Industrial & Engineering Chemistry Research*, 61(32), 11977-11987. doi:10.1021/acs.iecr.2c01186
- Jones, S. A., Laskaris, G., Vincent-Bonnieu, S., Farajzadeh, R., & Rossen, W. R. (2016). *Surfactant Effect On Foam: From Core Flood Experiments To Implicit-Texture Foam-Model Parameters*. Paper presented at the SPE Improved Oil Recovery Conference, Tulsa, Oklahoma. 11-13 April. doi:10.2118/179637-MS

-
- Kahrobaei, S., Vincent-Bonnieu, S., & Farajzadeh, R. (2017). Experimental Study of Hysteresis behavior of Foam Generation in Porous Media. *Scientific Reports*, 7(1), 8986. doi:10.1038/s41598-017-09589-0
- Khan, S. A., Schnepfer, C. A., & Armstrong, R. C. (1988). Foam Rheology: III. Measurement of Shear Flow Properties. *Journal of Rheology*, 32(1), 69-92. doi:10.1122/1.549964
- Khatib, Z. I., Hirasaki, G. J., & Falls, A. H. (1988). Effects of Capillary Pressure on Coalescence and Phase Mobilities in Foams Flowing Through Porous Media. *SPE Reservoir Engineering*, 3(03), 919-926. doi:10.2118/15442-pa
- Kim, M., Sell, A., & Sinton, D. (2013). Aquifer-on-a-Chip: understanding pore-scale salt precipitation dynamics during CO₂ sequestration. *Lab on a Chip*, 13(13), 2508-2518. doi:10.1039/C3LC00031A
- Kornev, K. G., Neimark, A. V., & Rozhkov, A. N. (1999). Foam in porous media: thermodynamic and hydrodynamic peculiarities. *Advances in Colloid and Interface Science*, 82(1), 127-187. doi:10.1016/S0001-8686(99)00013-5
- Kovscek, A. R., & Radke, C. J. (1994). Fundamentals of Foam Transport in Porous Media. In *Foams: Fundamentals and Applications in the Petroleum Industry* (Vol. 242, pp. 115-163): American Chemical Society.
- Lee, S., & Kam, S. I. (2013). Chapter 2 - Enhanced Oil Recovery by Using CO₂ Foams: Fundamentals and Field Applications. In J. J. Sheng (Ed.), *Enhanced Oil Recovery Field Case Studies* (pp. 23-61). Boston: Gulf Professional Publishing.
- Ma, H., Luo, M., & Dai, L. L. (2008). Influences of surfactant and nanoparticle assembly on effective interfacial tensions. *Physical Chemistry Chemical Physics*, 10(16), 2207-2213. doi:10.1039/B718427C
- Ma, K., Lopez-Salinas, J. L., Puerto, M. C., Miller, C. A., Biswal, S. L., & Hirasaki, G. J. (2013). Estimation of Parameters for the Simulation of Foam Flow through Porous Media. Part 1: The Dry-Out Effect. *Energy & Fuels*, 27(5), 2363-2375. doi:10.1021/ef302036s
- Maini, B. B., & Ma, V. (1986). Laboratory Evaluation Of Foaming Agents For High-Temperature Applications — I. Measurements Of Foam Stability At Elevated Temperatures And Pressures. *Journal of Canadian Petroleum Technology*, 25(06), 6. doi:10.2118/86-06-05
- Mannhardt, K., Novosad, J. J., & Schramm, L. L. (1998). *Foam/Oil Interactions at Reservoir Conditions*. Paper presented at the SPE/DOE Improved Oil Recovery Symposium, Tulsa, Oklahoma. 19-22 April. doi:10.2118/39681-ms
- Massarweh, O., & Abushaikha, A. S. (2021). A review of recent developments in CO₂ mobility control in enhanced oil recovery. *Petroleum*. doi:10.1016/j.petlm.2021.05.002
- Mo, D., Yu, J., Liu, N., & Lee, R. L. (2012). *Study of the Effect of Different Factors on Nanoparticle-Stabilized CO₂ Foam for Mobility Control*. Paper presented at the SPE Annual Technical Conference and Exhibition, San Antonio, Texas, USA. 8-10 October. doi:10.2118/159282-MS

-
- Müller, T., & Lake, L. W. (1991). Theoretical Study of Water Blocking in Miscible Flooding. *SPE Reservoir Engineering*, 6(04), 445-451. doi:10.2118/20206-pa
- Noiriel, C., & Daval, D. (2017). Pore-Scale Geochemical Reactivity Associated with CO₂ Storage: New Frontiers at the Fluid–Solid Interface. *Accounts of Chemical Research*, 50(4), 759-768. doi:10.1021/acs.accounts.7b00019
- Núñez-López, V., Gil-Egui, R., & Hosseini, S. A. (2019). Environmental and Operational Performance of CO₂-EOR as a CCUS Technology: A Cranfield Example with Dynamic LCA Considerations. *Energies*, 12(3). doi:10.3390/en12030448
- Ott, H., & Oedai, S. (2015). Wormhole formation and compact dissolution in single- and two-phase CO₂-brine injections. *Geophysical Research Letters*, 42(7), 2270-2276. doi:10.1002/2015GL063582
- Pal, N., Zhang, X., Ali, M., Mandal, A., & Hoteit, H. (2022). Carbon dioxide thickening: A review of technological aspects, advances and challenges for oilfield application. *Fuel*, 315, 122947. doi:10.1016/j.fuel.2021.122947
- Peksa, A. E., Wolf, K.-H. A. A., & Zitha, P. L. J. (2015). Bentheimer sandstone revisited for experimental purposes. *Marine and Petroleum Geology*, 67, 701-719. doi:10.1016/j.marpetgeo.2015.06.001
- Pichot, R., Spyropoulos, F., & Norton, I. T. (2012). Competitive adsorption of surfactants and hydrophilic silica particles at the oil–water interface: Interfacial tension and contact angle studies. *Journal of Colloid and Interface Science*, 377(1), 396-405. doi:10.1016/j.jcis.2012.01.065
- Pini, R., Krevor, S., Krause, M., & Benson, S. (2013). Capillary Heterogeneity in Sandstone Rocks During CO₂/Water Core-flooding Experiments. *Energy Procedia*, 37, 5473-5479. doi:10.1016/j.egypro.2013.06.467
- Pini, R., Vandehey, N. T., Druhan, J., O’Neil, J. P., & Benson, S. M. (2016). Quantifying solute spreading and mixing in reservoir rocks using 3-D PET imaging. *Journal of Fluid Mechanics*, 796, 558-587. doi:10.1017/jfm.2016.262
- Prud’homme, R. K., & Khan, S. A. (1996). *Foams : theory, measurements, and applications* (Vol. vol. 57). New York: Marcel Dekker.
- Ransohoff, T. C., & Radke, C. J. (1988). Mechanisms of Foam Generation in Glass-Bead Packs. *SPE Reservoir Engineering*, 3(02), 573-585. doi:10.2118/15441-PA
- Ritchie, H., Roser, M., & Rosado, P. (2022). Energy. Retrieved from <https://ourworldindata.org/energy>
- Rognmo, A. U., Fredriksen, S. B., Alcorn, Z. P., Sharma, M., Føyen, T., Eide, Ø., . . . Fernø, M. (2019). Pore-to-Core EOR Upscaling for CO₂ Foam for CCUS. *SPE Journal*, 24(06), 2793-2803. doi:10.2118/190869-pa
- Ross, S., & McBain, J. W. (1944). Inhibition of Foaming in Solvents Containing Known Foamers. *Industrial & Engineering Chemistry*, 36(6), 570-573. doi:10.1021/ie50414a019

-
- Rossen, W. R. (1996). Foams in enhanced oil recovery. *Foams: theory, measurements and applications*, 57, 413-464.
- Rossen, W. R., Farajzadeh, R., Hirasaki, G. J., & Amirmoshiri, M. (2022). *Potential and challenges of foam-assisted CO₂ sequestration*. Paper presented at the SPE Improved Oil Recovery Conference.
- Schramm, L. L., & Novosad, J. J. (1992). The destabilization of foams for improved oil recovery by crude oils: Effect of the nature of the oil. *Journal of Petroleum Science and Engineering*, 7(1), 77-90. doi:10.1016/0920-4105(92)90010-X
- Schramm, L. L., & Wassmuth, F. (1994). Foams: Basic Principles. In *Foams: Fundamentals and Applications in the Petroleum Industry* (Vol. 242, pp. 3-45): American Chemical Society.
- Seyyedi, M., Mahmud, H. K. B., Verrall, M., Giwelli, A., Esteban, L., Ghasemiziarani, M., & Clennell, B. (2020). Pore Structure Changes Occur During CO₂ Injection into Carbonate Reservoirs. *Scientific Reports*, 10(1), 3624. doi:10.1038/s41598-020-60247-4
- Shan, D., & Rossen, W. R. (2004). Optimal Injection Strategies for Foam IOR. *SPE Journal*, 9(02), 132-150. doi:10.2118/88811-pa
- Sharma, M. (2019). *CO₂ Mobility Control with Foam for Enhanced Oil Recovery and Associated Storage Multi-scale Approach for Field Application*. (PhD). University of Stavanger, Retrieved from <https://www.uis.no/sites/default/files/inline-images/uaGYu4WynJ81f3RT3vGx6TMOOPPxoRhAk68MFqeDpQhdJnx3Ns.pdf>
- Sharma, M., Alcorn, Z., Fredriksen, S., Fernø, M., & Graue, A. (2017). *Numerical modelling study for designing CO₂-foam field pilot*. Paper presented at the IOR 2017-19th European Symposium on Improved Oil Recovery.
- Shelton, J. L., & Schneider, F. N. (1975). The Effects of Water Injection on Miscible Flooding Methods Using Hydrocarbons and Carbon Dioxide. *Society of Petroleum Engineers Journal*, 15(03), 217-226. doi:10.2118/4580-pa
- Sheng, (2013). Chapter 11 - Foams and Their Applications in Enhancing Oil Recovery. In J. J. Sheng (Ed.), *Enhanced Oil Recovery Field Case Studies* (pp. 251-280). Boston: Gulf Professional Publishing.
- Simjoo, M., Dong, Y., Andrianov, A., Talanana, M., & Zitha, P. L. (2012). *A CT Scan Study of Immiscible Foam Flow in Porous Media for EOR*. Paper presented at the SPE EOR Conference at Oil and Gas West Asia. doi:10.2118/155633-MS
- Skauge, T., Spildo, K., & Skauge, A. (2010). *Nano-sized Particles For EOR*. Paper presented at the SPE Improved Oil Recovery Symposium, Tulsa, Oklahoma, USA. 2010/1/1/. doi:10.2118/129933-MS
- Song, Y.-C., Ning-Jun, Z., Yu, L., Jia-Fei, Z., Wei-Guo, L., Yi, Z., . . . Lan-Lan, J. (2011). Magnetic resonance imaging study on the miscibility of a CO₂/n-decane system. *Chinese Physics Letters*, 28(9), 096401.


-
- Taber, J. J., Martin, F. D., & Seright, R. S. (1997). EOR Screening Criteria Revisited - Part 1: Introduction to Screening Criteria and Enhanced Recovery Field Projects. *SPE Reservoir Engineering*, 12(03), 189-198. doi:10.2118/35385-PA
- Talebian, S. H., Masoudi, R., Tan, I. M., & Zitha, P. L. J. (2014). Foam assisted CO₂-EOR: A review of concept, challenges, and future prospects. *Journal of Petroleum Science and Engineering*, 120, 202-215. doi:10.1016/j.petrol.2014.05.013
- Talmage, S. S. (2020). *Environmental and human safety of major surfactants: alcohol ethoxylates and alkylphenol ethoxylates*: CRC Press.
- Wang, J., Nguyen, A. V., & Farrokhpay, S. (2016). A critical review of the growth, drainage and collapse of foams. *Advances in Colloid and Interface Science*, 228, 55-70. doi:10.1016/j.cis.2015.11.009
- Xu, K., Bonnecaze, R., & Balhoff, M. (2017). Egalitarianism among Bubbles in Porous Media: An Ostwald Ripening Derived Anticoarsening Phenomenon. *Physical Review Letters*, 119(26). doi:10.1103/physrevlett.119.264502
- Yekeen, N., Manan, M. A., Idris, A. K., Padmanabhan, E., Junin, R., Samin, A. M., . . . Oguamah, I. (2018). A comprehensive review of experimental studies of nanoparticles-stabilized foam for enhanced oil recovery. *Journal of Petroleum Science and Engineering*, 164, 43-74. doi:10.1016/j.petrol.2018.01.035
- Yekeen, N., Manan, M. A., Idris, A. K., & Samin, A. M. (2017). Influence of surfactant and electrolyte concentrations on surfactant Adsorption and foaming characteristics. *Journal of Petroleum Science and Engineering*, 149, 612-622. doi:https://doi.org/10.1016/j.petrol.2016.11.018
- Yu, W., & Kanj, M. Y. (2022). Review of foam stability in porous media: The effect of coarsening. *Journal of Petroleum Science and Engineering*, 208, 109698. doi:10.1016/j.petrol.2021.109698
- Zahasky, C., Kurotori, T., Pini, R., & Benson, S. M. (2019). Positron emission tomography in water resources and subsurface energy resources engineering research. *Advances in Water Resources*, 127, 39-52. doi:10.1016/j.advwatres.2019.03.003
- Zhang, D., & Song, J. (2014). Mechanisms for Geological Carbon Sequestration. *Procedia IUTAM*, 10, 319-327. doi:10.1016/j.piutam.2014.01.027

Scientific Papers

Paper 1

Article

Pore- and Core-Scale Insights of Nanoparticle-Stabilized Foam for CO₂-Enhanced Oil Recovery

Zachary Paul Alcorn ^{1,*}, Tore Føyen ^{1,2}, Jarand Gauteplass ¹ , Benyamine Benali ¹, Aleksandra Soyke ¹ and Martin Fernø ¹

¹ Department of Physics and Technology, University of Bergen, 5007 Bergen, Norway; tore.foyen@uib.no (T.F.); Jarand.Gauteplass@uib.no (J.G.); Benyamine.benali@uib.no (B.B.); aleksandra.soyke@uib.no (A.S.); Martin.Fernø@uib.no (M.F.)

² SINTEF Industry, 7034 Trondheim, Norway

* Correspondence: zachary.alcorn@uib.no

Received: 4 September 2020; Accepted: 17 September 2020; Published: 25 September 2020



Abstract: Nanoparticles have gained attention for increasing the stability of surfactant-based foams during CO₂ foam-enhanced oil recovery (EOR) and CO₂ storage. However, the behavior and displacement mechanisms of hybrid nanoparticle–surfactant foam formulations at reservoir conditions are not well understood. This work presents a pore- to core-scale characterization of hybrid nanoparticle–surfactant foaming solutions for CO₂ EOR and the associated CO₂ storage. The primary objective was to identify the dominant foam generation mechanisms and determine the role of nanoparticles for stabilizing CO₂ foam and reducing CO₂ mobility. In addition, we shed light on the influence of oil on foam generation and stability. We present pore- and core-scale experimental results, in the absence and presence of oil, comparing the hybrid foaming solution to foam stabilized by only surfactants or nanoparticles. Snap-off was identified as the primary foam generation mechanism in high-pressure micromodels with secondary foam generation by leave behind. During continuous CO₂ injection, gas channels developed through the foam and the texture coarsened. In the absence of oil, including nanoparticles in the surfactant-laden foaming solutions did not result in a more stable foam or clearly affect the apparent viscosity of the foam. Foaming solutions containing only nanoparticles generated little to no foam, highlighting the dominance of surfactant as the main foam generator. In addition, foam generation and strength were not sensitive to nanoparticle concentration when used together with the selected surfactant. In experiments with oil at miscible conditions, foam was readily generated using all the tested foaming solutions. Core-scale foam-apparent viscosities with oil were nearly three times as high as experiments without oil present due to the development of stable oil/water emulsions and their combined effect with foam for reducing CO₂ mobility

Keywords: nanoparticles; foam; CO₂ EOR; CO₂ mobility control

1. Introduction

An energy transition to a net-zero society is a global challenge in need of affordable, low-risk technologies. Carbon capture, utilization and storage (CCUS) is a crucial technology for substantial emission cuts for many energy-intensive industries to achieve the ambitious climate goals of the Paris Agreement [1]. CCUS involves capturing CO₂ from industrial sources and injecting it into subsurface reservoirs for simultaneous storage and energy production, via CO₂-enhanced oil recovery (EOR). Permanent CO₂ storage coupled with CO₂ EOR can provide affordable and reliable energy for our developing world while reducing the life-cycle carbon emissions of fossil fuels.

CO₂ EOR has been developed and widely implemented over the past 50 years. CO₂ is an excellent solvent in EOR processes because it is miscible with most crude oils at reservoir conditions. Above miscibility conditions, CO₂ swells the oil and reduces its viscosity resulting in increased recovery. Laboratory corefloods have reported high microscopic displacement efficiency and oil recoveries of nearly 100% [2]. However, field-scale operations often report lower than expected recoveries due to poor sweep efficiency and high CO₂ mobility [3,4]. These issues stem from reservoir heterogeneity and the low viscosity and density of CO₂ compared to reservoir fluids.

CO₂ foam can mitigate the impacts of high CO₂ mobility and reservoir heterogeneity by effectively increasing CO₂ viscosity, reducing its relative permeability and diverting CO₂ flow from high permeability zones [5]. CO₂ foam is generated in porous media by injecting foaming solution with CO₂, either simultaneously or in alternating slugs. The foam is a dispersion of CO₂ in liquid where stable liquid films, called lamellae, block some of the pathways for CO₂ flow [6]. Lamellae are commonly stabilized by surfactants. However, surfactant-stabilized foams can break down in the reservoir due to surfactant adsorption, the presence of oil, and at elevated temperatures and salinities. Therefore, their ability to reduce CO₂ mobility can be limited. The addition of silica nanoparticles to the surfactant-stabilized CO₂ foam has been shown to increase the strength and stability of the foam system and provide increased oil recovery [7,8].

Spherical silica nanoparticles are the most commonly used for EOR applications [9]. They are particles with a size up to 100 nm with intrinsic properties different from those found in the bulk of the material due to their high surface-to-volume ratio. Stable emulsions are generated using nanoparticles because a rigid monolayer is formed on the droplet surface and the particles are irreversibly attached to the interface. These emulsions may withstand high-temperature reservoir conditions without agglomeration and the nanoparticles may be further surface-treated to improve stability in harsh conditions. In addition, the small size of the particles, two orders of magnitude smaller than colloidal particles, make them suitable for flow through small pore throats in rock [10,11].

Whether stabilized by surfactants, nanoparticles, or a combination of both, bulk foams are typically composed of bubbles smaller than the containers they are within whereas foam in porous media is composed of bubbles about the same size or larger as the pore space [12]. For foam to generate, lamella creation must exceed lamella destruction. Capillary forces dominate lamella creation by three main mechanisms: leave behind, snap-off and lamella division [5,13].

An issue with foam for EOR applications is the impact of oil on foam (lamellae) stability. Many studies report that oil hinders foam generation and can destabilize already generated foam [14–16]. However, these findings are mostly based upon bulk tests at immiscible conditions with surfactant-stabilized foam, which may not necessarily represent foam in porous media and at miscible conditions for CO₂ and oil. In any case, foam behavior in the presence of oil involves several interactions between the foam, oil, and rock, which may be either detrimental or beneficial to the foam process [17,18]. These interactions include emulsification–imbibition, pseudo emulsions, and entering and spreading [19,20].

In the absence of oil, foam coalescence can reduce the number of bubbles by two mechanisms: texture (bubble size) coarsening by diffusion, often referred to as Ostwald ripening, or capillary suction drainage [21]. Diffusion occurs by the transport of gas from smaller bubbles to larger bubbles, with lower internal pressure, which results in fewer bubbles [22,23]. Capillary suction drainage occurs when the water saturation approaches a saturation value where the lamellae are no longer stable, as the capillary pressure exceeds the maximum disjoining pressure of the foam film and drains the lamellae [24,25].

The majority of earlier work has focused on foam generation and the coalescence of surfactant-stabilized CO₂ foams in the absence and presence of oil at immiscible conditions. However, much less is known about the role of nanoparticles in the absence and presence of oil at miscible conditions. Thus, this study aimed to thoroughly characterize the dominant foam generation mechanisms and determine the role of nanoparticles for stabilizing CO₂ foam and reducing CO₂

mobility. In addition, we shed light on the influence of oil on foam generation and stability. We present a pore- to core-scale characterization of hybrid nanoparticle–surfactant foam formulation for CO₂ mobility control for CO₂ EOR and CO₂ storage. Experimental results compared the hybrid foaming solution to foam stabilized by only surfactant or nanoparticles, in the presence and absence of oil.

2. Materials and Procedures

2.1. Pore-Scale System

Two foaming agents were used to study foam generation, stability and coalescence. One was a nonionic surfactant (Huntsman *Surfonic L24-22*, Houston, TX, USA), a linear ethoxylated alcohol. The other foaming agent was a surface-modified spherical silica nanoparticle (Nouryon *Levasil CC301*, Amsterdam, The Netherlands). Foaming solutions were made by dissolving each foaming agent, either separately or combined, in 35,000 ppm NaCl brine at the concentrations shown in Table 1. CO₂ with 99.999% purity was used. The pore space was cleaned between injection cycles using 2-propanol-water azeotrope (IPA). For experiments in the presence of oil, a refined oil (n-Decane, C₁₀H₂₂) was used to obtain first-contact miscibility with CO₂.

Table 1. Composition of the foaming solutions used in pore- and core-scale experiments.

Foaming Agents	Concentration, Component	Scale
Nanoparticle (NP)	1500 ppm, <i>Levasil CC301</i>	Pore
Surfactant (SF)	3500 ppm, <i>Surfonic L24-22</i>	Core
	5000 ppm, <i>Surfonic L24-22</i>	Pore and Core
Hybrid (SF + NP)	3500 ppm, <i>Surfonic L24-22</i> + 1500 ppm, <i>Levasil CC301</i>	
	5000 ppm, <i>Surfonic L24-22</i> + 1500 ppm, <i>Levasil CC301</i>	
	5000 ppm, <i>Surfonic L24-22</i> + 150 ppm, <i>Levasil CC301</i>	Core

The micromodel was composed of a rectangular etched silicon wafer with an irregular porous structure bonded to a transparent borosilicate glass with dimensions of 26.96 mm × 22.50 mm (Figure 1) and a constant etching depth of 30 μm. The pore pattern was a simplified two-dimensional projection of real pore structures with connected pores that allow flow with discontinuous, irregularly shaped grains that provide tortuosity. The chemical composition of the crystalline silicon and borosilicate glass are similar to sandstone and are chemically inert to the injected fluids. Complete manufacturing procedures can be found elsewhere [26,27].

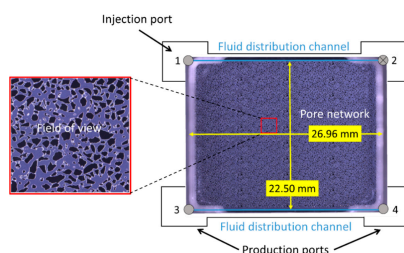


Figure 1. Dimensions of the micromodel, location of the flow ports and the fluid distribution channels. The focused field of view is shown on the left. Injection was into port 1 and production was from ports 3 and 4. Port 2 was closed. The entire pore network consisted of 36 repetitions of a single 749-grain pore pattern. The grain size distribution ranged from 100 to 79,000 μm² and the pore throat distribution ranged from 10 to 200 μm. The average pore throat length was 89 μm.

The micromodel had a porosity of 61%, permeability of 3000 mD and pore volume (PV) of 11.1 μL . The porous pattern (27,000 grains) had 36 (4×9) repetitions of a pore network with 749 unique grains. The grain size distribution of the 749-grain pattern ranged between 100 and 79,000 μm^2 and the pore throat width distribution ranged from 10 to 200 μm . Flow ports were located at each corner of the micromodel with the inlet at ports 1 and 2 and the outlet at ports 3 and 4. The micromodel was positioned in the bottom part of a two-piece polyether ether ketone (PEEK) plastic micromodel holder. The top part had an open window for direct visual observation. The micromodel holder was placed on a motorized stage below a microscope (Axio Zoom. V16, Zeiss, Jena, Germany). The microscope software controlled the zoom, focus, illuminator intensity, imaging, and the motorized stage. Additional details on the micromodel set-up can be found in [28].

2.2. Pore-Scale Procedure

The micromodel system was pressurized to 100 bar using a backpressure system at 25 °C for experiments in the absence and presence of oil. For experiments in the absence of oil, foaming solution was first injected to completely saturate the micromodel before injecting dense (liquid) phase CO_2 at a constant volumetric flow rate of 4 $\mu\text{L}/\text{min}$. The foaming solutions consisted of 1500 ppm nanoparticles, 5000 ppm surfactant, and two hybrid solutions with 5000 ppm surfactant combined with 1500 ppm or 150 ppm nanoparticles. An overview of the foaming solutions are listed in Table 1. A baseline, without foaming solution, was also conducted for comparison. For experiments in the presence of oil, the micromodel was initially saturated with distilled water before injecting six pore volumes of oil. Distilled water was then injected for an additional six pore volumes to achieve residual oil saturation. The micromodel was then saturated with the hybrid 3500 ppm surfactant and 1500 ppm nanoparticle foaming solution before CO_2 injection began at a constant rate of 1 $\mu\text{L}/\text{min}$. For all experiments, CO_2 was injected in port 1 (inlet), port 2 was closed and ports 3 and 4 (outlet) were open and kept at 100 bar using the backpressure system (Figure 1). The microscope settings (light intensity, aperture, and shutter time) were optimized for image processing and remained constant. Images were acquired of the entire micromodel with high spatial resolution (4.38 $\mu\text{m}/\text{pixel}$) by stitching multiple overlapping images. The image acquisition time of the porous pattern (121 separate images) was 73 s. A focused field of view was selected, which was representative of the remainder of the micromodel, for detailed analysis and to minimize the capillary end effects. Raw images from the experiments show the grains as dark and opaque and the pore space in a grayish-blue hue. The gas/liquid interfaces (lamellae) were white due to the diffusive ring-illuminator of the microscope. Foam generation and coalescence were also analyzed by utilizing the Python Library OpenCV [29] to identify bubble number and size.

2.3. Core-Scale System

The core-scale experiments used the same brine as the pore-scale work. In experiments with only surfactant in the foaming solution, a 3500 ppm or 5000 ppm concentration was used. In experiments with the hybrid foaming solutions, a 3500 ppm surfactant concentration was used with either 1500 ppm or 150 ppm nanoparticles to evaluate the concentration sensitivity for foam stabilization. See Table 1 for an overview of the foaming solutions. A single outcrop Bentheimer sandstone core was used for all experiments to eliminate the impacts of variable core properties. The core was cleaned and dried before being 100% saturated with brine under vacuum. Porosity and pore volumes were calculated based on the weight differential before and after saturation. Absolute permeability was measured between each experiment by injecting brine until a stable differential pressure was obtained for three different injection rates. The permeability of the core was 1400 millidarcy with a porosity of 24% (Table 2).

Table 2. Core properties of the Bentheimer sandstone used in the experimental work.

Core Properties	Value
Length (cm)	24.6 ± 0.01
Diameter (cm)	3.64 ± 0.01
Pore Volume (mL)	68.23
Porosity	0.24
Permeability (mD)	1400

2.4. Core-Scale Procedure

The brine-saturated sandstone core was wrapped in a 0.1-mm thick nickel foil to reduce the radial CO₂ diffusion into the confinement oil before installation into the Viton rubber sleeve. The core was then mounted in a vertically oriented Hassler-type core holder and placed inside a heating cabinet. Experimental conditions were set to 40 °C and 200 bar with a net overburden pressure of 70 bar. At these conditions, CO₂ is supercritical and has a similar density as in the pore-scale experiments. A differential pressure transducer and two absolute pressure transducers monitored pressure response at the inlet and outlet. Figure 2 shows the experimental set-up, modified from [30].

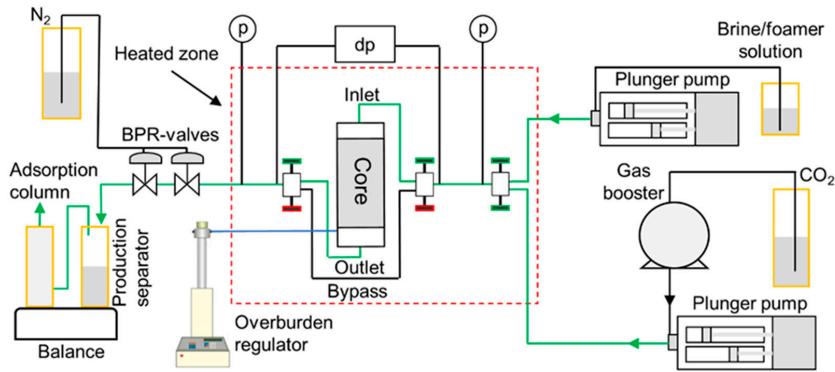


Figure 2. Experimental setup used for the core-scale foam experiments. Green lines indicate the fluid flow directions during the injection of CO₂ and the foaming solution. Pure CO₂ was pressurized by a gas booster and injected using a Quizix Q6000-10k plunger pump. Foaming solutions were injected using a Quizix Q5000-10k plunger pump. Injection was performed through a series of needle valves (marked green for open, red for closed) to the top of the core. Produced fluids were depressurized downstream through a series of backpressure regulator (BPR) valves and measured in the production separator and associated water adsorption column using a digital balance. Modified from [30].

Foam apparent viscosity is a measure of foam generation, strength and stability. An increase in apparent viscosity indicates a generation of foam and a higher value of apparent viscosity corresponds to a stronger foam. Foam apparent viscosity (μ_{app}) was quantified from the experimental superficial velocities and measured pressure drop [31] by

$$\mu_{app} = \frac{k \nabla p}{(u_l + u_g)} \quad (1)$$

where k is the absolute permeability of the porous media, ∇p is the measured pressure gradient and u_l and u_g are the superficial velocities of liquid and gas, respectively [32]. The effect of nanoparticles on foam strength and stability was evaluated by comparing dynamic experimental apparent viscosity results using foaming solutions with and without nanoparticles.

The injection scheme for the core-scale experiments in the absence of oil was adapted from [33]. First, a minimum of three PVs of foaming solution was injected to satisfy adsorption, displace the initial brine and fully saturate the pore space. Then, CO₂ was injected from the top of the vertically mounted core at a superficial velocity of 4 ft/day for approximately six PVs. Unsteady state apparent foam viscosities were calculated as a function of time (PVs injected) using Equation (1). A minimum of two experiments were performed for each individual foaming solution. A baseline experiment, without foaming solution, was also conducted for comparison. The core was cleaned between experiments by injecting solutions of IPA before being re-saturated with brine and then foaming solution.

The core-scale procedure in the presence of oil was developed to obtain approximately 30% residual oil before evaluating foam generation and stability. First, a primary drainage with n-Decane for nearly one PV was conducted followed by a waterflood for one PV. Foaming solution was then injected for at least three PVs at a low and high rate. Finally, CO₂ was continuously injected at 4 ft/day for 10 to 14 PVs. A minimum of two experiments was performed for each individual foaming solution.

3. Results and Discussion

3.1. Pore-Scale: Foam in the Absence of Oil

Figure 3 shows pore-scale images from four experiments with different foaming solutions. Three time steps are shown which correspond to pre-foam generation (PV = 1.3), peak foam generation and post-foam generation (PV = 20.1). The images show a focused field of view with CO₂ injection from the top to the bottom for each image. The dark opaque areas are grains, the grayish-blue open areas are the pore space and the thin white films are lamellae.

The experiment with only nanoparticles present (1500 NP) generated weak foam as indicated by the continuous distribution of open flow paths and very few lamellae or bubbles (Figure 3, left column). Thus, CO₂ mobility remained high and was comparable to the baseline without any foaming agent. CO₂ injection with the three surfactant-laden foaming solutions resulted in the generation of densely distributed, finely textured foam, which significantly reduced CO₂ mobility during the peak foam generation stage (5000 SF, 5000 SF + 1500 NP and 5000 SF + 150 NP). Individual bubbles were located near the ends of pore throats and several bubbles filled individual pore bodies, suggesting snap-off as the primary foam generation mechanism. Because the pore bodies had a larger area than the pore throats, repeated snap-off occurred until the pore body was filled with bubbles, a phenomenon also described by [34]. Dynamic observations also revealed many individual lamellae spanning across pore throats. These lamellae may have formed from the leave-behind mechanism because CO₂ was injected into a surfactant saturated porous media in a drainage-like process. The rise in capillary pressure during drainage can cause lamellae generation by both leave-behind and snap-off as gas enters the pore network [35].

Direct visual observations of the experiment with the hybrid foaming solution containing 5000 ppm surfactant and 1500 ppm nanoparticles revealed a continuous open flow path for CO₂ throughout the duration of the experiment (Figure 3, red line, 5000 SF + 1500 NP). No lamellae impeded CO₂ flow in this region and the CO₂ relative permeability was reduced by the presence of lamellae in the remainder of the pore network. Therefore, within this focused field of view, a continuous gas-foam was generated.

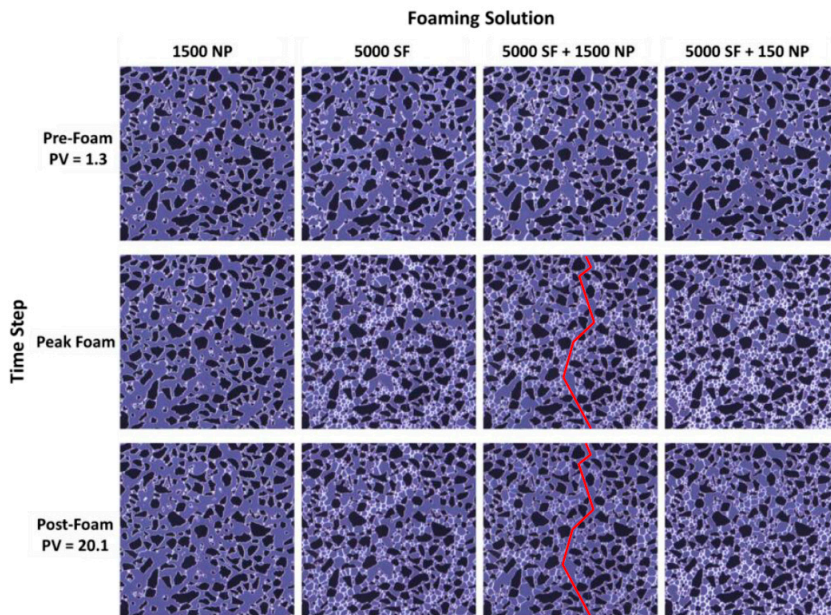


Figure 3. The pore-scale images of a focused field of view during the injection of dense phase CO_2 into a micromodel saturated with four different foaming solutions at 100 bar and 25°C . Experiments with different foaming solutions are shown across the top: 1500 ppm nanoparticles (1500 NP), 5000 ppm surfactant (5000 SF), hybrid 5000 ppm surfactant and 1500 ppm nanoparticles (5000 SF + 1500 NP) and hybrid 5000 ppm surfactant and 150 ppm nanoparticles (5000 SF + 150 NP). Injection was from top to bottom in each image. The dark opaque areas are grains, the grayish-blue open areas are the pore space and the thin white films are lamellae. Individual image dimensions are $2190 \times 2190 \mu\text{m}$. The grain size ranged from 100 to $79,000 \mu\text{m}^2$ and the pore throat distribution ranged from 10 to $200 \mu\text{m}$ for the entire micromodel.

Figure 4 quantifies the number of bubbles versus the bubble size for the images shown in Figure 3. Bubble number and size were used as indications of foam generation and strength where a higher bubble number corresponded to a finer textured foam. All foaming solutions containing surfactant-generated small bubbles ($\leq 10^3 \mu\text{m}^2$) at the peak generation stage. In the post-foam generation stage, the total number of bubbles decreased and their size increased; hence, the foam texture coarsened, increasing CO_2 mobility as CO_2 was continuously injected. The hybrid foaming solutions with either 1500 ppm or 150 ppm nanoparticles showed similar behavior, indicating that foam strength and stability was not sensitive to nanoparticle concentration when used together with the selected surfactant.

Pore-scale foam behavior was also analyzed by examining the total bubble number (N_i) as a function of the PV of CO_2 injected. The number of bubbles during foam generation and coalescence (N_{bubble}) were normalized to baseline (N_{baseline}) for the four foaming solutions. Figure 5 shows the normalized bubble number as a function of PV injected for each foaming solution for the focused field of view. Foam generation (as indicated by bubble number) increased from approximately 9 to 11 times the baseline for all foaming solutions. Peak foam generation was reached after approximately seven PVs of the CO_2 injected. After peak foam generation, the number of bubbles steadily decreased from bubble coarsening as the dominant coalescence mechanism as observed in Figure 3. The hybrid foaming solutions, containing nanoparticles and surfactant, had a limited impact on the number of bubbles and foam stability during continuous CO_2 injection.

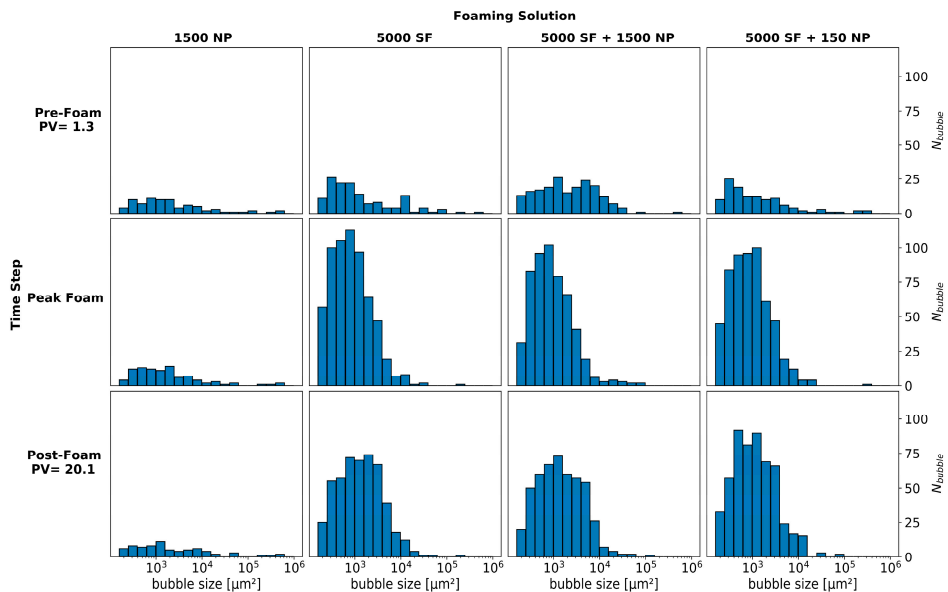


Figure 4. The number of bubbles (N_{bubble}) versus bubble size for the micromodel experiments with four different foaming solutions. Foaming solutions are shown across the top and include 1500 ppm nanoparticles (1500 NP), 5000 ppm surfactant (5000 SF), hybrid 5000 ppm surfactant and 1500 ppm nanoparticles (5000 SF + 1500 NP) and hybrid 5000 ppm surfactant and 150 ppm nanoparticles (5000 SF + 150 NP).

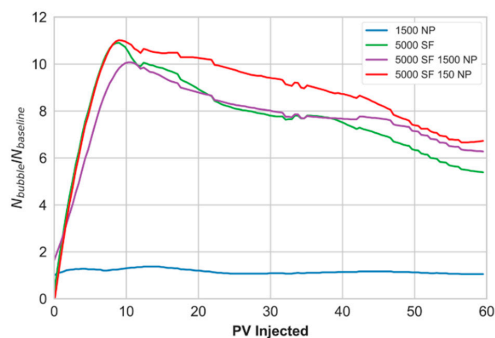


Figure 5. Development in normalized bubble number as a function of pore volume (PV) injected using four different foaming solutions for the focused field of view. The blue curve represents the foaming solution with 1500 ppm nanoparticles (1500 NP), the green curve represents the 5000 ppm surfactant solution (5000 SF), the purple curve represents the hybrid solution with 5000 ppm surfactant and 1500 ppm nanoparticles (5000 SF + 1500 NP) and the red curve represents the hybrid solution with 5000 ppm surfactant and 150 ppm nanoparticles (5000 SF + 150 NP).

The two-dimensional geometry of the micromodel likely resulted in multiple bubbles per pore because the widths of some of the pore throats were narrower than the pore throat depths. Therefore, pore-scale foam texture may not have a direct relation to foam in three-dimensional porous media. Many studies report that in situ foam usually consists of bubbles about the same size or larger than pore bodies based upon effluent analysis during laboratory experiments and the large flow resistance

for bubbles smaller than pores [12,36,37]. In addition, most mechanistic foam models [38–40] assume a single bubble per pore and that discrete bubbles flow through the porous media, where foam strength is controlled by foam texture (bubble size). The latter assumptions are supported by the pore-scale observations reported here.

3.2. Pore-Scale: Foam in the Presence of Oil

Dynamic foam generation in the presence of oil was evaluated by injecting CO₂ into a micromodel saturated with a hybrid foaming solution and oil. The aim was to evaluate the impact of oil on foam generation and gain insight on the influence of oil/water emulsions during CO₂ foam processes. Figure 6 shows the pore-scale images of the unsteady-state CO₂ injection in the presence of oil with the hybrid foaming solution containing 3500 ppm surfactant and 1500 ppm nanoparticles. Three stages of the experiment are shown which correspond to before CO₂ injection, the start of CO₂ injection, and during CO₂ injection. Each image was acquired with 75 s between each time step.

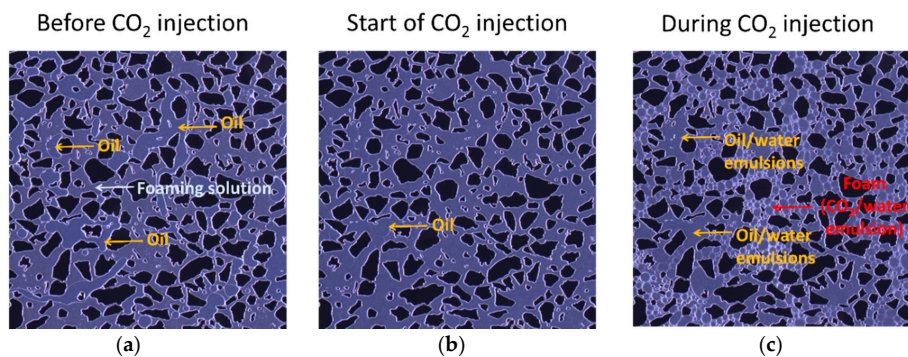


Figure 6. Pore-scale images of a focused field of view during the injection of dense phase CO₂ into a micromodel saturated with a hybrid foaming solution and oil at 100 bar and 25 °C. Three stages of the experiment are shown which correspond to: (a) before CO₂ injection; (b) the start of CO₂ injection; and (c) during CO₂ injection. Injection was from top to bottom in each image. The dark opaque areas are grains, the grayish-blue open areas are the pore space filled and the thin white films are the lamellae. Individual image dimensions are 2190 × 2190 μm. The grain size ranged from 100 to 79,000 μm² and the pore throat distribution ranged from 10 to 200 μm for the entire micromodel.

Before CO₂ injection, the micromodel was initially saturated with foaming solution and oil (Figure 6a). Foaming solution appears as the continuous liquid phase, whereas oil is seen as isolated globules in interconnected pores. At the start of CO₂ injection (Figure 6b), the oil globules faded due to miscibility between CO₂ and oil. As CO₂ injection continued, the oil was displaced by CO₂ and foam readily generated in areas where oil was not present. Oil not displaced formed oil/water emulsions and occupied pores without foam present (Figure 6c). The foam (CO₂/water emulsion) had thicker lamellae compared to the oil/water emulsions likely due to interfacial tension differences at these conditions as also observed in [41]. Compared to foam (CO₂/water emulsion) alone, the combined effect of oil/water emulsions and foam further reduced CO₂ mobility. This resulted in increased “foam” strength as also observed in the core-scale experiments in the presence of oil (discussed in Section 3.4).

3.3. Core-Scale: Foam in the Absence of Oil

Dynamic foam generation and stability in the absence of oil was evaluated by injecting CO₂ into cores saturated with different foaming solutions. This set of experiments established conditions to investigate foam behavior during prolonged periods of CO₂ injection in a drainage-like process. Figure 7a shows the apparent viscosity versus pore volume of CO₂ injected for the CO₂ foam stability

scans with foaming solutions containing only surfactant at concentrations of 3500 ppm (green curves) and 5000 ppm (blue curves). Figure 7b shows the results from the experiments using the two hybrid foaming solutions with 3500 ppm surfactant and 150 ppm nanoparticles (orange curves) and 3500 ppm surfactant and 1500 ppm nanoparticles (red curves). A baseline scan, without foaming solution, is also shown in each figure for comparison (black curves).

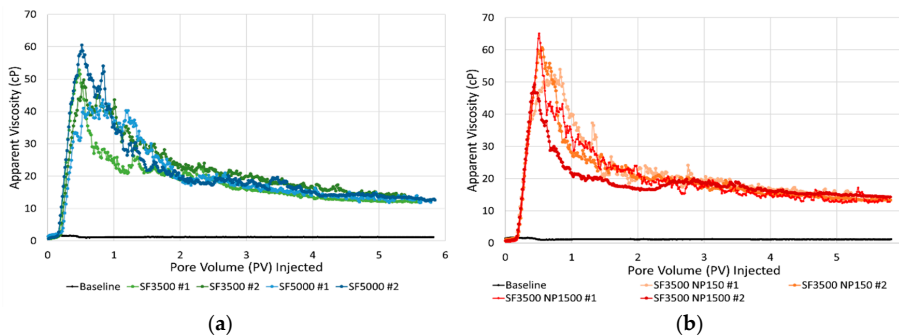


Figure 7. Apparent viscosity versus pore volume of the CO₂ injected for the unsteady state CO₂ injections into cores pre-saturated with foaming solutions containing: (a) 3500 ppm surfactant (green curves) and 5000 ppm surfactant (blue curves); (b) hybrid foaming solutions containing 3500 ppm surfactant and 150 ppm nanoparticles (orange curves) and 3500 ppm surfactant and 1500 ppm nanoparticles (red curves). The black curve is the baseline with only brine.

For all experiments, the rapid and linearly increasing apparent viscosity until 0.2 PV injected indicated that foam was generated as CO₂ invaded the core saturated with foaming solution. Apparent viscosity steadily increased, from 0.2 to 0.5 PV injected, as foam continued to generate and propagate into the core. A peak in apparent viscosity (foam strength) was achieved after approximately 0.5 PV was injected. The magnitude of the peak apparent viscosity varied from 45 to 65 cP for all experiments. The peak in apparent viscosity indicated a transition from a period of predominantly foam generation to predominantly foam coalescence. The development of a continuous CO₂ flow path not impeded by lamellae caused the foam to coalesce, likely related to a combination of bubble rupture and foam displacement. The CO₂ flow path rapidly reduced the apparent viscosity just before one PV was injected. After about six PVs were injected, the initial CO₂ viscosity was not fully recovered due to trapped bubbles in the pore space, which continued to reduce CO₂ mobility.

The difference in dynamic foam generation and coalescence processes for the foaming solutions with and without nanoparticles were insignificant. Including nanoparticles in the surfactant-laden foaming solution did not result in a more stable foam and the type of foaming solutions did not clearly affect the apparent viscosity of the foam. Therefore, the surfactant contributed mostly to foam generation and the nanoparticles had only minor impacts on the foam strength and stability in these experiments. The experiments with the hybrid foaming solutions (Figure 7b) revealed similar foam behavior independent of nanoparticle concentration. Despite an order of magnitude difference in nanoparticle concentration, the measured apparent viscosities and stability of the foam were similar. Thus, the nanoparticle concentrations of 150 ppm gave similar performance as the nanoparticle concentrations of 1500 ppm when used with the selected surfactant. The next set of experiments focused on evaluating the same foaming solutions in the presence of oil, a condition known to destabilize some surfactant-based foams.

3.4. Core-Scale: Foam in the Presence of Oil

Dynamic foam generation and stability for foaming solutions with and without nanoparticles in the presence of oil was evaluated by injecting CO_2 into a core saturated with each foaming solution. The core contained a residual oil saturation of around 30% prior to being flooded with foaming solution and then CO_2 . Each experiment was conducted a minimum of two times for reproducibility. Figure 8 shows the average apparent viscosity (cP) versus the pore volume of CO_2 injected for the unsteady state CO_2 foam stability scans in the presence of oil. Experiments using the foaming solution with only surfactant are shown with the blue curve and experiments with the hybrid foaming solution are shown with the red curve.

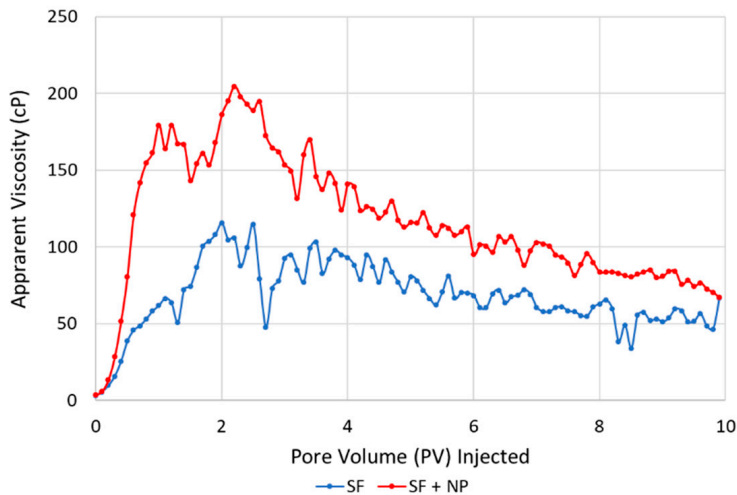


Figure 8. Apparent viscosity versus pore volume of the CO_2 injected for the unsteady state CO_2 injections in cores with residual oil (S_{or}) and pre-saturated with a hybrid foaming solution containing surfactant and nanoparticles (SF + NP, red curve) or a foaming solution containing only surfactant (SF, blue curve).

Both types of foaming solutions generated foam within the first 0.2 PV injected. However, the hybrid foaming solution generated foam more rapidly (faster increase in apparent viscosity) than the solution containing only surfactant. In addition, the hybrid foaming formulation generated a stronger (higher apparent viscosity) foam, compared to the solution containing only surfactant. The increased apparent viscosity for both types of solution indicated that each formulation generated foam with the residual oil present.

Apparent foam viscosity values with the hybrid solution in the presence of oil (Figure 8, red curve) were nearly three times as high as the experiments without oil present (Figure 7b). In the presence of oil, the foaming solution with only surfactant (Figure 8, blue curve) had foam-apparent viscosity values about twice as high as experiments in the absence of oil (Figure 7a). This is related to the development of oil/water emulsions, which were likely stabilized by each respective foaming agent. The emulsions influenced the calculated apparent viscosities (differential pressure) and are indistinguishable from foam (CO_2 /water emulsion). Nonetheless, the oil/water emulsions highlight an important facet of the CO_2 foam process, which can be beneficial to enhancing oil recovery by increasing the capillary number (increased viscous forces and lower interfacial tension) [42].

3.5. From Pore- to Core-Scale

The similarity in foam generation and coalescence during unsteady-state CO₂ injections at the pore- and core-scale is striking. Figures 5 and 7 reveal dynamic foam generation and coalescence processes with similar behavior at two different length scales. The experiments in this work were characterized by a period of rapid foam generation during drainage-like CO₂ injection and a period of foam coalescence during prolonged CO₂ injection. The decline in foam strength, at both scales, was related to the development of open CO₂ flow paths through the generated foam. This phenomenon was a result of bubble coarsening from diffusion. The pore-scale observations unlocked real-time insights on in situ foam behavior that may help explain the observations from the core-scale experiments. Since foam was rapidly generated at both scales (due to ideal conditions for foam generation), the coalescence mechanisms during continued CO₂ injection at the pore-scale may be applied at the core-scale with some level of confidence. It is understood that foam will dry out as more CO₂ is injected and not supplemented with additional surfactant solution. Here, we showed one of the physical mechanisms responsible for such behavior.

In addition, the experiments in the presence of oil revealed the importance of stable oil/water emulsions on the CO₂ foam process. The insights from pore-scale experiments with oil shed light on the influence of oil/water and CO₂/water emulsions on CO₂ mobility reduction. Higher foam apparent viscosities were calculated for the core-scale experiments with oil present and were likely related to the development of the oil/water emulsions. Because apparent viscosity is used as an indication of foam generation and strength in laboratory experiments, care must be taken when interpreting the results from coreflood studies with the presence of stable oil/water emulsions. These emulsions can influence the calculated apparent viscosities (based on differential pressures) and may contribute to reducing CO₂ mobility.

4. Conclusions

This work presented a multi-scale investigation of hybrid nanoparticle–surfactant foam for CO₂ mobility control for CO₂ EOR and CO₂ storage. High-pressure micromodel experiments and high-pressure/high-temperature core floods evaluated a hybrid surfactant and nanoparticle foaming solution and foaming solutions with only surfactant or nanoparticles, in the presence and absence of oil. The following conclusions can be drawn:

- Direct pore-scale observations of dense phase CO₂ injection into a micromodel saturated with foaming solutions containing only surfactant or a hybrid nanoparticle–surfactant foaming solution revealed snap-off as the primary foam generation mechanism and leave-behind as a secondary foam generation mechanism.
- At the pore-scale, foam readily generated in areas where oil was not present and oil/water emulsions initially occupied pores without foam present.
- All foaming solutions containing surfactant generated foam in the presence and absence of oil, whereas foaming solution only containing nanoparticles did not. Thus, surfactant was the main foam generator and nanoparticles may be more important for foam stabilization.
- Foam strength was not sensitive to nanoparticle concentration when used together with surfactant in the tested foaming solutions.
- At the core-scale, all foaming solutions rapidly generated foam in the presence of residual oil.
- Foam apparent viscosity values with the hybrid foaming solution, in the presence of oil, were nearly three times as high as the experiments without oil. This was related to the development of oil/water emulsions, which were likely stabilized by the foaming agents.
- A link is proposed between direct pore-scale visual observations and quantitative core-scale measurements. The combined influence of stable oil/water emulsions and foam (CO₂/water emulsions) may be beneficial for increasing the capillary number by achieving higher apparent viscosity and lower interfacial tension.

- The experiments in this work were characterized by a period of rapid foam generation during drainage-like CO₂ injection and a period of foam coalescence during prolonged CO₂ injection. The decline in foam strength is related to the development of open CO₂ flow paths through the generated foam.
- Increased apparent viscosities with foam reduced CO₂ mobility at multiple length scales, which can improve volumetric sweep efficiency in field-scale CO₂ EOR and CO₂ storage processes.

Author Contributions: Conceptualization, Z.P.A., T.F., J.G., M.F.; methodology, Z.P.A., T.F., J.G., B.B., M.F.; formal analysis, Z.P.A., T.F., J.G.; investigation, T.F., B.B., A.S.; writing—original draft preparation, Z.P.A.; review and editing, T.F., J.G., B.B., M.F.; supervision, Z.P.A., J.G., M.F.; project administration, M.F.; funding acquisition, M.F. All authors have read and agreed to the published version of the manuscript.

Funding: This research was funded by the Norwegian Research Council, grant numbers 268216, 294886 and 301201.

Conflicts of Interest: The authors declare no conflict of interest.

References

1. IPCC. *Climate Change 2014: Chapter 1: Mitigation of Climate Change. Contribution of Working Group III to the Fifth Assessment Report of the Intergovernmental Panel on Climate Change*; Victor, D.G., Zhou, D., Ahmed, E.H.M., Dadhich, P.K., Olivier, J.G.J., Rogner, H.-H., Sheikho, K., Yamaguchi, M., Eds.; Cambridge University Press: Cambridge, UK; New York, NY, USA, 2014.
2. Enick, R.M.; Olsen, D.K.; Ammer, J.R.; Schuller, W. *Mobility and Conformance Control for CO₂ EOR via Thickeners, Foams, and Gels—A Detailed Literature Review of 40 Years of Research*; DOE/NETL-2012/1540; USDOE, National Energy Technology Laboratory: Washington, DC, USA, 2012.
3. Hoefner, M.L.; Evans, E.M. CO₂ Foam: Results from Four Developmental Field Trials. *SPE Reserv. Eng.* **1995**, *10*, 273–281. [[CrossRef](#)]
4. Martin, F.D.; Stevens, J.E.; Harpole, K.J. CO₂-Foam Field Test at the East Vacuum Grayburg/San Andres Unit. *SPE Reserv. Eng.* **1995**, *10*, 266–272. [[CrossRef](#)]
5. Rudden, W.R. Foams in Enhanced Oil Recovery. In *Foams Theory, Measurements, and Applications*; Prud'homme, R.K., Khan, S.A., Eds.; Marcel Dekker, Inc.: New York, NY, USA, 1996; Volume 57, Chapter 11, pp. 414–464.
6. David, A.; Marsden, S.S. The Rheology of Foam. In Proceedings of the 44th Annual Fall Meeting of SPE of AIME, Denver, CO, USA, 28 September–1 October 1969. [[CrossRef](#)]
7. Espinosa, D.; Caldelas, F.; Johnston, K.; Bryant, S.L.; Huh, C. Nanoparticle-Stabilized Supercritical CO₂ Foams for Potential Mobility Control Applications. In Proceedings of the SPE Improved Oil Recovery Symposium, Tulsa, OK, USA, 24–28 April 2010.
8. Rognmo, A.U.; Al-Khayyat, N.; Heldal, S.; Vikingstad, I.; Eide, Ø.; Fredriksen, S.B.; Alcorn, Z.P.; Graue, A.; Bryant, S.L.; Kovscek, A.R.; et al. Performance of Silica Nanoparticles in CO₂-Foam for EOR and CCUS at Tough Reservoir Conditions. In Proceedings of the SPE Norway One-Day Seminar, Bergen, Norway, 18 April 2019.
9. Ogolo, N.A.; Olafuyi, O.A.; Onyekonwu, M.O. Enhanced Oil Recovery Using Nanoparticles. In Proceedings of the SPE Saudi Arabia Section Technical Symposium and Exhibition, Al-Khobar, Saudi Arabia, 8–11 April 2012.
10. Yu, J.; Wang, S.; Liu, N.; Lee, R. Study of Particle Structure and Hydrophobicity Effects on the Flow Behavior of Nanoparticle-Stabilized CO₂ Foam in Porous Media. In Proceedings of the SPE Improved Oil Recovery Symposium, Tulsa, OK, USA, 12–16 April 2014.
11. Bennetzen, M.; Mogensen, K. Novel Applications of Nanoparticles for Future Enhanced Oil Recovery. In Proceedings of the International Petroleum Technology Conference, Kuala Lumpur, Malaysia, 10–12 December 2014.
12. Ettinger, R.A.; Radke, C.J. Influence of Texture on Steady Foam Flow in Berea Sandstone. *SPE Reserv. Eng.* **1992**, *7*, 83–90. [[CrossRef](#)]
13. Chen, M.; Yortos, Y.C.; Rossen, W.R. A Pore-Network Study of the Mechanisms of Foam Generation. In Proceedings of the SPE Annual Technical Conference and Exhibition, Houston, TX, USA, 26–29 September 2004. SPE-90939.
14. Farajzadeh, R.; Andrianov, A.; Krastev, R.; Hirasaki, G.J.; Rossen, W.R. Foam–oil interaction in porous media: Implications for foam assisted enhanced oil recovery. *Adv. Colloid Interface Sci.* **2012**, *183*, 1–13. [[CrossRef](#)] [[PubMed](#)]

15. Harkins, W.D.; Feldman, A. Films: The spreading of liquids and the spreading coefficient. *J. Am. Chem. Soc.* **1922**, *44*, 2665–2685. [[CrossRef](#)]
16. Schramm, L.L.; Novosad, J.J. Micro-visualization of Foam Interactions with Crude Oil. *Colloids Surf.* **1990**, *46*, 21–43. [[CrossRef](#)]
17. Marsden, S.S. *Foams in Porous Media—SUPRI TR-49*; U.S. Department of Energy Topical Report; 1986. Available online: <https://www.osti.gov/biblio/5866567> (accessed on 27 June 2020).
18. Talebian, S.H.; Masoudi, R.; Tan, I.M.; Zitha, P.L.J. Foam Assisted CO₂ EOR; Concepts, Challenges and Applications. In Proceedings of the SPE Enhanced Oil Recovery Conference, Kuala Lumpur, Malaysia, 2–4 July 2013.
19. Farajzadeh, R. Enhanced Transport Phenomena in CO₂ Sequestration and CO₂ EOR. Ph.D. Thesis, Faculty of Civil Engineering and Geosciences, Delft University of Technology, Delft, The Netherlands, 2009.
20. Kristiansand, T.S.; Holt, T. Properties of Flowing Foam in Porous media Containing Oil. In Proceedings of the SPE/DOE Improved Oil Recovery Symposium, Tulsa, OK, USA, 22–24 April 1992.
21. Kovscek, A.R.; Radke, C.J. Fundamentals of Foam Transport in Porous Media. In *Foams: Fundamentals and Applications in the Petroleum Industry*; American Chemical Society: Washington, DC, USA, 1994; pp. 115–163.
22. Saint-Jalmes, A. Physical chemistry in foam drainage and coarsening. *Soft Matter* **2006**, *2*, 836–849. [[CrossRef](#)]
23. Marchalot, J.; Lambert, J.; Cantat, I.; Tabeling, P.; Jullien, M.-C. 2D foam coarsening in a microfluidic system. *EPL (Europhys. Lett.)* **2008**, *83*, 64006. [[CrossRef](#)]
24. Falls, A.; Musters, J.; Ratulowski, J. The Apparent Viscosity of Foams in Homogeneous Bead Packs. *SPE Reserv. Eng.* **1989**, *4*, 155–164. [[CrossRef](#)]
25. Farajzadeh, R.; Lotfollahi, M.; Eftekhari, A.A.; Rossen, W.R.; Hirasaki, G.J.H. Effect of Permeability on Implicit-Texture Foam Model Parameters and the Limiting Capillary Pressure. *Energy Fuels* **2015**, *29*, 3011–3018. [[CrossRef](#)]
26. Buchgraber, M.; Al-Dossary, M.; Ross, C.M.; Kovscek, A.R. Creation of a dual-porosity micromodel for pore-level visualization of multiphase flow. *J. Pet. Sci. Eng.* **2012**, *86*, 27–38. [[CrossRef](#)]
27. Hornbrook, J.W.; Castanier, L.M.; Pettit, P.A. Observation of Foam/Oil Interactions in a New, High-Resolution Micromodel. In Proceedings of the SPE Annual Technical Conference and Exhibition, Dallas, TX, USA, 6–9 October 1991; Society of Petroleum Engineers: Houston, TX, USA, 1991.
28. Benali, B. Quantitative Pore-Scale Analysis of CO₂ Foam for CCUS. Master’s Thesis, University of Bergen, Bergen, Norway, December 2019. Available online: <http://hdl.handle.net/1956/21300> (accessed on 27 June 2020).
29. Bradski, G. The OpenCV Library. *Dr. Dobb’s J. Softw. Tools* **2000**, *25*, 120–125.
30. Føyen, T.; Alcorn, Z.P.; Fernø, M.A.; Holt, T. 2020 CO₂ Mobility Reduction Using Foam Stabilized by CO₂- and Water-Soluble Surfactants. *J. Pet. Sci. Eng.* **2020**. [[CrossRef](#)]
31. Hirasaki, G.J.; Lawson, J.B. Mechanisms of Foam Flow in Porous Media: Apparent Viscosity in Smooth Capillaries. *SPE J.* **1985**, *25*, 176–190. [[CrossRef](#)]
32. Jones, S.A.; Laskaris, G.; Vincent-Bonnieu, S.; Farajzadeh, R. Surfactant Effect on Foam: From Core Flood Experiments to Implicit-Texture Foam- Model Parameters. In Proceedings of the SPE Improved Oil Recovery Conference, Tulsa, OK, USA, 11–13 April 2016; SPE-179637. [[CrossRef](#)]
33. Føyen, T.; Brattækås, B.; Fernø, M.; Barrabino, A.; Holt, T. Increased CO₂ storage capacity using CO₂-foam. *Int. J. Greenh. Gas Control* **2020**, *96*, 103016. [[CrossRef](#)]
34. Chambers, K.T.; Radke, C.J. *Interfacial Phenomena in Oil Recovery*; Morrow, N.R., Ed.; Marcel Dekker: New York, NY, USA, 1990.
35. Ranshoff, T.C.; Radke, C.J. Mechanics of Foam Generation in Glass Bead Packs. *SPE Reserv. Eng.* **1988**, *3*, 573–585. [[CrossRef](#)]
36. Rossen, W.R. Theory of mobilization pressure gradient of flowing foams in porous media: III. Asymmetric lamella shapes. *J. Colloids Interface Sci.* **1990**, *136*, 38–53. [[CrossRef](#)]
37. Falls, A.H.; Hirasaki, G.J.; Patzek, T.W.; Gauglitz, D.A.; Millerand, D.D.; Ratulowski, T. Development of a Mechanistic Foam Simulator: The Population Balance and Generation by Snap-Off. *SPE Reserv. Eng.* **1988**, *3*, 884–892. [[CrossRef](#)]
38. Kovscek, A.R.; Patzek, T.W.; Radke, C.J. A Mechanistic Population Balance Model for Transient and Steady-State Foam Flow in Boise Sandstone. *Chem. Eng. Sci.* **1995**, *50*, 3783–3799. [[CrossRef](#)]
39. Simjoo, M.; Zitha, P.L.J. Modeling and Experimental Validation of Rheological Transition during Foam Flow in Porous Media. *Transp. Porous Media* **2020**, *131*, 315–332. [[CrossRef](#)]

40. Ma, K.; Ren, G.; Mateen, K.; Moreland, D.; Cordelier, P. Modeling techniques for foam flow through porous media. *SPE J.* **2015**, *20*, 453–470. [[CrossRef](#)]
41. Gauteplass, J.; Follesø, H.N.; Graue, A.; Kovscek, A.R.; Fernø, M.A. Visualization of pore-level displacement mechanisms during CO₂ injection and EOR processes. In Proceedings of the EAGE IOR—17th European Symposium on Improved Oil Recovery, St. Petersburg, Russia, 16–18 April 2013.
42. Simjoo, M.; Dong, Y.; Andrianov, A.; Talanana, M.; Zitha, P.L.J. A CT Scan Study of Immiscible Foam Flow in Porous Media for EOR. In Proceedings of the SPE EOR Conference at Oil and Gas West Asia, Muscat, Oman, 16–18 April 2012.



© 2020 by the authors. Licensee MDPI, Basel, Switzerland. This article is an open access article distributed under the terms and conditions of the Creative Commons Attribution (CC BY) license (<http://creativecommons.org/licenses/by/4.0/>).

Paper 2

Pore-level Ostwald ripening of CO₂ foams at reservoir pressure

Benyamine Benali¹, Aleksandra Sæle¹, Na Liu¹, Martin A. Fernø¹, Zachary Paul Alcorn¹

¹ Department of Physics and Technology, University of Bergen, Norway

1. Abstract

The success of foam to reduce CO₂ mobility in CO₂ enhanced oil recovery (EOR) and CO₂ storage operations depends on foam stability in the reservoir. Foams are thermodynamically unstable and factors such as surfactant adsorption, the presence of oil, and harsh reservoir conditions can cause the foam to destabilize. Pore-level foam coarsening and anti-coarsening mechanisms are not, however, fully understood and characterized at reservoir pressure. Using lab-on-a-chip technology, we probe CO₂ foam stability and the impact of Ostwald ripening using dynamic pore-scale observations. Three types of pore-level coarsening were observed: 1. large bubbles growing at the expense of small bubbles, at high aqueous phase saturations, unrestricted by the grains; 2. large bubbles growing at the expense of small bubbles, at low aqueous phase saturation, restricted by the grains; and 3. equilibration of plateau borders. Type 3 coarsening led to stable CO₂ foam states 8 times faster than type 2, and 10 times faster than type 1. Anti-coarsening, where CO₂ diffused from a large bubble to a small bubble was also observed. The experimental results also compared CO₂ foam generated with hybrid nanoparticle-surfactant solution to CO₂ foam stabilized by only surfactant or nanoparticles. Doubling the surfactant concentration from 2500 ppm to 5000 ppm, and adding 1500 ppm of nanoparticles to the 2500 ppm surfactant-based solution resulted in stronger foam, which resisted Ostwald ripening. Dynamic pore-scale observations revealed gas diffusion from small, high-curvature bubbles to large, low-curvature bubbles and that the overall curvature of the bubbles decreased with time.

2. Keywords

CO₂ foam, Ostwald Ripening, Foam stability, Foam coarsening, Micromodels, Pore-scale.

3. Article Highlights

- A comprehensive laboratory investigation of CO₂ foam stability and the impact of Ostwald ripening.
- Pore-level foam coarsening and anti-coarsening mechanisms insights.

4. Introduction

Carbon capture, utilization and sequestration (CCUS) is essential for limiting global warming and achieving the climate goals of the Paris Agreement [1]. CCUS involves capturing CO₂ from industrial sources, such as cement plants or power plants, and injecting it into subsurface reservoirs for enhanced oil recovery (EOR) and geological carbon sequestration [2]. CO₂ injection for EOR and carbon storage is a proven technology that has been widely implemented over the last decades [3, 4]. Although CO₂ EOR and sequestration has been successfully performed, the effectiveness of CO₂ EOR and CO₂ storage is limited by challenges associated with high CO₂ mobility and reservoir heterogeneity [5]. The low viscosity and density of CO₂ compared to other reservoir fluids can lead to viscous fingering and gravity override, while reservoir heterogeneity can cause channeling through high permeable zones [6-8]. This

results in poor sweep efficiency, high producing gas-oil ratios, low oil recovery, and reduced CO₂ sequestration capacity [9]. CO₂ foam can reduce these flow instabilities by increasing CO₂ viscosity, reducing its relative permeability and diverting flow from high to lower permeability zones [10-13].

CO₂ foam is a dispersion of a discontinuous gas (CO₂) in a continuous liquid phase [14]. Foam can be generated in the porous media by injecting a foaming solution such as surfactant and/or nanoparticles and CO₂, either simultaneously or in alternating slugs [15]. To maintain the stability of surfactant-based foams in the reservoir is challenging due to various factors such as surfactant adsorption, the presence of oil, and the harsh reservoir conditions, which can cause the foam to break [16]. Nanoparticles can add stability to surfactant-based foams by withstanding high temperature and high salinity conditions [17]. However, nanoparticles alone generate weak foam compared to surfactants [18, 19]. Recent research has shown that the addition of silica nanoparticles to surfactant-based foam may increase the stability and improve displacement efficiency for CO₂ EOR and CO₂ storage applications [20, 21].

CO₂ foam bubbles are separated by continuous liquid films called lamellae, whereas a three-lamellae link is referred to as a plateau border. Foams are thermodynamically unstable and their longevity depends on the stability of single lamellae [22]. Lamellae move and rearrange to achieve minimum interfacial free energy [23]. This results in a change in foam texture (size and the number of bubbles) and a decrease in foam stability, which is driven by three mechanisms: (1) drainage, where lamella thinning is caused by gravity or capillary suction [24], (2) coalescence, where bubbles unite and form larger bubbles due to lamella rupture [25] and (3) coarsening, where gas diffuses through lamella due to capillary pressure differences, known as Ostwald ripening [26].

The stability of bulk foams is typically measured by the decrease in the volume or height of the foam with time [27]. The average bubble size in bulk is usually smaller than the outer boundaries and instabilities are mostly related to drainage and coalescence mechanisms [28, 29]. In porous media, the bubbles are the same size or larger than the pore bodies [30] with a high fraction (>0.97) of trapped bubbles due to large capillary forces [26]. At pore scale, the drainage mechanism is insignificant due to the more dominant effect of surface forces compared to the volumetric forces [28]. Bubble coalescence is also significantly reduced and can be neglected for surfactant-based foams where the surfactants improve the interfacial properties of the lamella and constrain bubble coalescence [31, 32]. Therefore, Ostwald ripening is the critical mechanism affecting foam stability in porous media.

Ostwald ripening is a well-known phenomenon in bulk systems [33-36]. It occurs due to the transport of gas from smaller bubbles with small radius, high curvature and high internal pressure to larger bubbles with large radius, low curvature and low internal pressure resulting in the disappearance of smaller bubbles [37, 38]. However, the process is more complex in porous media, because the bubbles cannot freely grow, and the coarsening is affected by the geometric confinement of the pores [28, 39]. Ostwald ripening in porous media typically leads to stable states, due to both bubble coarsening and anti-coarsening. The anti-coarsening phenomenon occurs when bubbles are deformed by the geometric confinement of the pore network leading to a reversed gas diffusion from larger bubbles to smaller bubbles [32, 40].

Pore scale experiments show that the coarsening does not conform to the unrestricted growth laws [41]. Instead, the bubbles coarsen to the pore size, and at the end of the coarsening, the lamellae rest in minimum-energy configurations in the pore throats [40, 42]. The grains, pore network, and pore throat sizes affect the Ostwald ripening mechanism and can result in different bubble shapes and sizes i.e., foam texture [32, 43]. Therefore, performing experiments in a realistic pore network is crucial to understanding CO₂ foam dynamics in porous media.

Micromodels can be used for direct visualization of CO₂ foam flow through porous media. They are two-dimensional flow cells that contain a pore network and transparent glass for visualization [44]. High pressure micromodels are ideal for studying CO₂ foam at reservoir conditions and enable gathering quantitative and qualitative data of the Ostwald ripening mechanism by using image analysis techniques to monitor the bubble size and distribution [45, 46].

Few attempts have been made to understand coarsening and anti-coarsening mechanisms in a realistic pore network at reservoir conditions. Therefore, the aim of this work was to study the Ostwald ripening mechanism for a static CO₂ foam generated with different foaming solutions in a realistic pore network at 100 bars. A secondary objective was to compare CO₂ foam generated by hybrid nanoparticle-surfactant solution to CO₂ foam stabilized by only surfactant or nanoparticles. The foam bubbles were monitored using high resolution images acquired by a Zeiss microscope. Quantitative data was obtained by image analysis using Python libraries as OpenCV, and skimage.

5. Materials and methods

5.1. Fluid preparation

Brine (3.5 wt.% NaCl) with fluorescein sodium salt (500 PPM C₂₀H₁₀Na₂O₅, F6377 Sigma-Aldrich) was used for all aqueous phases (Table 1), where the fluorescent tracer was added to the solution to distinguish between the water and CO₂ phases. All the aqueous solutions were filtered using a sterile 0.2 μm cellulose acetate filter (514-0061, VWR) before injected into the micromodel. Two foaming agents were used: (1) Surfonic L24-22, a non-ionic, water-soluble surfactant with linear ethoxylated alcohol from Indorama Ventures and (2) Levasil CC301, a surface-modified spherical silica nanoparticle from Nouryon. CO₂ of 99.999% purity was used for foam generation and to saturate the aqueous solution before injecting it into the micromodel. Four foaming solutions were prepared by mixing brine with surfactant, nanoparticle, or a hybrid combination of both (Table 1).

Table 1: Composition of aqueous solutions

Aqueous Solution	Concentration, Component
Brine	35 000 ppm, NaCl
Fluorescent dye	500 ppm, fluorescein sodium salt
SF 5000	5000 ppm, Surfonic L24-22
SF2500	2500 ppm, Surfonic L24-22
SF2500 + NP1500	2500 ppm, Surfonic L24-22 + 1500 ppm, Levasil CC301
NP1500	1500 ppm, Levasil CC301
IPA	877 000 ppm, 2-propanol-water azeotrope
Hydrogen peroxide	300 000 ppm, H₂O₂

5.2. Micromodel and holder

The high-pressure micromodel enabled direct visualization of pore-scale interactions between different fluids and rock grains at reservoir conditions [44]. It consisted of an optically transparent borosilicate glass on the top bonded to an etched silicon wafer with a representative pore structure. The 2D pore network was generated from thin sections of a natural sandstone and etched on the silicon wafer by the deep reactive ion etching method with a constant depth of 30 μm to get vertical pore walls and sharp edges. However, when reproducing a 3D porous matrix obtained from a real reservoir rock to 2D, some modifications were made to connect all the pores, resulting in higher porosity and permeability compared to cylindrical sandstone samples. Detailed production procedures can be found in [47]. The unique pore network (7.2 x 2.8 mm) was repeated 36 times (4 x 9) with an overlap, resulting

in a total pore network of 27 x 21 mm (Figure 1). In addition, the micromodel had two etched fluid distribution channels (200 μm width), one at the top and one at bottom. Four flow ports were etched through the silicon wafer to connect with external environments. Micromodel properties are summarized in Table 2. The porosity and permeability were calculated to be 0.61 and 2.97 Darcy, respectively. The pore volume (PV) with a constant etching depth of 30 μm was 11.1 μL [48]. The pores were classified using snow algorithm [49], and the average pore size was 3896 μm^2 .

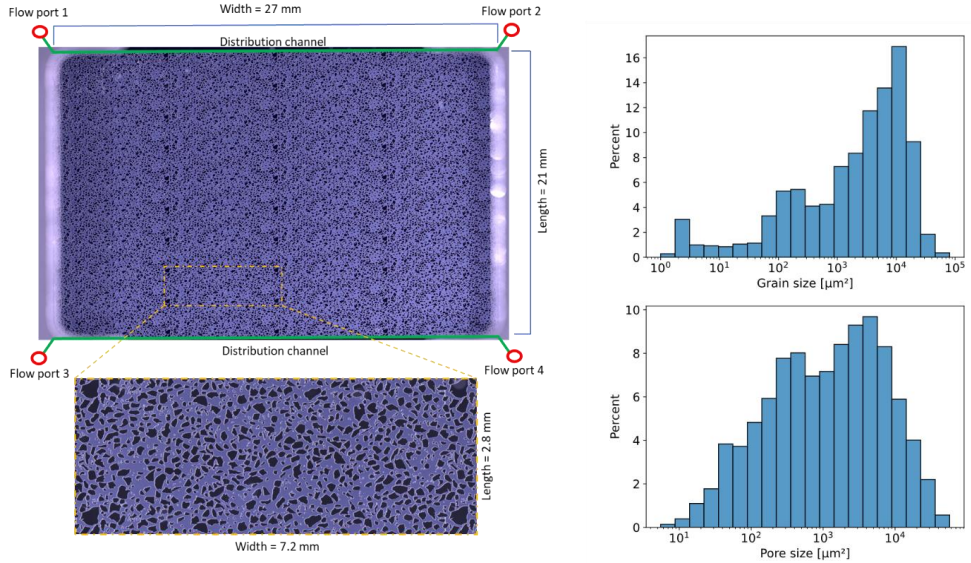


Figure 1: Left: Dimensions of the entire micromodel and the unique pore network with the locations of the fluid flow ports and distribution channels. Right: Characteristic features of the micromodel from one of the 36 repetitions of the pattern where the top graph shows grain sizes and the bottom graph shows pore size distribution. The average grain and pore sizes are 6238 μm^2 and 3896 μm^2 , respectively.

Table 2: Pore network properties

Parameter	Value
Width	27 mm
Length (without channels)	21 mm
Depth	30 μm
Porosity	0.61
Permeability	2.97 Darcy
Average Pore size	3896 μm^2
Unique pore network repetition	36
Pattern size	7.2 mm x 2.8 mm
Tortuosity (x-axis)	1.881
Tortuosity (y-axis)	1.998

The micromodel-holder was designed and manufactured in-house from PEEK and aluminium materials. The first part made of PEEK had four threaded holes in the bottom side that aligned with the micromodel flow ports. The micromodel was placed on the top of the O-rings on the first part, and the second part made of aluminium was attached. The second part had an open window for direct

visualization of the micromodel. Detailed steps for mounting the micromodel in holder with images can be found in [50].

5.3. Experimental setup and procedures

Images of the pore network were acquired using a microscope (Axio Zoom. V16, Zeiss) equipped with both brightfield and fluorescence channels. The brightfield channel used a cold-light source and a diffuser S for uniform illumination, whereas the fluorescence channel used a 38 HE Green fluorescent reflector to track the phase with the fluorescent tracer. A motorized scanning stage enabled high-resolution image acquisition by using 121 tiles (11 x 11). Two images were captured for each tile and then stitched together to obtain images of the whole pore network at two channels (Fluorescence channel image and Brightfield channel image) (Figure 3).

Figure 2 shows a schematic of the experimental setup for visualization of CO₂ foam. The setup was designed to enable high pressure experiments. A back pressure regulator (BPR) was placed at the end of experimental setup connecting with a N₂ cylinder at 100 bars. The select valves used in this setup allow injection and production from all the flow ports, but in this study port 1 was used for CO₂ injection and port 4 was used for production. The switch valve was used to inject incompressible fluids directly into the micromodel using the pump with distilled water as driving force. The cleaning solutions were injected into the 1 mL loop in the switch valve using a syringe, then the switch valve was set to go through the loop, and the solutions were pressurized the same as the system. Prior to inject into the pore network, all aqueous solutions were saturated with liquid CO₂ at experimental conditions, enabling the intensity of fluorescence dye to stay constant when contacting CO₂. Before each experiment the pore network was cleaned with distilled water, 2-propanol-water azeotrope (IPA), and hydrogen peroxide (H₂O₂). H₂O₂ was used to maintain the same surface conditions before each experiment. The CO₂ was in the liquid phase at experimental conditions [51].

Two repetitions of five static CO₂ foam experiments were performed (four with foaming solutions listed in Table 1, and one with only brine for comparison). Investigation of Ostwald ripening mechanism for a static CO₂ foam in porous media at high pressure requires stable CO₂ saturation in the field of view (FoV). The experiments were designed so that the CO₂ saturation was constant throughout the experiment. To achieve this, the following procedure was used:

- i. Pre-saturate the micromodel with the CO₂ saturated solution at a constant volumetric flow rate (2 μL/min) using port 1 for injection and port 4 for production.
- ii. Inject CO₂ at a constant volumetric flow rate (2 μL/min) for 2 hours, to generate foam with high CO₂ saturation and bubble number, using port 1 for injection and port 4 for production.
- iii. Inject the aqueous solution at a constant volumetric flow rate (1 μL/min) to remove the CO₂ bubbles in the distribution channels and isolate foam in the pore network, from port 1 to port 2, and port 3 to port 4 for 1 hour each.
- iv. Hold constant pressure in the micromodel, with the distilled water pump, using port 1 for injection while the production line was closed. T= 0 in the results and discussion section refers to this step, when the distilled water pump is connected to the micromodel.

Despite isolation of the foam, dissolution of CO₂ bubbles into the aqueous phase was observed in the top left side of the micromodel. The dissolution was caused by diffusion at the inlet (port 1). The aqueous phase in the micromodel and inlet lines was pre-saturated with CO₂, but the CO₂ diffused to the distilled water pump used to hold the pressure. Therefore, the dissolved area was removed from the analysed FoV for each experiment.

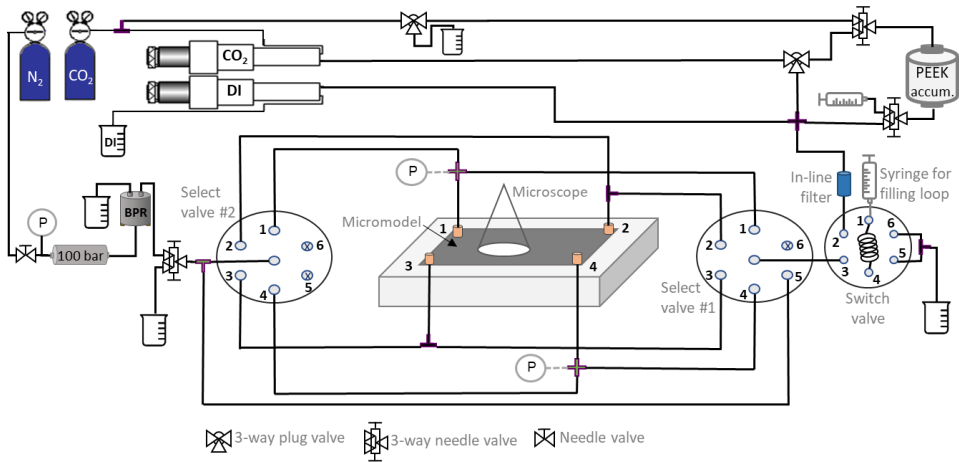


Figure 2: Schematic of the experimental setup used for pore-scale foam studies in the micromodel. The micromodel was assembled in the holder positioned underneath the microscope. The lines were connected to the ports from the bottom side of the holder but are shown at the top in the figure for illustration. A high precision plunger pump (Quizix Q5000-2.5K) was used for fluid injection. The DI cylinder was used for injection of the distilled water or driving the fluids in the loop in the switch valve, whereas CO₂ cylinder was used for CO₂ injection or driving the fluids from the PEEK accumulator. Two 6-ports select valves (IDEX, MXP7970-000) were used, one at inlet (#1) and one at the outlet (#2), to ensure constant dead-volume. In addition, a two-position switch valve (IDEX, 9725) was used to facilitate variable fluid injection without need for additional pumps.

5.4. Image processing and analysis

Image segmentation was conducted to obtain quantitative data for each CO₂ bubble throughout the experiments. Image thresholding is the most challenging task during image processing. It transfers a grayscale image with a range of pixel values into a binary image of two-pixel values, where the first value is the background and the second value is the foreground. In this work, the CO₂ bubble properties need to be analyzed. Therefore, the background was set to consist of the grains and aqueous phase and the foreground consisted of CO₂ bubbles. Cropped images acquired with fluorescence and brightfield channels, and their corresponding grayscale histograms are shown in Figure 3.

The fluorescence and brightfield images were transformed into grayscale to calculate the corresponding grayscale histograms. Then the histograms were used to separate the image into two or three classes using the Multi-Otsu algorithm from scikit-image library [52]. The Multi-Otsu algorithm was used to calculate appropriate thresholding values. The fluorescence channel image was separated into two classes, where each class was in the foreground at this stage. The first class contained grains and CO₂ signals, whereas the second class contained the water phase (fluorescent tracer) (Figure 3a and c). The brightfield channel image was separated into three classes (Figure 3d) following two steps. In the first step, the histogram with values starting at 50 were used to calculate the first threshold value, and the grains were classified as foreground in the first class. In the second step, the histogram was used from the first threshold value to the end of the histogram to calculate the second threshold value. The aqueous phase and CO₂ were classified as a foreground in the second class, whereas the grain edges and lamellae were classified as a foreground in the third class (Figure 3b and d). Subtraction of class 3 (grains) and class 5 (grain edges, and lamellae) obtained from the brightfield image from class 1 (grains and CO₂) obtained from the fluorescence image results in a binary image of separated bubbles and some noise. The morphology function from OpenCV [53] was used with 1 x 3 and 3 x 1 kernels to

remove noise. Figure 3e illustrates the grains, CO₂ bubbles, and the aqueous phase in different colors. The CO₂ saturation is underestimated due to subtraction of thick lamellae and filtration.

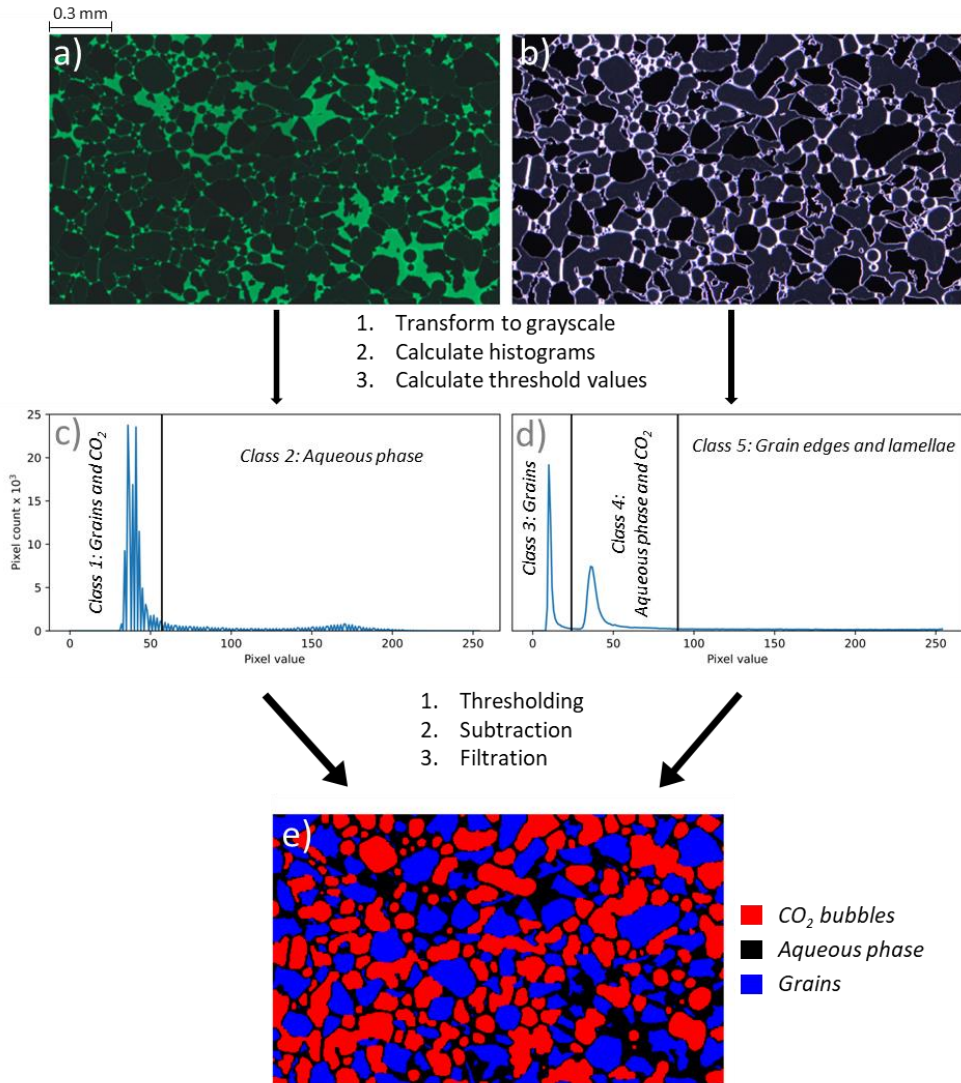


Figure 3: Illustration of the segmentation process. a) Fluorescence channel image (2.2 mm x 1.3 mm) of the micromodel with CO₂ foam and aqueous phase occupying the pores, CO₂ and grains appear black, whereas aqueous phase with fluorescent tracer appears green. b) Brightfield channel image from same size, position, and time as a), grains appear black, aqueous phase and CO₂ appear purple, and grain edges and lamella appear white. c) and d) grayscale image histogram plots corresponding to the images above. The black vertical lines shown in the histogram plots are the thresholding values calculated using the multi-Otsu algorithm [52]. The possible classes to obtain from each channel are shown in the histograms. e) Illustration of results, blue areas represent the grains, red areas are discrete CO₂ bubbles, and black areas are the continuous water phase.

Ostwald ripening occurs due to the diffusion of gas from smaller high-curvature bubbles to larger low-curvature bubbles. Therefore, the bubble shape was described quantitatively using a roundness equation:

$$\text{Roundness} = \frac{4\pi \times \text{Area}}{\text{Perimeter}^2}$$

The roundness equals one for a circular shape and goes down to zero for highly non-circular shapes.

6. Results and discussion

6.1. CO₂ saturation

To separate Ostwald ripening from other effects, it was important that the CO₂ saturation was constant as a function of time (see Figure 4). After an initial increase, the CO₂ saturation for CO₂ foam generated with surfactant-based solutions were constant within experimental uncertainty in the FoV. For CO₂-foam stabilized with nanoparticles, the CO₂ saturation decreased with time because the nanoparticle-based foam consisted of very large CO₂ bubbles that were more exposed to the water phase and gradually dissolved. The CO₂ saturation without foaming agent was constant during the first 30 hours and then decreased because of CO₂ dissolution.

The finely textured surfactant-based foams trapped more CO₂ and showed higher CO₂ saturation (on average 0.50) relative to nanoparticle (0.36) and brine (0.29) that did not generate stable foam and lower CO₂ trapping. Silica nanoparticles are known for stabilizing, rather than generating, foam, and brine did not generate foam due to the lack of a foaming agent [18]. The hybrid nanoparticle-surfactant solution trapped more CO₂ (0.53) compared with pure surfactant-based foam (on average 0.49), and doubling the surfactant concentration (from 2500 to 5000 ppm) increased the CO₂ trapping by two percent PV due to the generation of finer textured foam which may be beneficial for CO₂ storage applications. Previous studies have reported increased oil recovery and CO₂ storage capacity using hybrid nanoparticle-surfactant solution [20, 54, 55].

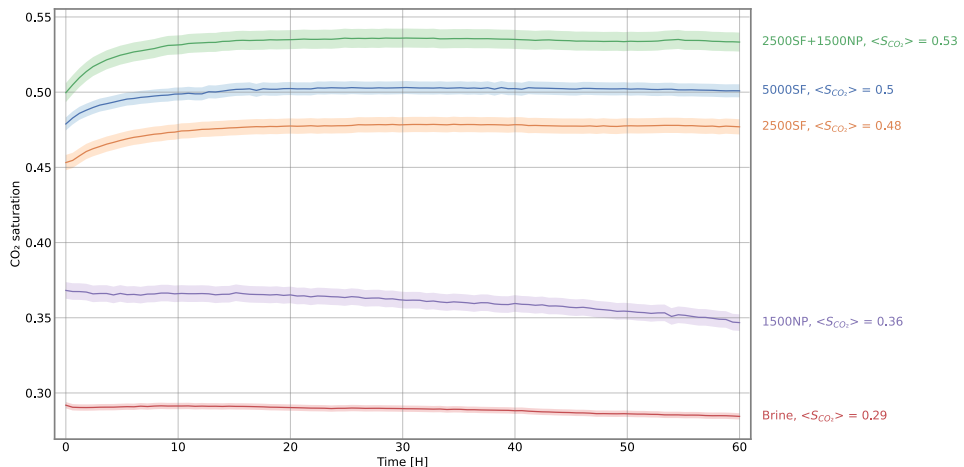


Figure 4: The average CO₂ saturation as a function of time for repeated experiments conducted with foaming solutions and brine, and their corresponding standard deviation (shaded area). The CO₂ saturation for CO₂ foam generated with surfactant-based solutions (green, blue, and orange lines) were constant from 10 hours and throughout the experiments. The increase at the start was due to diffusion of very small bubbles that could not be tracked by image analysis into larger bubbles. The highest CO₂ saturation (53% of pore volume) was achieved using hybrid nanoparticle-surfactant solution (2500SF+1500NP). The

average CO₂ saturation without counting for the first 10 hours for the experiments conducted with surfactant was 0.50, 0.48, 0.53, 0.36 and 0.29 for 5000SF, 2500SF, 2500SF+1500NP, 1500NP and Brine, respectively. The CO₂ saturation for 1500NP decreased with time because nanoparticle-based foam consisted of very large CO₂ bubbles that were more exposed to the aqueous phase and hence dissolved a little.

6.2. Bubble roundness

Ostwald ripening leads to bubble coarsening due to the diffusion of gas from smaller, high-curvature bubbles to larger, low-curvature bubbles (see Figure 5). Pore-level images showed a small bubble (blue circle, Figure 5) being consumed by a larger bubble, with a resulting accumulation of the aqueous phase in the original location of the small bubble. During this process, the roundness of the larger bubbles decreased with time (from on average 0.91, to on average 0.79), hence coarsening occurred. As coarsening ensued, the aqueous phase on top of lamellae was pushed to the top side of the image resulting in less bubble roundness.

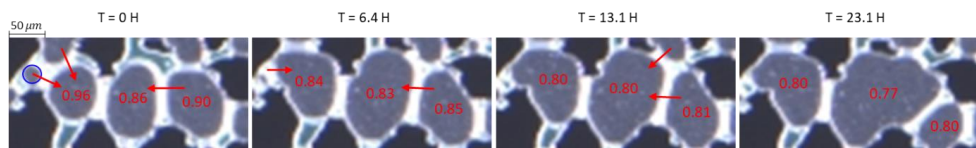


Figure 5: Sequential composed images showing static CO₂ foam. Red arrow shows the direction of CO₂ diffusion. The bubble roundness is indicated by red values inside corresponding bubbles. The images are from 5000SF at the same FoV (0.33 mm x 0.16 mm).

Pore-level foam stability depends on several factors, including bubble roundness, bubble size and the position of lamellae. Typically, high-curvature bubbles have higher energy and are less stable than low-curvature bubbles. The average bubble roundness (Figure 6) was higher using 2500SF foaming solution compared to solutions with higher foaming agent concentration (2500SF + 1500NP, 5000SF), indicating less stable foam at lower concentrations. Previous studies have reported generation of stronger and more stable CO₂ foams at higher surfactant concentrations [56]. The average bubble roundness for surfactant-based foams decreased over time and the rate of change was comparable for all foaming agents. The rate of change in bubble roundness for the three solutions decreased at the start, reaching a minimum after 2 hours, then increased towards zero. The rate of change reached zero after around 30 hours for all three solutions. However, after 40 hours the rate of change for the average roundness increased (Figure 6, inset plot), and resulted in a further decrease in the average roundness because of coarsening. The average roundness approached equilibrium again between 55 and 60 hours. Experiments conducted with only brine or nanoparticles (1500 NP) were excluded because the bubbles were stable, and their roundness did not change with time. The average roundness of bubbles generated with brine and 1500NP was 0.70 and 0.56, respectively.

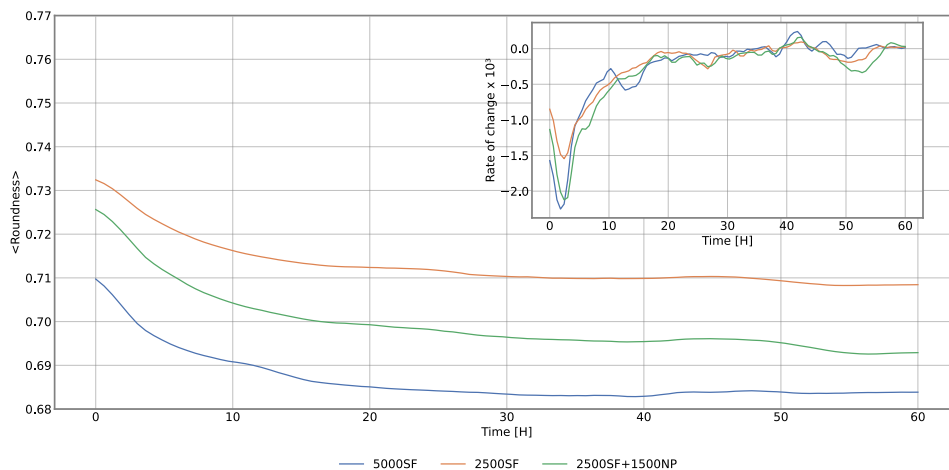


Figure 6: The average roundness for repeated experiments conducted with surfactant and nanoparticles-based solutions (5000SF, 2500SF, and 2500SF+1500NP). The inset plot shows the rates of change in the average bubble roundness. Bubbles generated with 2500SF solution had the most roundness, next was bubbles generated with 2500SF+1500 NP solution, and bubbles generated with 5000SF solution had the least roundness. The overall trend of average roundness is equal for the three solutions. The rate of change reached zero after around 2 hours for all three solutions, and reached equilibrium after 30 hours.

6.3. Coarsening and anti-coarsening of CO₂ foam

Three types of coarsening were observed in this study: 1. large bubbles in open pore network growing at the expense of small bubbles at high aqueous phase saturations (Figure 7); 2. large bubbles growing at the expense of small bubbles, at low aqueous phase saturation, restricted by the grains (Figure 8); and 3. equilibration of plateau borders (Figure 9).

Type 1 coarsening resembles bulk systems, where the largest bubbles with low-curvature grow at the expense of smaller bubbles with high-curvature, unrestricted by the porous media (Figure 7). The presence of foaming agents reduced coarsening, and equilibrium was not achieved even after 60 hours, indicated by the gradual increase of the bubble area (Figure 7). Type 2 coarsening showed that CO₂ bubbles were constricted by the grains, and the aqueous saturation was low compared to type 1 coarsening (Figure 8). Type 2 coarsening was driven by lamella movement towards minimum energy configuration at the pore throats. The number of bubbles decreased, whereas the largest bubble grow (Figure 8). Overall, type 2 coarsening led to the disappearance of small bubbles with high curvature, due to diffusion of CO₂ from smaller bubbles to the larger bubbles, resulting in a system with lower average bubble curvature.

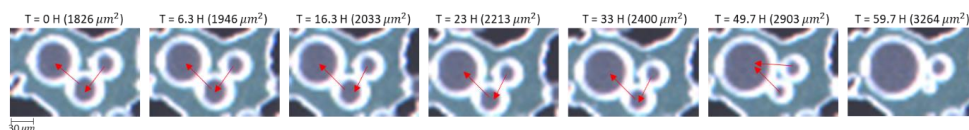


Figure 7: Sequential composed images showing an example of type 1 coarsening of static CO₂ foam. The size of the largest bubble is tracked, and to find next to the time of images. Red arrows show the direction of CO₂ diffusion. The largest bubble with low-curvature grows at the expense of smaller bubbles with high-curvature, unrestricted by the porous media in a high aqueous phase saturation. The images are from 5000SF at the same FoV (0.18 mm x 0.12 mm).

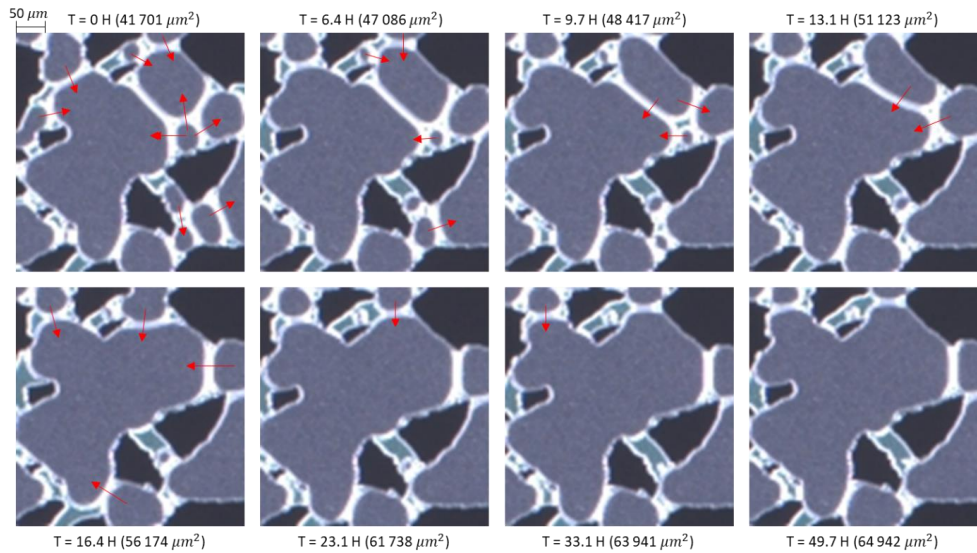


Figure 8: Sequential composed images showing example of type 2 coarsening of static CO_2 foam. The size of the largest bubble is tracked, and to find next to the time of images. Red arrows show the direction of CO_2 diffusion. From 0 to 13.1 hours, the number of arrows decreased from 9 to 2, small bubbles disappeared, and large bubbles grow. The largest bubble moved toward the top right corner in the time interval from 13.1 to 16.4 hours, and this made the water flow from the left bottom to top left, and some lamellae were moved from the minimum energy configuration. This destabilization of lamellae led to further coarsening, and the number of arrows increased to 4. Type 1 coarsening led to the disappear of small bubbles with high curvature, and diffusion of CO_2 from those bubbles to the larger bubbles resulting in a system with lower curvature. Due to the wettability of the micromodel, water accumulation in narrow pores was observed. The images are from 5000SF at the same FoV (0.39 mm x 0.41 mm).

Sequentially composed images of the pore network revealed that most lamellae were in the pore throats at the minimum-energy configuration. However, some lamellae were also found in the middle of the pores if the bubbles were positioned with an equilibrium curvature in relation to each other [31]. Type 3 coarsening occurred when lamellae were in a minimum-energy state positioned in the middle of the pores (Figure 9). A plateau border is where three lamellae are connected. The lamellae can be at minimum energy configuration when the angles for all the interfaces between the bubbles in the plateau border equal 120 degree, even if the lamellae are in the middle of the pore. At time zero in Figure 9, the angles at the plateau border are not 120 degree and that causes the plateau border to reposition and triggering CO_2 diffusion between the bubbles. The plateau border reached equilibrium after 6 hours when all the angles reached 120 degrees. Type 3 coarsening led to stable CO_2 foam states 8 times faster than type 2, and 10 times faster than type 1. In type 3 coarsening, the lamellae are freer to move, without friction with the pore walls, therefore the foam reaches equilibrium faster than type 2 coarsening which had friction from the pore walls. For type 1 coarsening, the aqueous saturation was high, and the CO_2 diffusion was slower due to the thick lamellae and the larger distance between the bubbles.

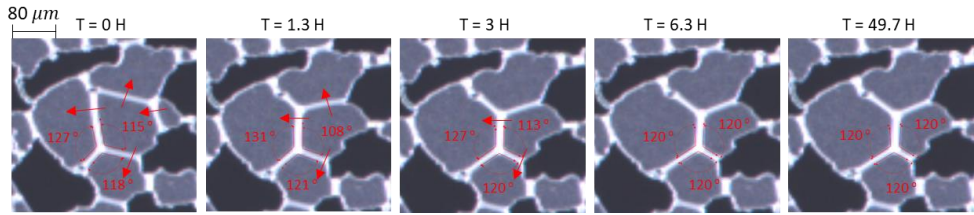


Figure 9: Sequential composed images showing example of type 3 coarsening of static CO_2 foam. Red arrows show the direction of CO_2 diffusion. Plateau border is where three lamellae are connected, the angles are drawn on the plateau border in the bottom of the images. The angles at the start are not 120 degree and that cause the plateau border to reposition, and the CO_2 start to diffuse between the bubbles. This repositioning of the plateau border caused creation of a new plateau border, and caused the disappear of the small bubble in the right of the image because the lamella was pushed toward the pore throat. Type 3 coarsening leads to equilibrium while the lamellae are still in the middle of the pores. The lamellae can be at minimum energy configuration when the angles for all the interfaces between the bubbles in the plateau border equal 120 degree. The images are from 5000SF at the same FoV (0.34 mm x 0.32 mm).

Several studies have reported that diffusion direction can reverse so that CO_2 is transported from large bubbles to small bubbles, a phenomenon called anti-coarsening [31, 32, 40]. We also observed anti-coarsening here (Figure 10); when the system is close to equilibrium (most lamellae at minimum-energy configuration at pore throats), a lamella moves towards the pore throat due to capillary suction and the CO_2 diffuses from large bubble to small bubble; the opposite of Ostwald ripening.

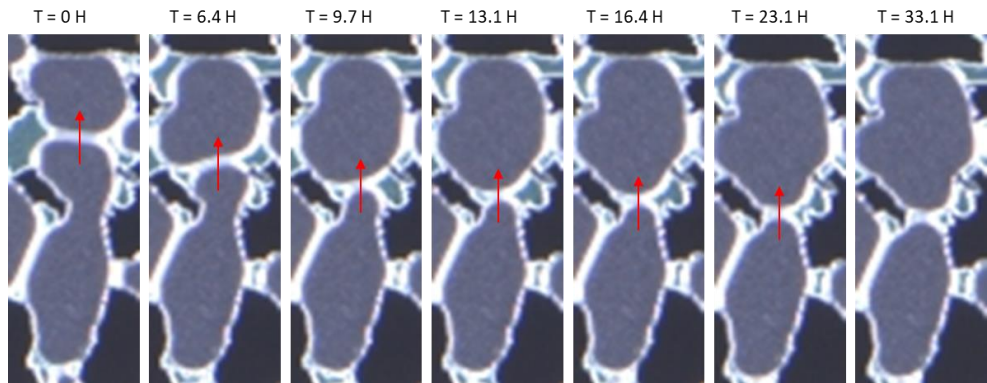


Figure 10: Sequential composed images showing anti-coarsening of static CO_2 foam. CO_2 is transported from the larger bubble to the smaller bubble, and lamella moves from the middle of the top pore to the pore throat in the middle. The images are from 5000SF at the same FoV (0.17 mm x 0.43 mm).

The average bubble area with surfactant-based solutions increased with time due to the Ostwald ripening effect (see Figure 11). The normalized average area increased rapidly in the time interval from 0 to 10 hours compared to the time interval from 10 to 60 hours with a decreasing rate of change (Figure 11, inset plot). The rapid increase at the start was because all coarsening types are trying to reach equilibrium, hence coarsening the CO_2 foam rapidly. After 10 hours, type 3 coarsening was already at equilibrium and the rate of change for type 2 decreased, whereas type 1 coarsening was a very slow process, and almost linear in the experimental time. Anti-coarsening mechanism did not affect the normalized average area because it does not remove bubbles (only repositions lamellae) and the average area remains constant. Bubbles generated with 2500SF solution reached the largest bubble size, followed by bubbles generated with 2500SF+1500 NP solution, and bubbles generated with 5000SF solution. Doubling the surfactant concentration from 2500 ppm to 5000 ppm resulted in stronger foam indicated by lower normalized average area, which resisted Ostwald ripening. Adding

1500 ppm of nanoparticles to the 2500 ppm surfactant-based solution resulted in stronger foam also, but the rate of destabilization at time interval from 0 to 10 hours was higher. Experiments conducted with only brine or nanoparticles (1500 NP) were not included in the analysis because their normalized average area did not change with time. The average normalized average bubble area with brine and 1500NP was 17.2 and 3.2, respectively.

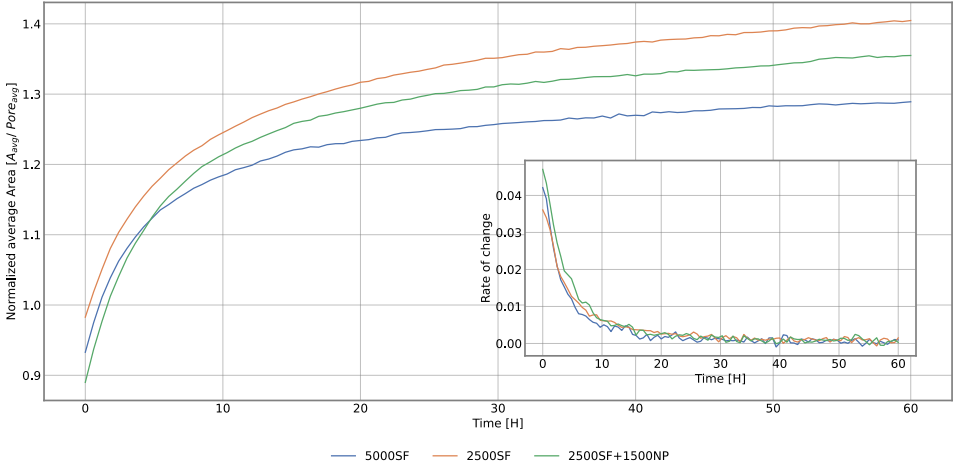


Figure 11: The normalized average area for repeated experiments conducted with surfactant and nanoparticles-based solutions (5000SF, 2500SF, and 2500SF+1500NP). The rates of change in the normalized average area are plotted as inset plot. Bubbles generated with 2500SF solution reached the highest bubble size, followed by bubbles generated with 2500SF+1500 NP solution, and bubbles generated with 5000SF solution.

7. Conclusion

This work studied the Ostwald ripening mechanism for static CO₂ foams generated with different foaming solutions in a realistic pore structure at reservoir pressure. Ostwald ripening was the dominant mechanism of foam destabilization. Sequentially composed images of the pore network revealed gas diffusion from small, high-curvature bubbles to large, low-curvature bubbles, and the overall curvature of the bubbles decreased with time. We have observed three types of coarsening. The first coarsening type was characterized by large bubbles growing at the expense of small bubbles, at high aqueous phase saturations, unrestricted by the grains. The second coarsening type was characterized by large bubbles growing at the expense of small bubbles, at low aqueous phase saturation, restricted by the grains. The third coarsening type was characterized by equilibration of plateau borders. We observed anti-coarsening phenomena, where CO₂ diffused from a large bubble to a small bubble. The experimental results also compared CO₂ foam generated by hybrid nanoparticle-surfactant foaming solution to CO₂ foam stabilized by only surfactant or nanoparticles. The foam generated with surfactant-based solutions achieved the highest CO₂ saturation compared to solutions with only nanoparticles or brine. Doubling the surfactant concentration from 2500 ppm to 5000 ppm and adding 1500 ppm of nanoparticles to the 2500 ppm surfactant-based solution resulted in stronger foam, which resisted Ostwald ripening.

8. Data availability

The raw foam injection micromodel images and python scripts are available from the corresponding author on reasonable request.

9. Declaration of Competing Interest

The authors declare that they have no known competing financial interests or personal relationships that could have appeared to influence the work reported in this paper.

10. Acknowledgement

The authors wish to acknowledge the Research Council of Norway for financial support (project no. 294886 and 301201) for funding of PhD candidates Benyamine Benali and Aleksandra Sæle and Dr. Zachary Paul Alcorn.

11. References

1. Ipcc, 2014: Climate Change 2014: Mitigation of Climate Change. Contribution of Working Group Iii to the Fifth Assessment, Report of the Intergovernmental Panel on Climate Change [Edenhofer, O., R. Pichs-Madruga, Y. Sokona, E. Farahani, S. Kadner, K. Seyboth, A. Adler, I. Baum, S. Brunner, P. Eickemeier, B. Kriemann, J. Savolainen, S. Schlömer, C. Von Stechow, T. Zwickel and J.C., and Minx (Eds.)]. Cambridge University Press, Cambridge, United Kingdom and New York, Ny, USA.
2. Metz, Bert, Davidson, Ogunlade, De Coninck, Hc, Loos, Manuela, and Meyer, Leo, *IPCC special report on carbon dioxide capture and storage*. 2005: Cambridge: Cambridge University Press.
3. Eiken, Ola, Ringrose, Philip, Hermanrud, Christian, Nazarian, Bamshad, Torp, Tore A., and Høier, Lars, *Lessons learned from 14 years of CCS operations: Sleipner, In Salah and Snøhvit*. Energy Procedia, 2011. **4**: p. 5541-5548.
4. Taber, J. J., Martin, F. D., and Seright, R. S., *EOR Screening Criteria Revisited— Part 1: Introduction to Screening Criteria and Enhanced Recovery Field Projects*. SPE Reservoir Engineering, 1997. **12**(03): p. 189-198.
5. Hanssen, J.E., Holt, Torleif, and Surguchev, L.M. *Foam Processes: An Assessment of Their Potential in North Sea Reservoirs Based on a Critical Evaluation of Current Field Experience*. in *SPE/DOE Improved Oil Recovery Symposium*. 1994.
6. Talebian, Seyedeh Hosna, Masoudi, Rahim, Tan, Isa Mohd, and Zitha, Pacelli Lidio Jose, *Foam assisted CO₂-EOR: A review of concept, challenges, and future prospects*. Journal of Petroleum Science and Engineering, 2014. **120**: p. 202-215.
7. Mo, Di, Yu, Jianjia, Liu, Ning, and Lee, Robert. *Study of the Effect of Different Factors on Nanoparticle-Stabilized CO₂ Foam for Mobility Control*. in *SPE Annual Technical Conference and Exhibition*. 2012.
8. Alcorn, Zachary Paul, Fredriksen, Sunniva B., Sharma, Mohan, Føyen, Tore, Wergeland, Connie, Fernø, Martin A., Graue, Arne, and Ersland, Geir, *Core-scale sensitivity study of CO₂ foam injection strategies for mobility control, enhanced oil recovery, and CO₂ storage*. E3S Web Conf., 2020. **146**: p. 02002.
9. Lake, Larry, Johns, Russell T., Rossen, William R., and Pope, Gary A., *Fundamentals of Enhanced Oil Recovery*. Society of Petroleum Engineers.
10. Rossen, Wr, *Foams in Enhanced Oil Recovery. Foams—Theory, Measurement, and Applications, RK Prud'homme and SA Khan ed., 413-464*. 1996, New York: Marcel Dekker Inc.
11. Sæle, Aleksandra, Graue, Arne, and Alcorn, Zachary, *Unsteady-state CO₂ foam injection for increasing enhanced oil recovery and carbon storage potential*. ADVANCES IN GEO-ENERGY RESEARCH, 2022. **6**: p. 472-481.
12. Enick, Robert Michael, Olsen, D, Ammer, J, and Schuller, William. *Mobility and conformance control for CO₂ EOR via thickeners, foams, and gels—a literature review of 40 years of research and pilot tests*. in *SPE improved oil recovery symposium*. 2012. OnePetro.
13. Føyen, T, Brattækås, Bergit, Fernø, Ma, Barrabino, Albert, and Holt, Torleif, *Increased CO₂ storage capacity using CO₂-foam*. International Journal of Greenhouse Gas Control, 2020. **96**: p. 103016.
14. David, Amiel and Marsden, Sullivan S. *The rheology of foam*. in *Fall Meeting of the Society of Petroleum Engineers of AIME*. 1969. OnePetro.
15. Shan, D. and Rossen, W. R., *Optimal Injection Strategies for Foam IOR*. SPE Journal, 2004. **9**(02): p. 132-150.
16. Sheng, James J., *Chapter 11 - Foams and Their Applications in Enhancing Oil Recovery, in Enhanced Oil Recovery Field Case Studies*, J.J. Sheng, Editor. 2013, Gulf Professional Publishing: Boston. p. 251-280.
17. Eide, Øyvind, Føyen, Tore, Skjelsvik, Eldri, Rognmo, Arthur, and Fernø, Martin. *Nanoparticle Stabilized Foam in Harsh Conditions for CO₂ EOR*. in *Abu Dhabi International Petroleum Exhibition & Conference*. 2018.

18. Alcorn, Zachary Paul, Føyen, Tore, Gautepllass, Jarand, Benali, Benyamine, Soyke, Aleksandra, and Fernø, Martin, *Pore- and Core-Scale Insights of Nanoparticle-Stabilized Foam for CO₂-Enhanced Oil Recovery*. *Nanomaterials*, 2020. **10**(10): p. 1917.
19. Soyke, A., Benali, B., Føyen, T., and Alcorn, Z.P., *Hybrid Nanoparticle-Surfactant Stabilized Foams for CO₂ Mobility Control at Elevated Salinities*. 2021. **2021**(1): p. 1-14.
20. Chaturvedi, Krishna Raghav and Sharma, Tushar, *In-situ formulation of pickering CO₂ foam for enhanced oil recovery and improved carbon storage in sandstone formation*. *Chemical Engineering Science*, 2021. **235**: p. 116484.
21. Singh, Robin and Mohanty, Kishore K., *Foams Stabilized by In-Situ Surface-Activated Nanoparticles in Bulk and Porous Media*. *SPE Journal*, 2016. **21**(01): p. 121-130.
22. Farajzadeh, R., Andrianov, A., Krastev, R., Hirasaki, G. J., and Rossen, W. R., *Foam–oil interaction in porous media: Implications for foam assisted enhanced oil recovery*. *Advances in Colloid and Interface Science*, 2012. **183-184**: p. 1-13.
23. Aronson, A. S., Bergeron, V., Fagan, M. E., and Radke, C. J., *The influence of disjoining pressure on foam stability and flow in porous media*. *Colloids and Surfaces A: Physicochemical and Engineering Aspects*, 1994. **83**(2): p. 109-120.
24. Kovscek, Anthony R and Radke, Clayton J, *Fundamentals of foam transport in porous media*. 1993, Lawrence Berkeley Lab., CA (United States).
25. Langevin, Dominique, *Coalescence in foams and emulsions: Similarities and differences*. *Current Opinion in Colloid & Interface Science*, 2019. **44**: p. 23-31.
26. Benali, Benyamine, Føyen, Tore L., Alcorn, Zachary Paul, Haugen, Malin, Gautepllass, Jarand, Kovscek, Anthony R., and Fernø, Martin A., *Pore-scale bubble population dynamics of CO₂-foam at reservoir pressure*. *International Journal of Greenhouse Gas Control*, 2022. **114**: p. 103607.
27. Yekeen, Nurudeen, Idris, Ahmad Kamal, Manan, Muhammad A., Samin, Ali Mohamed, Risal, Abdul Rahim, and Kun, Tan Xin, *Bulk and bubble-scale experimental studies of influence of nanoparticles on foam stability*. *Chinese Journal of Chemical Engineering*, 2017. **25**(3): p. 347-357.
28. Yu, Wei and Kanj, Mazen Y., *Review of foam stability in porous media: The effect of coarsening*. *Journal of Petroleum Science and Engineering*, 2022. **208**: p. 109698.
29. Kornev, Konstantin G., Neimark, Alexander V., and Rozhkov, Aleksey N., *Foam in porous media: thermodynamic and hydrodynamic peculiarities*. *Advances in Colloid and Interface Science*, 1999. **82**(1): p. 127-187.
30. Osei-Bonsu, Kofi, Grassia, Paul, and Shokri, Nima, *Relationship between bulk foam stability, surfactant formulation and oil displacement efficiency in porous media*. *Fuel*, 2017. **203**: p. 403-410.
31. Yu, Wei, Zhou, Xianmin, and Kanj, Mazen Yousef, *Microfluidic Investigation of Foam Coarsening Dynamics in Porous Media at High-Pressure and High-Temperature Conditions*. *Langmuir*, 2022. **38**(9): p. 2895-2905.
32. Huang, Zhandong, Su, Meng, Yang, Qiang, Li, Zheng, Chen, Shuoran, Li, Yifan, Zhou, Xue, Li, Fengyu, and Song, Yanlin, *A general patterning approach by manipulating the evolution of two-dimensional liquid foams*. *Nature Communications*, 2017. **8**(1): p. 14110.
33. Greenwood, Gw, *The growth of dispersed precipitates in solutions*. *Acta metallurgica*, 1956. **4**(3): p. 243-248.
34. Lifshitz, Ilya M and Slyozov, Vitaly V, *The kinetics of precipitation from supersaturated solid solutions*. *Journal of physics and chemistry of solids*, 1961. **19**(1-2): p. 35-50.
35. Voorhees, Peter W, *The theory of Ostwald ripening*. *Journal of Statistical Physics*, 1985. **38**(1): p. 231-252.
36. Voorhees, Peter Willis, *Ostwald ripening of two-phase mixtures*. *Annual Review of Materials Science*, 1992. **22**(1): p. 197-215.
37. Saint-Jalmes, Arnaud, *Physical chemistry in foam drainage and coarsening*. *Soft Matter*, 2006. **2**(10): p. 836-849.

38. Marchalot, Julien, Lambert, Jérôme, Cantat, Isabelle, Tabeling, Patrick, and Jullien, M-C, *2D foam coarsening in a microfluidic system*. EPL (Europhysics Letters), 2008. **83**(6): p. 64006.
39. Xu, Ke, Mehmani, Yashar, Shang, Luoran, and Xiong, Qingrong, *Gravity-Induced Bubble Ripening in Porous Media and Its Impact on Capillary Trapping Stability*. Geophysical Research Letters, 2019. **46**(23): p. 13804-13813.
40. Xu, Ke, Bonnecaze, Roger, and Balhoff, Matthew, *Egalitarianism among bubbles in porous media: an ostwald ripening derived anticoarsening phenomenon*. Physical review letters, 2017. **119**(26): p. 264502.
41. Wang, Chuanxi, Mehmani, Yashar, and Xu, Ke, *Capillary equilibrium of bubbles in porous media*. Proceedings of the National Academy of Sciences, 2021. **118**(17): p. e2024069118.
42. Jones, S. A., Getrouw, N., and Vincent-Bonnieu, S., *Foam flow in a model porous medium: I. The effect of foam coarsening*. Soft Matter, 2018. **14**(18): p. 3490-3496.
43. Mehmani, Yashar and Xu, Ke, *Pore-network modeling of Ostwald ripening in porous media: How do trapped bubbles equilibrate?* Journal of Computational Physics, 2022. **457**: p. 111041.
44. Gogoi, Sekhar and Gogoi, Subrata Borgohain, *Review on microfluidic studies for EOR application*. Journal of Petroleum Exploration and Production Technology, 2019. **9**(3): p. 2263-2277.
45. Gizzatov, Ayrat, Pierobon, Scott, Alyousef, Zuhair, Jian, Guoqing, Fan, Xingyu, Abedini, Ali, and Abdel-Fattah, Amr I., *High-temperature high-pressure microfluidic system for rapid screening of supercritical CO₂ foaming agents*. Scientific Reports, 2021. **11**(1): p. 3360.
46. Rogmo, Arthur Uno, Fredriksen, Sunniva Brudvik, Alcorn, Zachary Paul, Sharma, Mohan, Føyen, Tore, Eide, Øyvind, Graue, Arne, and Fernø, Martin, *Pore-to-Core EOR Upscaling for CO₂ Foam for CCUS*. SPE Journal, 2019. **24**(06): p. 2793-2803.
47. Buchgraber, M., Al-Dossary, M., Ross, C. M., and Kovscek, A. R., *Creation of a dual-porosity micromodel for pore-level visualization of multiphase flow*. Journal of Petroleum Science and Engineering, 2012. **86-87**: p. 27-38.
48. Benali, Benyamine, *Quantitative Pore-Scale Analysis of CO₂ Foam for CCUS*. 2019, The University of Bergen.
49. Gostick, Jeff T, Khan, Zohaib A, Tranter, Thomas G, Kok, Matthew Dr, Agnaou, Mehrez, Sadeghi, Mohammadamin, and Jervis, Rhodri, *PoreSpy: A python toolkit for quantitative analysis of porous media images*. Journal of Open Source Software, 2019. **4**(37): p. 1296.
50. Haugen, Malin, Benali, Benyamine, Føyen, Tore, Song, Wen, Fernø, Martin A., and Brattekkås, Bergit, *Calcite-functionalized micromodels for pore-scale investigations of CO₂ storage security*. E3S Web Conf., 2023. **366**: p. 01004.
51. Eric W. Lemmon, Ian H. Bell, Marcia L. Huber, and Mark O. McLinden, *Thermophysical properties of fluid systems*. NIST Chemistry WebBook, NIST Standard Reference Database Number 69, Eds. P.J. Linstrom and W.G. Mallard, National Institute of Standards and Technology, Gaithersburg MD, 20899, <https://doi.org/10.18434/T4D303>, (retrieved February 15, 2023).
52. Van Der Walt, Stefan, Schönberger, Johannes L, Nunez-Iglesias, Juan, Boulogne, François, Warner, Joshua D, Yager, Neil, Gouillart, Emmanuelle, and Yu, Tony, *scikit-image: image processing in Python*. PeerJ, 2014. **2**: p. e453.
53. Bradski, Gary, *The openCV library*. Dr. Dobb's Journal: Software Tools for the Professional Programmer, 2000. **25**(11): p. 120-123.
54. Worthen, Andrew J., Parikh, Parth S., Chen, Yunshen, Bryant, Steven L., Huh, Chun, and Johnston, Keith P., *Carbon Dioxide-in-Water Foams Stabilized with a Mixture of Nanoparticles and Surfactant for CO₂ Storage and Utilization Applications*. Energy Procedia, 2014. **63**: p. 7929-7938.
55. Alyousef, Zuhair, Almobarky, Mohammed, and Schechter, David. *Surfactant and a Mixture of Surfactant and Nanoparticles Stabilized-CO₂/Brine Foam for Gas Mobility Control and Enhance Oil Recovery*. in *Carbon Management Technology Conference*. 2017.

56. Phukan, Ranjan, Gogoi, Subrata Borgohain, and Tiwari, Pankaj, *Effects of CO₂-foam stability, interfacial tension and surfactant adsorption on oil recovery by alkaline-surfactant-alternated-gas/CO₂ flooding*. *Colloids and Surfaces A: Physicochemical and Engineering Aspects*, 2020. **597**: p. 124799.

Paper 4

Original article

Unsteady-state CO₂ foam injection for increasing enhanced oil recovery and carbon storage potential

Aleksandra Sæle^{✉*}, Arne Graue, Zachary Paul Alcorn

Department of Physics and Technology, University of Bergen, Bergen, Norway

Keywords:

CO₂ foam
unsteady-state injection
mobility control
carbon storage potential

Cited as:

Sæle, A., Graue, A., Alcorn, Z. P. Unsteady-state CO₂ foam injection for increasing enhanced oil recovery and carbon storage potential. *Advances in Geo-Energy Research*, 2022, 6(6): 472-481.

<https://doi.org/10.46690/ager.2022.06.04>

Abstract:

The efficiency of CO₂ injection for enhanced oil recovery and carbon storage is limited by severe viscosity and density differences between CO₂ and reservoir fluids and reservoir heterogeneity. In-situ generation of CO₂ foam can improve the mobility ratio to increase oil displacement and CO₂ storage capacity in geological formations. The aim of this work was to investigate the ability of CO₂ foam to increase oil production and associated CO₂ storage potential, compared to other CO₂ injection methods, in experiments that deploy field-scale injection strategies. Additionally, the effect of oil on CO₂ foam generation and stability was investigated. Three different injection strategies were implemented in the CO₂ enhanced oil recovery and associated CO₂ storage experiments: pure CO₂ injection, water-alternating-gas and surfactant-alternating-gas. Foam generation during surfactant-alternating-gas experiments showed reduced CO₂ mobility compared to water-alternating-gas and pure CO₂ injections indicated by the increase in apparent viscosity. CO₂ foam increased oil recovery by 50% compared to pure CO₂ injection and 25% compared to water-alternating-gas. In addition, CO₂ storage capacity increased from 12% during pure CO₂ injection up to 70% during surfactant-alternating-gas injections. Experiments performed at high oil saturations revealed a delay in foam generation until a critical oil saturation of 30% was reached. Oil/water emulsions in addition to CO₂ foam generation contributed to CO₂ mobility reduction resulting in increased CO₂ storage capacity with foam.

1. Introduction

Carbon capture, utilization, and storage (CCUS) is an important contributor to the ongoing transition to a net-zero carbon emission society. In the context of this work, CCUS involves capturing anthropogenic CO₂ from point sources and injecting it into geological formations for energy production and permanent storage (IPCC, 2005). Injection of CO₂ for enhanced oil recovery (EOR) has been performed for over 50 years with commercial success. CO₂ is an excellent solvent for EOR because, at typical reservoir conditions, it is miscible with most of crude oils and may swell the oil, reduce its viscosity and the interfacial tension between oil and water, which all contribute to increased oil recovery (Lee and Kam, 2013). Although utilization of CO₂ for EOR has several benefits there are disadvantages associated with the

density and viscosity differences between the injected CO₂ and reservoir fluids. Common challenges are gravity override, viscous fingering and early gas breakthrough which result in reduced oil recovery and lower carbon storage capacity (Lake et al., 2014). These challenges can be mitigated by reducing CO₂ mobility (Hanssen et al., 1994; Enick et al., 2012).

Common CO₂ mobility control methods include water-alternating-gas (WAG), foams and polymers (Enick et al., 2012). WAG is a method where water and a gas are injected into the porous media in alternating slugs. During WAG injection, the water slugs reduce the relative permeability of the gas to increase volumetric sweep efficiency. WAG will therefore provide CO₂ mobility control by reducing the effect of viscous fingering and early gas breakthrough (Christensen et al., 2001; Massarweh and Abushaikha, 2021). Gravity override can still be a challenge because of density and viscosity diffe-

Table 1. Core properties.

Properties	SS1	SS2
Length (cm)	16.05 ± 0.01	15.55 ± 0.01
Diameter (cm)	3.87 ± 0.01	3.89 ± 0.01
Pore Volume (ml)	41.99 ± 0.01	41.14 ± 0.01
Porosity (%)	22.24 ± 0.05	22.29 ± 0.05
Permeability (D)	2.26 ± 0.03	2.47 ± 0.02
Experiments	Foam quality rate scans	EOR

rences between the injected gas and fluids in the reservoir. The injected CO₂ can be foamed to increase the viscosity of CO₂ and prevent flow instabilities (Rossen, 1996; Skauge et al., 2002; Talebian et al., 2014).

Foam is a colloidal dispersion where gas is dispersed in continuous liquid films called lamellae (Falls et al., 1989; Tadros, 2017). Lamellae are thermodynamically unstable but can be stabilized by a foaming agent, most commonly a surfactant (Schramm, 1994). Foam increases the viscosity of CO₂, thereby reducing CO₂ mobility and improving displacement (Talebian et al., 2014). The efficiency of CO₂ foam for combined EOR and CO₂ storage strongly depends on foam strength and stability, which is influenced by the presence of oil. Several studies report that oil can hinder foam generation and can destabilize foam by spontaneously spreading on the liquid films, resulting in an unstable oil film and bubble coalescence (Ross and McBain, 1944). Others report generation of oil/water emulsions in addition to foam, which increases the capillary number and is beneficial for oil recovery (Amimoshiri et al., 2018; Alcorn et al., 2020). The effect of oil on foam is an area under active investigation.

CO₂ foam is generated in-situ by injecting CO₂ and a foaming solution, either simultaneously (co-injection) or by injecting alternating slugs of foaming solution and CO₂ surfactant-alternating-gas (SAG) (Farajzadeh et al., 2012). At laboratory scale, co-injection is the most common injection strategy because of the ability to achieve steady-state for deriving foam model parameters. Co-injection can be difficult to implement at field-scale because of operational limitations (Hoefner and Evans, 1995). Extremely low injectivities, rapid pressure increases, and challenges associated with downhole corrosion are some of challenges that has led to most field tests using SAG as the injection strategy (Chou et al., 1992; Hoefner and Evans, 1995; Shan and Rossen, 2004).

Few attempts have been made to characterize unsteady-state in-situ CO₂ foam behavior during injection of alternating slugs. Therefore, this study aims to establish a knowledge base and procedure for investigating core-scale CO₂ foam injection strategies for EOR and CO₂ storage. The primary objective was to reduce CO₂ mobility, through the generation of foam, in experiments that are representative of field-scale injection strategies. Three different CO₂ injection strategies were implemented and compared based upon their impact on oil recovery and CO₂ storage. A secondary objective was to investigate the effect of oil on CO₂ foam generation and

stability.

2. Materials and experimental set-up

2.1 Core material

The experiments were performed on two outcrop Bentheimer core plugs with similar properties (Table 1). Bentheimer is a water-wet, homogenous sandstone consisting mainly of quartz, feldspar and clay (Peksa et al., 2015). Sandstone reservoirs are the most common reservoir type in the world and are good candidates for CO₂ storage (Bjørlykke, 2010). Before the experiments the core plugs were cut to the desired length, cleaned, and dried at 60 °C for 72 hours. Then the core plugs were fully saturated with brine under vacuum. The porosity and pore volume of the core plugs were calculated based on weight difference between a dry and a fully saturated core. Absolute brine permeability was measured using Darcy's law for three different injection rates. The core properties are shown in Table 1.

2.2 Fluids

Table 2 shows the fluid properties. Brine consisting of 3.5 wt% NaCl was used for saturation of the core plugs and for waterfloods. To generate CO₂ foam, a nonionic water-soluble surfactant (Surfonic L24-22, Huntsman, TX, USA) was used as the foaming agent. This surfactant was previously tested at core- and field-scale and has shown promising effect on CO₂ mobility reduction (Alcorn et al., 2020a, 2020b). The surfactant was dissolved in brine to make foaming solutions with desired concentrations (Table 2). Both concentrations were above the critical micelle concentration of the surfactant (Sharma, 2019). EOR experiments were performed at first-contact miscible conditions using a mineral oil, n-Decane as the oleic phase. The core plugs were cleaned between each experiment using 2-propanol-water-azetropo (IPA).

2.3 Experimental set-up

The core plug was wrapped in a nickel foil to reduce radial CO₂ diffusion into the surrounding Viton rubber sleeve. The core was mounted in a vertically positioned biaxial Hassler core holder and placed in a heating cabinet. The experimental conditions were 40 °C and 180 bar with an overburden pressure of 240 bar. At these conditions CO₂ is supercritical and miscible with n-Decane. The pressure in the system was maintained by two Equilibar back pressure regulators connected in series to reduce pressure fluctuations. The confinement pressure was controlled using an ISCO pump and the fluids were injected using three different Quizix pumps (Fig. 1). A differential pressure transducer and two absolute pressure transducers were used to measure and control the pressure response. The produced fluids were depressurized and collected at atmospheric conditions. The liquids were collected in a glass cylinder and CO₂ was vented out through an adsorption column. Volume and mass of the produced liquids were measured, and material balance was used to calculate fluid saturation in the core and to estimate the amount CO₂ stored in the core.

Table 2. Fluid properties.

Fluids	Composition
Brine	3.5 wt% NaCl
Foaming solutions	0.25 wt% Surfonic L24-22, Brine 0.50 wt% Surfonic L24-22, Brine
Oil	n-Decane, C ₁₀ H ₂₂
CO ₂	> 99.99% CO ₂
IPA	87.7 wt% 2-propanol

3. Methods

3.1 Foam quality and rate scans

Foam strength and stability is impacted by foam quality and injection rate (Chang and Grigg, 1999). Steady state co-injections of CO₂ and foaming solution were performed as gravity stable assisted injection from top to determine the optimal gas fraction and injection rate that will generate foam with the highest apparent viscosity. Foam quality scans were performed with a drainage-like co-injection with increasing gas fraction (fg). The superficial velocity was constant during foam quality scans (2 and 4 ft/day) and the gas fraction monotonically increased from 0.3 to 1.0. The core plug was saturated with brine before the injections started. Each gas fraction was held constant until steady state was obtained. Apparent viscosity was calculated at steady state for each gas fraction. The gas fraction at which apparent viscosity was highest was used for rate scans. Foam apparent viscosity (μ_{app}) was calculated based on the differential pressure and is defined as:

$$\mu_{app} = \frac{k}{\mu_g + \mu_l} \nabla p \quad (1)$$

where k is the absolute permeability of the core, μ_g and μ_l are respectively gas and liquid superficial velocities, and ∇p is the pressure gradient across the core (Jones et al., 2016). A higher apparent viscosity corresponds to stronger foam.

Rate scans were also performed to determine the influence of injection rate on foam strength and stability. During rate scans, CO₂ and foaming solution were co-injected at constant foam quality, as determined from the quality scan, with increasing superficial velocity from 2 to 12 ft/day. Each rate was held constant until steady state was obtained. An optimal velocity was chosen based on the apparent viscosity results.

3.2 Injection strategies

Three different injection strategies were implemented in the CO₂ EOR and associated CO₂ storage experiments: pure CO₂ injection, WAG and SAG. For all experiments the core plug was 100% saturated with brine before primary drainage with oil until a water saturation between 0.30 and 0.40 was reached. After drainage, the core plug was flooded with water or foaming solution to obtain a residual oil saturation of approximately 0.30. For some experiments the core was not waterflooded and WAG and SAG was implemented directly

after drainage. Fig. 2 shows the injection schemes used during EOR experiments. Each experiment was performed at least twice and the procedures are described below.

(i) Pure CO₂ Injection

During pure CO₂ injection, supercritical CO₂ was injected into the core at a superficial velocity of 4 ft/day. The injection lasted for a total of 8 to 10 pore volumes injected. Two types of experiments were performed: CO₂ injection after waterflood and CO₂ injection after injection of foaming solution (Fig. 2). Differential pressure and fluid production were measured during the experiments.

(ii) WAG and SAG

During WAG and SAG, 18 cycles (approximately 3.5 Pore Volume (PV) injected) of brine or foaming solution and CO₂ were injected (Fig. 2). Each cycle consisted of one brine or foaming solution slug and one CO₂ slug. The volumetric ratio between the slugs was 0.60 to achieve the desired gas fraction as determined from the foam quality scans. After completing the WAG and SAG cycles, pure CO₂ was injected for additional 5 to 6 pore volumes to study the dry out effect, a phenomenon where foam collapses as a result of low foaming solution saturation and high gas fraction. Superficial velocity during WAG and SAG injections was 4 ft/day. Two different foaming solution concentrations were tested during SAGs. The experiments were conducted after waterflood (Fig. 2(a)) and after drainage (Fig. 2(b)).

3.3 CO₂ storage capacity estimation

The CO₂ storage capacity was defined as the fraction of pore volume available for storing CO₂. During the experiments, the volume and mass of produced liquids was precisely measured and the CO₂ storage potential was calculated using the equation below:

$$\text{CO}_2 \text{ storage potential (\%)} = \frac{V_{o,p} + V_{w,p} - V_{w,i}}{V_p} \times 100\% \quad (2)$$

where $V_{o,p}$, $V_{w,p}$, $V_{w,i}$ are respectively volume of oil produced, volume of water, and volume of water injected; V_p is pore volume of the core plug. The volume of CO₂ dissolved in water- and oil-phase was not included in the estimations.

4. Results and discussion

4.1 Foam quality and rate scans

Fig. 3 shows apparent viscosity as a function of gas fraction during co-injections at 2 ft/day (a) and 4 ft/day (b). Two different velocities were tested to investigate the effect of superficial velocity on foam strength. Foam was generated at the lowest gas fraction (0.30) indicated by high apparent viscosity compared to no foam experiment (Fig. 3(a), black dots). Foam apparent viscosity increased until a peak at gas fraction between 0.50 and 0.60. Beyond this point, foam strength decreased as the gas fraction increased because foam texture became coarser when a limiting capillary pressure was reached (Khatib et al., 1988; Farajzadeh et al., 2015). Previous researchers have observed an increase in the optimal gas fraction with increasing velocity (Osterloh and Jante, 1992; Alvarez et al., 2001). However, this behavior was not observed

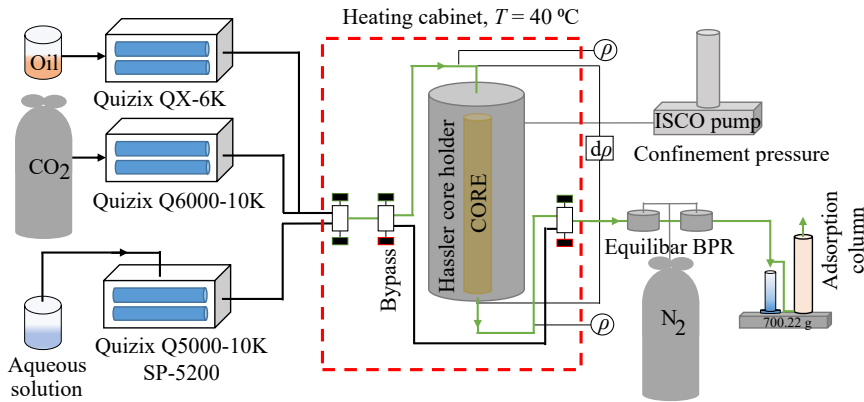


Fig. 1. Experimental set-up. Brine saturated core plug was mounted inside a core holder in a heating cabinet. Green lines represent fluid flow during the experiment. Two back pressure regulators connected in series maintained desired system pressure. A differential pressure transducer and two absolute pressure transducers were used to control and measure the pressure response. The produced fluids were depressurized, collected and measured at atmospheric conditions.

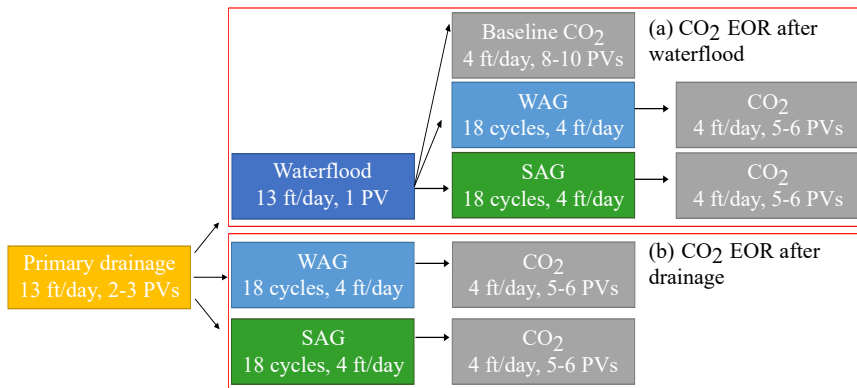


Fig. 2. Injection schemes. Each experiment started with primary drainage, then different CO₂ injection strategies were implemented either after waterflood (a) or directly after drainage (b). Three injection strategies were performed: pure CO₂ injection, WAG and SAG.

here and the optimal gas fraction was between 0.50 and 0.60 for both superficial velocities.

The effect of a lower surfactant concentration on foam strength was observed at lower superficial velocity (Fig. 3(a)). Foam apparent viscosity was slightly higher using 0.50 wt% foaming solution compared to 0.25 wt%. Alcorn et al. (2019) reported the same behavior using foaming solutions of 1 wt% and 0.50 wt% with the same surfactant. Their results showed that reduction of surfactant concentration did not reduce the efficiency on EOR and CO₂ storage which is beneficial for field-scale applications. At higher superficial velocity the apparent viscosity was not affected by surfactant concentration (Fig. 3(b)). Comparison of the two injection velocities showed slightly stronger foam generation at higher velocity. Based on the foam quality scans, 0.60 was identified

as the optimal gas fraction for the rate scans.

Fig. 4 shows apparent viscosity as a function of superficial velocity using foaming solutions with 0.25 wt% (green) and 0.50 wt% (red) surfactant concentration. Results showed a near-Newtonian foam behavior where foam apparent viscosity was similar and independent of superficial velocity. For 0.25 wt% foaming solution, the average apparent viscosity was 26.8 ± 4.7 cP and for 0.50 wt% foaming solution the average apparent viscosity was 26.6 ± 1.4 cP. The average values are within the uncertainty range of each measurement. Many studies report shear-thinning behavior where apparent viscosity increases with decreasing superficial velocity for surfactant-stabilized foams (Lee and Heller, 1990; Rognmo et al., 2017). However, this behavior was not observed during the experiments. Alvarez et al. (2001) have reported similar

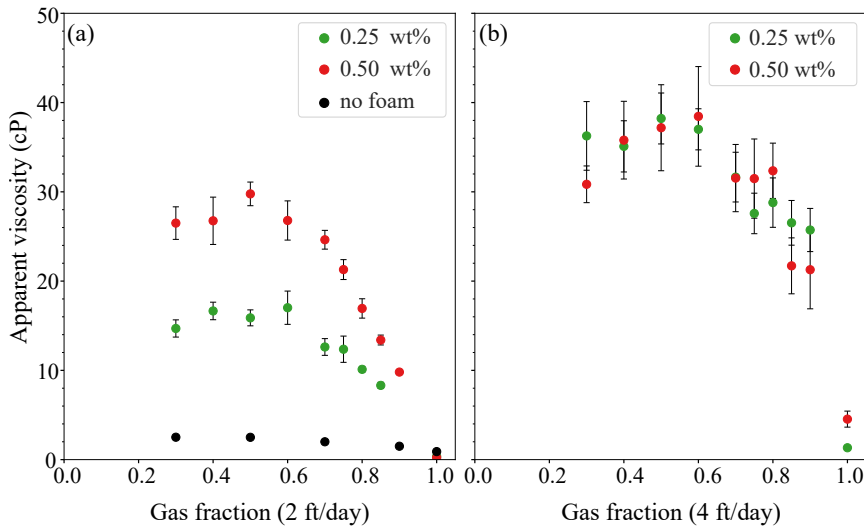


Fig. 3. Apparent viscosity as a function of gas fraction during steady state co-injection using two surfactant concentrations. Left graph is at superficial velocity of 2 ft/day and right at 4 ft/day. Each point was calculated when steady state was obtained. Injection without foaming solution (black dots, no foam) has been performed for comparison. Stronger foam generation was observed using higher surfactant concentration. Highest apparent viscosity was at gas fraction between 0.50 and 0.60.

behavior using a nonionic surfactant. The behavior is not fully understood but may be explained by pore geometry. It has been reported that pore throat size and pore angularity have an effect on foam generation and stability due to the effect on capillary pressure (Osei-Bonsu et al., 2018). Based on the results from rate scans, 4 ft/day was chosen as superficial velocity for the following EOR experiments.

4.2 Injection strategies for CO₂ and carbon storage

4.2.1 Pure CO₂ injection after waterflood

A baseline CO₂ injection was performed where supercritical CO₂ was injected into the core after waterflood to investigate CO₂ EOR and associated CO₂ storage. Fig. 5 shows apparent viscosity and recovery factors for baseline CO₂ injection (gray). Results showed low apparent viscosity because no foam was generated in absence of surfactant. The results also showed that 45% of original oil in place (OOIP) was recovered during waterflood and only 8% of OOIP was recovered during the subsequent CO₂ injection. CO₂ is miscible with n-Decane therefore high oil recovery was expected (Song et al., 2011). Low recovery can be explained by water shielding, a phenomenon where oil droplets are trapped within the water phase and are not in contact with the solvent. Earlier studies have shown that water shielding is significant especially for water-wet cores (Shelton and Schneider, 1975; Muller and Lake, 1991). Poor sweep efficiency due to rock heterogeneity can also reduce oil recovery (Chang et al., 1990). Pini et al. (2013) have shown that there is a degree

of heterogeneity in apparently homogenous sandstone cores which will affect the displacement front. Water recovery factor during the CO₂ injection was low (11%) as shown in Fig. 5. Poor water displacement can be explained by the high CO₂ mobility compared to water which lead to viscous fingering and early gas breakthrough (Lake et al., 2014).

4.2.2 Pure CO₂ injection after foaming solution injection

The effect of foam on CO₂ EOR efficiency and CO₂ storage capacity was evaluated by injecting foaming solution, rather than only waterflooding, prior to CO₂ injection. Fig. 5 shows the apparent viscosity and recovery factors as a function of PVs injected for baseline CO₂ injection after waterflood (gray) and CO₂ injection after foaming solution injection (green). Foam was generated as soon as CO₂ injection started into the core as indicated from the rapid increase in apparent viscosity (Fig. 5, green solid curve). The apparent viscosity increased until a peak of approximately 9 cP was reached, before decreasing and indication of foam coalescence. The reduction in water saturation and development of continuous CO₂ flow paths not impeded by lamella caused the foam to dry out (Farajzadeh et al., 2015; Benali et al., 2022). After several PVs injected, the apparent viscosity remained slightly higher than for the baseline experiment indicating decreased CO₂ mobility due to foam generation. The calculated recovery factors showed a positive effect of foam on both oil and water displacement. The total oil recovery was 53% for the experiment without foam and was 78% for the experiment with foam. Water recovery was also significantly higher for the experiment with foam where 60% of the water was displaced

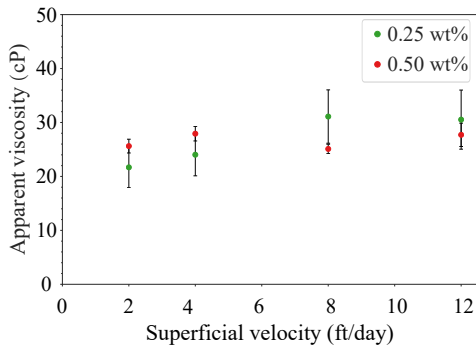


Fig. 4. Apparent viscosity as a function of superficial velocity for steady state co-injection of CO₂ and foaming solutions with 0.25 wt% (green) and 0.50 wt% (red) surfactant concentrations. Gas fraction was 0.60 for both. Near-Newtonian behavior was observed as foam apparent viscosity was independent of the velocity.

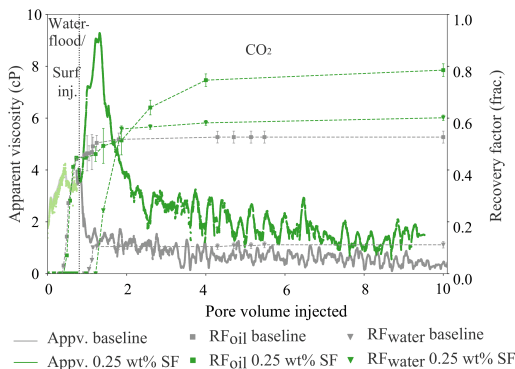


Fig. 5. Apparent viscosity (solid lines) and recovery factors (dotted lines) as a function of pore volume injected for CO₂ injection after waterflood (gray) and after foaming solution injection (green). Results show an increase in apparent viscosity when surfactant was present in the core. Oil and water recovery factors are higher because of foam generation.

compared to 11% for the baseline CO₂ injection. High water recovery is beneficial for CO₂ storage as more pore space can be available to store CO₂.

4.2.3 WAG after waterflood

WAG is a common method to reduce CO₂ mobility and was evaluated to establish a baseline for comparison to SAG experiments for CO₂ EOR and CO₂ storage. Fig. 6 shows an increase in apparent viscosity during WAG compared to the baseline CO₂ injection due to a reduction in CO₂ relative permeability in the presence of higher water saturations (Enick et al., 2012). The apparent viscosity varied between 1 and 3.5 cP during the WAG cycles and rapidly decreased to the same

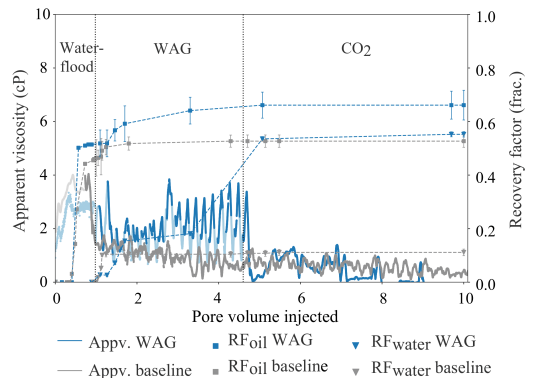


Fig. 6. Apparent viscosity (solid lines) and recovery factors (dotted lines) as a function of pore volume injected for WAG (blue) and baseline CO₂ injection (gray) for comparison. Light and dark colors represent brine and CO₂ injection respectively. Apparent viscosity increased due to CO₂ relative permeability reduction. Oil and water recovery factors are higher than for baseline.

values as the baseline when only CO₂ was injected. This was due to the decrease in water saturation and increase in CO₂ relative permeability. As a result of mobility control through WAG, 15% of additional oil was displaced compared to 8% during the baseline CO₂ injection. Water recovery factor showed improved water displacement for WAG (55%) compared to CO₂ baseline (11%) which increased the CO₂ storage capacity.

4.2.4 SAG after waterflood

Two SAG injections with different surfactant concentrations were performed to evaluate the effect of surfactant concentration of foam strength, stability and CO₂ EOR and CO₂ storage potential. Fig. 7 shows apparent viscosity, oil recovery factor and water recovery factor for 0.25 wt% (green) and 0.50 wt% (red) foaming solution and WAG (blue). An increase in apparent viscosity was observed when surfactant was present in the solution, indicating foam generation. For both solutions the apparent viscosity started to increase after the second SAG cycle. Within each cycle the apparent viscosity increased for the CO₂ slugs and decreased for the surfactant slugs which indicated foam generation in a drainage-like process as also observed by (Kovscek and Radke, 1994). For the 0.25 wt% foaming solution, the apparent viscosity stabilized after 6 cycles and was on average 7 cP. After 18 SAG cycles, pure CO₂ was injected which resulted in a rapid decrease in apparent viscosity. This can be explained by the dry out effect. When pure CO₂ was injected into the core, the foaming solution saturation decreased, gas fraction increased and coarsening of foam occurred. The rate of foam generation and coalescence equated and foam started to collapse or dry out (Abbaszadeh et al., 2014). The apparent viscosity remained higher for the SAG, compared to the WAG, for several PVs CO₂ injected. This indicated trapped gas bubbles within the pores that con-

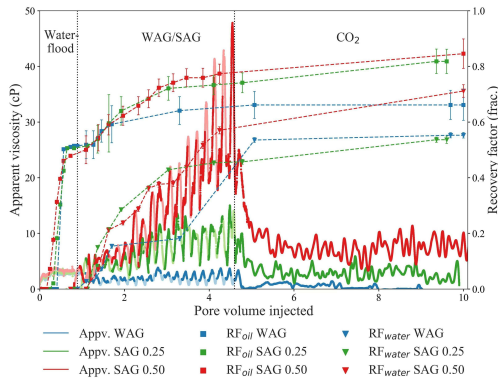


Fig. 7. Apparent viscosity (solid lines) and recovery factors (dotted lines) as a function of pore volume injected for WAG (blue), SAG with 0.25 wt% foaming solution (green) and SAG with 0.50 wt% foaming solution (red). Light and dark colors represent brine and CO₂ injection respectively. CO₂ foam was generated in presence of surfactant indicated by increase in apparent viscosity. Foam increased oil and water recovery.

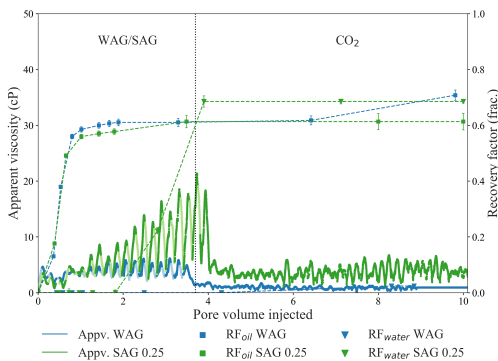


Fig. 8. Apparent viscosity (solid lines) and recovery factors (dotted lines) as a function of pore volume injected for WAG (blue) and SAG (green) as primary recovery method. Light and dark colors represent brine and CO₂ injection respectively. During SAG foam was generated after a significant amount of oil was displaced. Water recovery was higher during SAG compared to WAG.

tributed to continued CO₂ mobility reduction (Jones et al., 2018; Benali et al., 2022).

For the 0.50 wt% foaming solution the apparent viscosity continued to increase even after 18 SAG cycles indicating generation of stronger foam as the injection continued. A rapid decrease in apparent viscosity was observed when pure CO₂ was injected. The apparent viscosity remained one order of magnitude higher than during WAG for several PVs injected indicating CO₂ mobility reduction. Comparison of the two foaming solutions showed stronger foam generation using the

higher surfactant concentration and increased CO₂ mobility reduction.

Generation of CO₂ foam during SAG increased oil and water displacement compared to WAG where no foam was generated. Before WAG and SAG cycles waterflood was performed and approximately 50% of OOIP was recovered for the three experiments. During WAG a total of 66% of OOIP was recovered and the oil recovery stopped after ended WAG cycles. During the SAG injections the total oil recovery was 82%-85% of which 9% OOIP was produced during the pure CO₂ injection stage. Higher apparent viscosity using 0.50 wt% foaming solution did not show significant improvement in oil recovery. This has been observed earlier and is economically beneficial for designing foam formulations for use at the field-scale (Alcorn et al., 2019). An increase in water recovery was also observed when foam was generated. More than 50% of the water was displaced during WAG and 0.25 wt% SAG and 70% was displaced during 0.50 wt% SAG. The increase in foam apparent viscosity had a significant effect on water displacement which resulted in more pore space available for CO₂ storage (Føyen et al., 2020).

4.2.5 WAG and SAG after drainage

WAG and SAG injection methods were implemented directly after primary drainage (i.e., no initial waterflood) with an initial oil saturation of approximately 70%. Fig. 8 shows the apparent viscosity, oil recovery and water recovery for WAG (blue) and SAG (green) as a function of PV injected. During the first 5 cycles, the apparent viscosity and oil recovery was similar for the two injection strategies. After 1.5 PVs injected the apparent viscosity started to increase indicating foam generation. At that point approximately 60% of the OOIP was recovered and oil saturation in the core was 30%. The delay in foam generation compared to SAG after waterflood (Fig. 7, green solid curve) was influenced by the presence of oil. The high amount of mobile oil in the core limited foam generation until the oil saturation was below a critical oil saturation for foam to generate (Friedmann and Jensen, 1986; Mannhardt et al., 1998). Higher apparent viscosity was observed compared to SAG after waterflood (Fig. 7, green curve), which is due to generation of oil/water emulsions in addition to CO₂ foam (Amirmoshiri et al., 2018; Alcorn et al., 2020). Similar to foam, emulsions can contribute to increased flow resistance, hence increased apparent viscosity (McAuliffe, 1973). The apparent viscosity for WAG after drainage was also higher than for WAG after waterflood (Fig. 7, blue solid curve) because of higher flow resistance at higher oil saturations. Foam and emulsions did not contribute to increase the oil recovery as the most part of oil was recovered before foam generation started. However, an improvement in water displacement was observed. During the SAG, 70% of the water was displaced whereas only 3% of water was displaced during WAG. After the 18 WAG and SAG cycles, pure CO₂ was injected into the core for additional 6 to 7 PVs. The apparent viscosity for WAG rapidly decreased to the same values as baseline CO₂ injection because of foam dry out (Fig. 6, gray solid curve). For the SAG, the apparent viscosity remained higher than baseline CO₂ injection due to trapped CO₂ bubbles in the pore

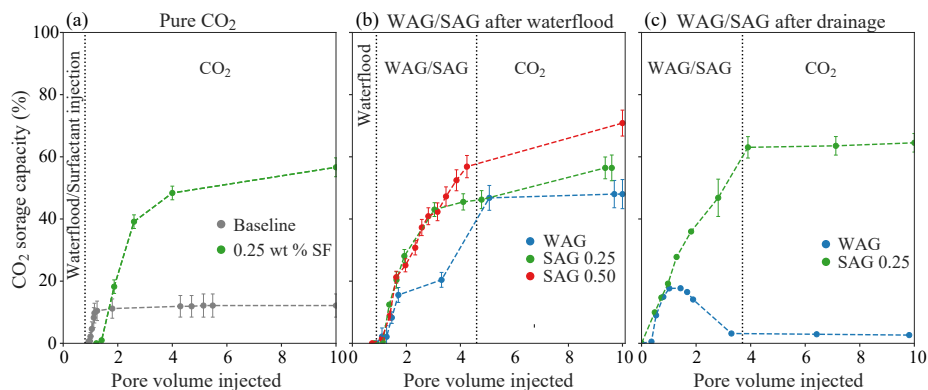


Fig. 9. CO₂ storage capacity versus pore volume injected for the different injection strategies. (a) Pure CO₂ injection after waterflood (gray) and after surfactant injection (green), (b) WAG (blue), SAG with 0.25 wt% (green) and SAG with 0.50 wt% surfactant concentration performed after waterflood, (c) WAG (blue) and SAG (green) performed after drainage. CO₂ foam increased CO₂ storage capacity for all injection strategies.

space, which continued to reduce the CO₂ mobility. Overall, the results did not show improvement in oil displacement when using WAG and SAG directly after drainage compared to WAG and SAG implemented after waterflood.

4.2.6 CO₂ storage

Fig. 9 shows CO₂ storage capacity versus pore volume injected for the different injection strategies. For the baseline CO₂ injection (Fig. 9(a), gray), the storage potential was 12% which was the lowest compared to the other injections. This was because of poor water and oil displacement. Changing the injection strategy to WAG increased storage potential to approximately 50% (Fig. 9(b), blue). Higher storage potential was estimated for all experiments containing foaming solution due to foam generation and improved fluid displacement. The injections containing 0.25 wt% foaming solution resulted in a CO₂ storage capacity of approximately 55% to 60% (Fig. 9(a), Fig. 9(b), Fig. 9(c), green). The highest CO₂ storage capacity (70%) was when stronger foam was generated using 0.50 wt% foaming solution (Fig. 9(b), red). Comparison of WAG after waterflood (Fig. 9(b), blue) and WAG after drainage (Fig. 9(c), blue) showed higher CO₂ storage capacity for WAG after waterflood. The CO₂ storage capacity for WAG after drainage was low because of poor water displacement. Comparison of SAG after waterflood (Fig. 9(b), green) and SAG after drainage (Fig. 9(c), green) showed higher CO₂ storage capacity for SAG after drainage. This was likely due to generation of oil/water emulsions in addition to CO₂ foam which contribute to increased displacement. Overall, foam generation reduced CO₂ mobility, increased displacement and therefore improved the storage capacity.

5. Conclusions

Understanding unsteady-state in-situ CO₂ foam behavior is important for upscaling and implementation of CO₂ foam

for EOR and associated CO₂ storage at the field-scale. The primary objective was to reduce CO₂ mobility, through the generation of foam, in experiments that are representative of field-scale injection strategies. A secondary objective was to investigate the effect of oil on CO₂ foam generation and stability. Therefore, this work focused on establishing a knowledge base and procedure for investigating core-scale unsteady-state CO₂ foam injection strategies. Pure unsteady-state CO₂ injection, WAG and SAG were performed at reservoir conditions and evaluated based on apparent viscosity, oil and water recovery and CO₂ storage capacity. The following key observations and conclusions were drawn:

- Foam quality scans showed that the optimal gas fraction (highest apparent viscosity) was between 0.50 and 0.60 for both surfactant concentrations (0.25 wt% and 0.50 wt%). Rate scans showed a near-Newtonian foam behavior where foam strength was independent of the superficial velocity.
- Injecting foaming solution before CO₂ injection generated foam and improved oil and water displacement compared to only waterflooding before CO₂ injection.
- Reduction of CO₂ relative permeability during WAG increased oil and water recovery compared to the CO₂ baseline, where only CO₂ was injected.
- Generation of CO₂ foam during SAG improved oil displacement by 25% and 50% compared to WAG and to the CO₂ baseline, respectively.
- Foam increased CO₂ storage capacity by 20% to 40% compared to WAG and 350% to 450% compared to the CO₂ baseline.
- Increasing surfactant concentration from 0.25 wt% to 0.50 wt% increased foam apparent viscosity and resulted in improved water displacement and increased CO₂ storage capacity but did not have an impact on oil recovery.
- High oil saturations during WAG and SAG injections

directly after drainage hindered CO₂ foam generation until a critical oil saturation of 30% was reached. In addition to CO₂ foam, generation of oil/water emulsions was observed. Performing WAG and SAG directly after drainage did not have impact on oil recovery compared to WAG and SAG after waterflood.

Acknowledgement

The authors wish to acknowledge the Research Council of Norway PETROMAKS2 program for financial support under grant number 301201 - Optimizing CO₂ Foam EOR Mobility Control for Field Pilots.

Conflict of interest

The authors declare no competing interest.

Open Access This article is distributed under the terms and conditions of the Creative Commons Attribution (CC BY-NC-ND) license, which permits unrestricted use, distribution, and reproduction in any medium, provided the original work is properly cited.

References

- Abbaszadeh, M., Nia Korrani, A. K., Lopez-Salinas, J. L., et al. Experimentally-based empirical foam modeling. Paper SPE 169888 Presented at SPE Improved Oil Recovery Symposium, Tulsa, Oklahoma, USA, 12-16 April, 2014.
- Alcorn, Z. P., Føyen, T., Gauteplass, J., et al. Pore- and core-scale insights of nanoparticle-stabilized foam for CO₂-enhanced oil recovery. *Nanomaterials*, 2020, 10(10): 1917.
- Alcorn, Z. P., Føyen, T., Zhang, L., et al. CO₂ foam field pilot design and initial results. Paper SPE 200450 Presented at SPE Improved Oil Recovery Conference, Virtual, 31 August-4 September, 2020.
- Alcorn, Z. P., Fredriksen, S. B., Sharma, M., et al. An integrated carbon-dioxide-foam enhanced-oil-recovery pilot program with combined carbon capture, utilization, and storage in an onshore Texas heterogeneous carbonate field. *SPE Reservoir Evaluation & Engineering*, 2019, 22(4): 1449-1466.
- Alvarez, J. M., Rivas, H. J., Rossen, W. R. Unified model for steady-state foam behavior at high and low foam qualities. *SPE Journal*, 2001, 6(3): 325-333.
- Amirmoshiri, M., Zeng, Y., Chen, Z., et al. Probing the effect of oil type and saturation on foam flow in porous media: Core-flooding and nuclear magnetic resonance (NMR) imaging. *Energy & Fuels*, 2018, 32(11): 11177-11189.
- Benali, B., Føyen, T. L., Alcorn, Z. P., et al. Pore-scale bubble population dynamics of CO₂-foam at reservoir pressure. *International Journal of Greenhouse Gas Control*, 2022, 114: 103607.
- Bjørlykke, K. *Petroleum Geoscience: From Sedimentary Environments to Rock Physics*. Heidelberg, German, Springer, 2010.
- Chang, S.-H., Grigg, R. B. Effects of foam quality and flow rate on CO₂-foam behavior at reservoir temperature and pressure. *SPE Reservoir Evaluation & Engineering*, 1999, 2(3): 248-254.
- Chang, S. H., Owusu, L. A., French, S. B., et al. The effect of microscopic heterogeneity on CO₂-foam mobility: Part 2-mechanistic foam simulation. Paper SPE 20191 Presented at SPE/DOE Enhanced Oil Recovery Symposium, Tulsa, Oklahoma, 22-25 April, 1990.
- Chou, S. I., Vasicek, S. L., Pisis, D. L., et al. CO₂ foam field trial at north ward-estes. Paper SPE 24643 Presented at 67th Annual Technical Conference and Exhibition of the Society of Petroleum Engineers, Washington, D. C., 4-7 October, 1992.
- Christensen, J. R., Stenby, E. H., Skauge, A. Review of wagg field experience. *SPE Reservoir Evaluation & Engineering*, 2001, 4(2): 97-106.
- Enick, R. M., Olsen, D. K., Ammer, J., et al. Mobility and conformance control for carbon dioxide enhanced oil recovery (CO₂-EOR) via thickeners, foams, and gels—A detailed literature review of 40 years of research. Paper SPE 154122 Presented at SPE Improved Oil Recovery Symposium, Tulsa, Oklahoma, 14-18 April, 2012.
- Falls, A. H., Musters, J. J., Ratulowski, J. The apparent viscosity of foams in homogeneous bead packs. *SPE Reservoir Engineering*, 1989, 4(2): 155-164.
- Farajzadeh, R., Andrianov, A., Krastev, R., et al. Foam-oil interaction in porous media: Implications for foam assisted enhanced oil recovery. *Advances in Colloid and Interface Science*, 2012, 183-184: 1-13.
- Farajzadeh, R., Lotfollahi, M., Eftekhari, A. A., et al. Effect of permeability on implicit-texture foam model parameters and the limiting capillary pressure. *Energy & Fuels*, 2015, 29(5): 3011-3018.
- Føyen, T., Brattekkås, B., Fernø, M. A., et al. Increased CO₂ storage capacity using CO₂-foam. *International Journal of Greenhouse Gas Control*, 2020, 96: 103016.
- Friedmann, F., Jensen, J. A. Some parameters influencing the formation and propagation of foams in porous media. Paper SPE 15087 Presented at SPE California Regional Meeting, Oakland, California, 2-4 April, 1986.
- Hoefner, M. L., Evans, E. M. CO₂ foam: Results from four developmental field trials. *SPE Reservoir Engineering*, 1995, 10(4): 273-281.
- Hanssen, J. E., Holt, T., & Surguchev, L. M. Foam processes: An assessment of their potential in north sea reservoirs based on a critical evaluation of current field experience. Paper SPE 27768 Paper presented at the SPE/DOE Improved Oil Recovery Symposium, Tulsa, Oklahoma, 17-20 April, 1994.
- Jones, S. A., Getrouw, N., Vincent-Bonnieu, S. Foam flow in a model porous medium: II. The effect of trapped gas. *Soft Matter*, 2018, 14(18): 3497-3503.
- Jones, S. A., Laskaris, G., Vincent-Bonnieu, S., et al. Surfactant effect on foam: From core flood experiments to implicit-texture foam-model parameters. *Journal of Industrial and Engineering Chemistry*, 2016, 37: 268-276.
- Khatib, Z. I., Hirasaki, G. J., Falls, A. H. Effects of capillary pressure on coalescence and phase mobilities in foams flowing through porous media. *SPE Reservoir Engineering*, 1988, 3(3): 919-926.
- Kovscek, A. R., Radke, C. J. *Fundamentals of foam transport*

- in porous media, in *Foams: Fundamentals and Applications in the Petroleum Industry*, edited by L. L. Schramm, American Chemical Society, Washington, pp. 115-163, 1994.
- Lake, L. W., Johns, R. T., Rossen, W. R., et al. *Fundamentals of enhanced oil recovery*. Richardson, TX: Society of Petroleum Engineers, 2014.
- Lee, H. O., Heller, J. P. Laboratory measurements of CO₂-foam mobility. *SPE Reservoir Engineering*, 1990, 5(2): 193-197.
- Lee, S., Kam, S. I. Chapter 2-Enhanced oil recovery by using CO₂ foams: Fundamentals and field applications, in *Enhanced Oil Recovery Field Case Studies*, edited by J. J. Sheng, Gulf Professional Publishing, Boston, pp. 23-61, 2013.
- Mannhardt, K., Novosad, J. J., Schramm, L. L. Foam/oil interactions at reservoir conditions. Paper SPE 39681 Presented at SPE/DOE Improved Oil Recovery Symposium, Tulsa, Oklahoma, 19-22 April, 1998.
- Massarweh, O., Abushaikha, A. S. [A review of recent developments in CO₂ mobility control in enhanced oil recovery. Petroleum, 2021.](#)
- McAuliffe, C. D. Oil-in-water emulsions and their flow properties in porous media. *Journal of Petroleum Technology*, 1973, 25(6): 727-733.
- Metz, B., Davidson, O., De Coninck, H. C., et al. *IPCC Special Report on Carbon Dioxide Capture and Storage*. London, United States, Cambridge University Press for the Intergovernmental Panel on Climate Change, 2005.
- Muller, T., Lake, L. W. Theoretical study of water blocking in miscible flooding. *SPE Reservoir Engineering*, 1991, 6(4): 445-451.
- Osei-Bonsu, K., Grassia, P., Shokri, N. Effects of pore geometry on flowing foam dynamics in 3D-printed porous media. *Transport in Porous Media*, 2018, 124(3): 903-917.
- Osterloh, W. T., Jante, M. J., Jr. Effects of gas and liquid velocity on steady-state foam flow at high temperature. Paper SPE 24179 Presented at SPE/DOE Enhanced Oil Recovery Symposium, Tulsa, Oklahoma, 22-24 April, 1992.
- Peksa, A. E., Wolf, K.-H. A. A., Zitha, P. L. J. Bentheimer sandstone revisited for experimental purposes. *Marine and Petroleum Geology*, 2015, 67: 701-719.
- Pini, R., Krevor, S., Krause, M., et al. Capillary heterogeneity in sandstone rocks during CO₂/water core-flooding experiments. *Energy Procedia*, 2013, 37: 5473-5479.
- Rognmo, A. U., Horjen, H., Fernø, M. A. Nanotechnology for improved CO₂ utilization in ccs: Laboratory study of CO₂-foam flow and silica nanoparticle retention in porous media. *International Journal of Greenhouse Gas Control*, 2017, 64: 113-118.
- Ross, S., McBain, J. W. Inhibition of foaming in solvents containing known foamers. *Industrial & Engineering Chemistry*, 1944, 36(6): 570-573.
- Rossen, W. R. Foams in enhanced oil recovery, in *Foams: Theory, Measurements and Applications*, edited by R. K. Prud'homme and S. A. Khan, Routledge, New York, pp. 413-464, 1996.
- Schramm, L. L. *Foams: Fundamentals and Applications in the Petroleum Industry*. Washington, D. C., American Chemical Society, 1994.
- Shan, D., Rossen, W. R. Optimal injection strategies for foam ior. *SPE Journal*, 2004, 9(2): 132-150.
- Sharma, M. CO₂ mobility control with foam for enhanced oil recovery and associated storage multi-scale approach for field application. Norway, University of Stavanger, 2019.
- Shelton, J. L., Schneider, F. N. The effects of water injection on miscible flooding methods using hydrocarbons and carbon dioxide. *Society of Petroleum Engineers Journal*, 1975, 15(3): 217-226.
- Skauge, A., Aarra, M. G., Surguchev, L., et al. Foam-assisted wag: Experience from the snorre field. Paper SPE 75157 presented at the SPE/DOE Improved Oil Recovery Symposium, Tulsa, Oklahoma, 13-17 April, 2002.
- Song, Y.-C., Zhu, N.-J., Liu, L., et al. Magnetic resonance imaging study on the miscibility of a CO₂/n-decane system. *Chinese Physics Letters*, 2011, 28(9): 096401.
- Tadros, T. F. *Basic Principles of Dispersions*. Berlin/Boston, Germany, De Gruyter, 2017.
- Talebian, S. H., Masoudi, R., Tan, I. M., et al. Foam assisted CO₂-EOR: A review of concept, challenges, and future prospects. *Journal of Petroleum Science and Engineering*, 2014, 120: 202-215.

Paper 6

Article

Unsteady-State CO₂ Foam Generation and Propagation: Laboratory and Field Insights

Zachary Paul Alcorn *, Aleksandra Sæle, Metin Karakas and Arne Graue

Department of Physics and Technology, University of Bergen, 5009 Bergen, Norway

* Correspondence: zachary.alcorn@uib.no

Abstract: This work presents a multiscale experimental and numerical investigation of CO₂ foam generation, strength, and propagation during alternating injection of surfactant solution and CO₂ at reservoir conditions. Evaluations were conducted at the core-scale and with a field-scale radial simulation model representing a CO₂ foam field pilot injection well. The objective of the experimental work was to evaluate foam generation, strength, and propagation during unsteady-state surfactant-alternating-gas (SAG) injection. The SAG injection rapidly generated foam based upon the increased apparent viscosity compared to an identical water-alternating-gas (WAG) injection, without surfactant. The apparent foam viscosity of the SAG continually increased with each subsequent cycle, indicating continued foam generation and propagation into the core. The maximum apparent viscosity of the SAG was 146 cP, whereas the maximum apparent viscosity of the WAG was 2.4 cP. The laboratory methodology captured transient CO₂ foam flow which sheds light on field-scale CO₂ foam flow. The single-injection well radial reservoir simulation model investigated foam generation, strength, and propagation during a recently completed field pilot. The objective was to tune the model to match the observed bottom hole pressure data from the foam pilot and evaluate foam propagation distance. A reasonable match was achieved by reducing the reference mobility reduction factor parameter of the foam model. This suggested that the foam generated during the pilot was not as strong as observed in the laboratory, but it has propagated approximately 400 ft from the injection well, more than halfway to the nearest producer, at the end of pilot injection.

Keywords: foam; CO₂; EOR; multiscale

Citation: Alcorn, Z.P.; Sæle, A.; Karakas, M.; Graue, A. Unsteady-State CO₂ Foam Generation and Propagation: Laboratory and Field Insights. *Energies* **2022**, *15*, 6551. <https://doi.org/10.3390/en15186551>

Academic Editors: Daoyong Yang, Shengnan Chen, Huazhou Li, Yin Zhang, Xiaoli Li and Zhaoqi Fan

Received: 18 August 2022
Accepted: 3 September 2022
Published: 7 September 2022

Publisher's Note: MDPI stays neutral with regard to jurisdictional claims in published maps and institutional affiliations.



Copyright: © 2022 by the authors. Licensee MDPI, Basel, Switzerland. This article is an open access article distributed under the terms and conditions of the Creative Commons Attribution (CC BY) license (<https://creativecommons.org/licenses/by/4.0/>).

1. Introduction

Foam has emerged as a promising, cost effective technique to reduce CO₂ mobility for improved sweep efficiency during CO₂ enhanced oil recovery (EOR) and CO₂ storage processes [1–4]. Foam is a dispersion of gas in a continuous liquid phase where gas flow is impeded by thin liquid films called lamellae [5,6]. Lamellae are often stabilized by water-soluble surfactants which reduce surface tension and are screened to ensure minimal adsorption on reservoir rock. Foam is generated in-situ by simultaneous injection of CO₂ and surfactant solution (co-injection) or in alternating slugs of CO₂ and surfactant solution [7,8]. Once foam is generated, it is propagated through the porous medium at an initial unsteady-state and then later at steady-state. Unsteady-state foam is characterized by a rapidly increasing pressure drop, whereas the pressure drop is constant at steady-state and can be described with Darcy's Law [9,10]. In addition, significant differences in relative permeability have been observed between steady- and unsteady-state foam flow [11]. At the field scale, it is assumed that foam is at steady-state [12]. However, foam may encounter both unsteady-state and steady-state flow regimes, with unsteady-state flow dominating the near wellbore area.

Foam injection must balance injectivity, mobility reduction, and operational constraints. At laboratory scale, co-injection is the most common injection strategy because of the ability to achieve steady-state and for deriving foam model parameters [13]. In addition,

co-injection offers the most control of injected foam quality [14]. However, co-injection can be challenging at the field-scale because of operational limitations, extremely low injectivities, rapid pressure increases, and challenges associated with downhole corrosion [15]. This has led to most field tests using a surfactant-alternating-gas (SAG) injection strategy. Additionally, SAG processes have been shown to be the optimal injection strategy to overcome gravity override and to maintain injectivity [16].

Details on in-situ foam generation and propagation during unsteady-state flow are needed because they significantly impact injectivity, which is crucial to the success of foam applications for EOR and CO₂ storage. However, few attempts have been made to characterize transient CO₂ foam behavior during alternating injection of surfactant solution and CO₂ slugs at reservoir conditions. Moreover, the connection between laboratory and field-scale transient foam flow is unclear. To further complicate the matter, conventional reservoir simulations calculate injectivity assuming a uniform saturation and mobility in the injection-well grid block. Therefore, injectivity in a simulation of an SAG process is extremely poor [17]. In reality, foam in the near-well region rapidly dries out and injectivity is much greater than estimated in a finite-difference simulation. Foam dry-out occurs at high gas fractional flows due to foam coalescence and depletion of adequate surfactant solution. The large injectivity reduction can be compounded by limited variation in foam apparent viscosity at different gas fractions from experimental data used to derive foam model parameters. Therefore, an approach to capture foam dry-out in the near-well region is needed.

This work presents a multiscale investigation of unsteady-state CO₂ foam generation, strength, and propagation at reservoir conditions. The main objective of the experimental work was to evaluate foam generation and propagation during unsteady-state SAG injection at reservoir conditions to assist with field pilot interpretations. The aim was to develop a laboratory methodology for CO₂ foam quantification during SAG injection, representative of the near wellbore region. The objective of the field-scale modeling work was to calibrate a radial reservoir simulation model to the observed behavior from a recently completed CO₂ foam field pilot test. An approach to capture the foam dry-out effect near the well is proposed.

2. Pilot Overview

A surfactant-stabilized CO₂ foam pilot was conducted in a mature heterogeneous carbonate reservoir in East Seminole Field, Permian Basin USA [18]. The main objective was to achieve in-depth CO₂ mobility control to increase CO₂ sweep efficiency and improve the CO₂ utilization factor. The foam formulation was designed in the laboratory by measuring surfactant adsorption and verifying foam stability in the presence of residual oil [19–21].

The pilot area was an inverted 40 acre five-spot pattern with a central injection well and four surrounding producers. The pilot injection strategy was designed to mitigate injectivity losses due to strong foam generation and to volumetrically target the optimal 70% foam quality, as recommended from the laboratory studies. A rapid surfactant-alternating-gas (SAG) injection strategy began in May 2019. The injection strategy consisted of SAG cycles with 10 days of surfactant solution injection followed by 20 days of CO₂ injection. Eleven complete SAG cycles were injected for total of 10% hydrocarbon pore volume (HCPV) injected at the completion of the pilot in August 2020. Figure 1 shows the observed injection rates and bottom hole pressure (BHP) during the pilot.

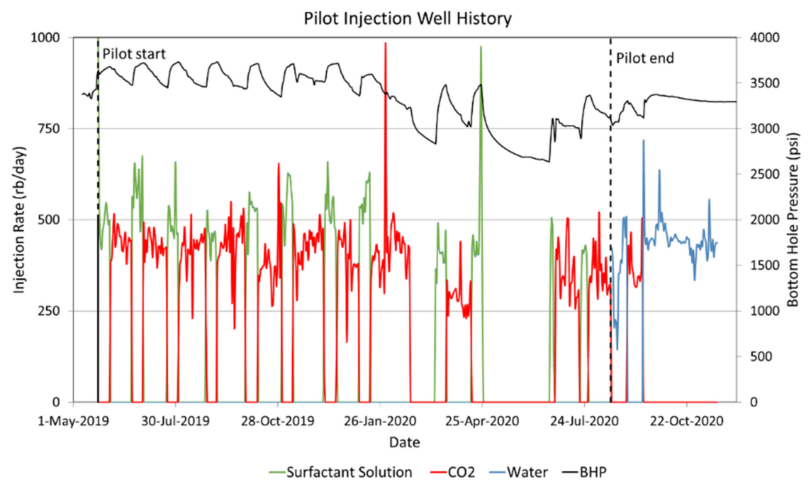


Figure 1. Observed injection rates and bottom hole pressure (BHP) during the foam pilot. The red curve corresponds to CO₂ injection, the green curve to surfactant solution injection, and the blue to water injection. The BHP is shown as the black curve.

Pilot Monitoring

The baseline data collection and pilot monitoring program aimed to obtain baseline from pre-pilot CO₂ and water injection periods and monitor pilot performance to evaluate reservoir response to foam injection. Foam was expected to reduce CO₂ mobility, thus the baseline period focused on characterizing interwell connectivity and injectivity of CO₂ and water. The baseline data collection program consisted of CO₂ injection profile logs, an interwell CO₂ tracer test (IWTT) and collection of injection and production flow rates for comparison to repeat surveys during the pilot. The pilot monitoring program included repeat CO₂ injection profiles, an IWTT, three-phase production monitoring and collection of downhole pressure data for evaluation of reservoir response to foam injection. The injection bottom hole pressure and temperature were monitored by mounting a downhole pressure gauge (DHPG) in the pilot injection well. Produced fluids were also collected, before the pilot and once a week during the pilot, for chemical analysis to determine surfactant breakthrough time.

Foam generation was confirmed during the pilot based upon a delay in CO₂ breakthrough compared to the baseline CO₂ breakthrough time, higher BHP values during the pilot compared to pre-pilot values, and more evenly distributed injection profiles during the pilot compared to the pre-pilot period. In addition, an increase in oil production was observed with less volumes of CO₂ injected during the pilot, compared to conventional CO₂ injection, thereby improving the CO₂ utilization factor and the economics of the project. Pilot results are discussed in detail in [22]. Observed BHP values and injection rates were used in this work to calibrate the radial reservoir model as discussed below.

3. Experimental Materials

The objective of the unsteady-state CO₂ foam experiments was to evaluate foam generation, strength, and collapse during alternating injection of CO₂ and surfactant solution to assist in the interpretation of the recently completed field pilot. The aim was to develop a laboratory methodology for CO₂ foam quantification during unsteady-state SAG injection, representative of the near wellbore region.

3.1. Rock and Fluid Properties

An outcrop Bentheimer sandstone was used for all experiments to maintain constant core properties. Bentheimer is a homogeneous, water-wet sandstone with a composition consisting of quartz (92%), clay minerals (3%) and feldspar (5%). The permeability was measured at an average of 2.14 ± 0.03 Darcy. Rock properties are shown in Table 1.

Table 1. Rock properties of the sandstone core material used in the experimental work.

Property	Value
Length (cm)	24.40 ± 0.01
Diameter (cm)	3.80 ± 0.01
Permeability (D)	2.14 ± 0.03
Pore Volume (mL)	62.16 ± 0.01
Porosity (%)	21.54 ± 0.10

Brine was prepared by dissolving 3.5 wt.% NaCl and distilled water. The foaming agent was a nonionic surfactant from Huntsman, SURFONIC L24-L22, that was dissolved in brine. The surfactant concentration was 0.50 wt% as also used in the pilot test. The SURFONIC L24-L22 surfactant demonstrated low adsorption in carbonate rock material, both in the absence and presence of CO₂ [19]. In addition, it is expected to have low adsorption on the surface of the Bentheimer sandstone. CO₂ of 99.999% purity was used during the foam injections. Isopropyl alcohol solution consisting of 87.5 wt.% isopropyl and 3.5 wt.% distilled water was injected to clean the core between each experiment. See Table 2 for an overview of fluid compositions used in the experimental work.

Table 2. Properties of the fluids used in the experimental work.

Fluid	Composition
Brine	Distilled water + 3.5 wt% NaCl
Surfactant solution	Brine + 0.5 wt% SURFONIC L24-L22
CO ₂	>99.999% CO ₂
Isopropyl alcohol	Distilled water + 87.5 wt% Di-propanol

3.2. Experimental Setup

Figure 2 shows a schematic of the experimental setup used for the unsteady-state CO₂ foam experiments. The temperature and pressure were set to reservoir conditions of 40 °C and 198 bar. The core was wrapped in a layer of nickel foil and placed inside of a Teflon rubber sleeve to prevent CO₂ diffusion into the sleeve [23]. The core was then inserted into a vertically-oriented hassler core holder. The system was pressurized by an N₂ tank connected with two Equilibar back pressure regulators (BPR) connected in series to reduce fluctuations and keep a constant pressure in the system. An ISCO pump kept the confinement pressure 70 bar over the system pressure. The confinement pressure, pressure at the inlet and outlet of the core and the pressure over the BPRs were measured and monitored by ESI-pressure transducers (Figure 2). The differential pressure over the core was used to calculate foam apparent viscosity and was measured by Aplisens Smart Differential Pressure Transmitter.

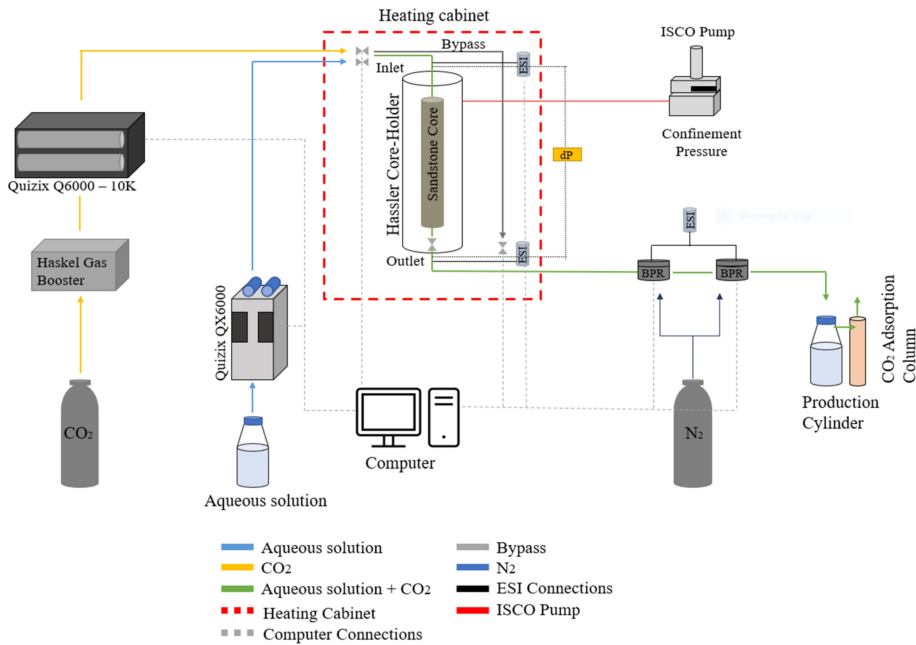


Figure 2. Illustration of experimental setup used for unsteady-state foam injections.

The aqueous solutions were injected through a Quizix QX6000-pump and CO₂ was injected through a Quizix Q6000-10K pump. CO₂ was pressurized by a Haskel gas booster to achieve a supercritical phase before it was injected through the pump and into the core. The production cylinder accumulated the production fluids from the outlet. The fluids were depressurized to atmospheric conditions and CO₂ was separated from the liquid solution by an adsorption column.

4. Experimental Methods

Foam generation, strength and stability were investigated during unsteady-state alternating slug injection of surfactant solution and CO₂. An identical WAG injection (without surfactant) was also conducted to establish a baseline for comparison. Foam generation and strength was quantified by calculating apparent viscosity (μ_{app}), which is based on the pressure measured across the core and is defined as:

$$\mu_{app} = \frac{k}{\mu_{gas} + \mu_{liquid}} \nabla p, \quad (1)$$

where k is the absolute permeability of the core, μ_{gas} and μ_{liquid} are the superficial velocities of gas and liquid, respectively, and ∇p is the pressure gradient across the core [24]. A higher apparent viscosity value corresponds to a stronger foam and increased resistance to flow.

The experimental procedure and injection strategy were designed to represent unsteady-state flow in the near wellbore region. The experimental procedure for the baseline water-alternating-gas (WAG) and surfactant-alternating-gas (SAG) are shown in Figure 3 and are discussed below.

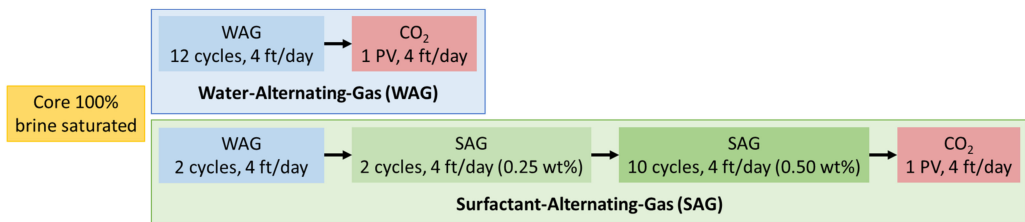


Figure 3. Experimental injection sequence for the baseline water-alternating-gas (WAG) and the surfactant-alternating-gas (SAG). The core was initially 100% saturated with brine and all injection rates were 4 ft/day. Individual WAG or SAG cycles injected 0.25 pore volumes (PV).

4.1. Baseline Water Alternating Gas (WAG)

The core was initially 100% saturated with brine by injecting brine at a low rate for five pore volumes (PV). The WAG injection was then conducted by injecting alternating slugs of brine and CO₂ at an injection rate of 4 ft/day. One brine slug and one CO₂ slug comprised one complete WAG cycle. The WAG injection procedure first injected brine for 0.10 PV. Next, the first CO₂ slug was injected for 0.15 PV to achieve the targeted 0.60 gas fraction. The WAG injection procedure was repeated until 12 complete WAG cycles were injected. Continuous CO₂ was then injected for 1 PV to study foam dry-out.

4.2. Surfactant Alternating Gas (SAG)

The core was initially 100% saturated with brine by injecting brine at a low rate for 5 PV. An initial 2-cycle WAG was conducted, followed by a diluted 2-cycle SAG and finally a 10-cycle SAG with 0.50 wt% surfactant solution. Pure CO₂ was injected at the end of the experiment for 1 PV. All injection rates were 4 ft/day at a gas fraction of 0.60, identical to the baseline WAG injection.

5. Modeling Methods

A single injection well radial reservoir simulation model was set up to investigate foam generation, strength, and propagation during the field pilot. The objective was to tune the foam model to match the simulated BHP to the observed BHP from the foam pilot. In addition, the sensitivity of foam model parameters on foam generation and propagation were studied. Previous simulation studies with the radial model have also been reported elsewhere [25]. The radial model was based upon a sector scale model that was history matched to the historical water and CO₂ injection periods in East Seminole Field [26].

The radial grid was composed of 560 active grid cells with 28 layers in the z-direction (Figure 4). Cell thicknesses, permeabilities, porosities and saturations were derived from the last step of the history matched sector model. The radial grid was centered around the pilot injection well and grid cell sizes increased logarithmically from the injector to a total of 700 ft. The radial model parameters are shown in Table 3. A commercially available conventional finite-difference compositional reservoir simulator was used for all simulations (ECLIPSE 300). The compositional model utilized the Peng–Robinson (PR) equation of state (EoS) model with six components that were tuned to PVT data. The model included two C7+ components where the lighter components were lumped as CO₂, N₂ + C1, H₂S + C2 + C3, C4 + C5 + C6. Two aqueous phases were included in the model, one for water and one for surfactant. See [26] for a complete description of the fluid model.

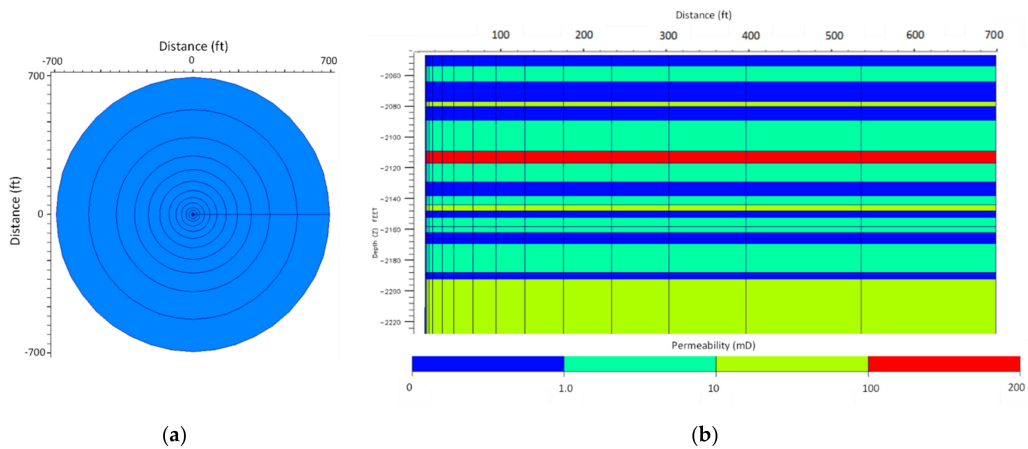


Figure 4. (a) Top view of the radial model. The injection well was placed in the center of the grid. (b) Permeability distribution of a 2D slice ($r-z$) of the radial simulation model. Properties were derived from the last step of the history matched sector model.

Table 3. Radial model properties.

Parameter	Value
Grid Dimensions (r, θ, z)	$20 \times 1 \times 28$
Outer Radius	700 ft
Total Thickness	145 ft
Initial Water saturation	0.50
Initial Reservoir Pressure	3118 psig
Reservoir Temperature	104 °F
Average Permeability	13.5 mD
Average Porosity	0.08

5.1. Foam Modeling

Foam was modeled with an implicit texture local-equilibrium (LE) model. LE foam models represent the effect of bubble size implicitly by introducing factors for reducing gas mobility by foam as a function of water saturation, oil saturation, surfactant concentration and shear-thinning due to flow rate [27,28]. LE models assume foam is present anywhere gas and water are present along with adequate surfactant concentration.

The decrease in gas mobility during foam floods is accounted for in LE models by scaling the gas relative permeability in the absence of foam (k_{rg}^{nf}) by a mobility reduction factor (FM), whereas the water relative permeabilities remain unchanged.

$$k_{rg}^f = k_{rg}^{nf} \times FM. \quad (2)$$

The effect of water saturation, shear rate, surfactant concentration and oil saturation on mobility reduction factor was modeled, given by the expression:

$$FM = \frac{1}{1 + f_{mmb} \times F_{water} \times F_{shear} \times F_{oil} \times F_{surf}}, \quad (3)$$

where f_{mmb} refers to the maximum gas mobility reduction that can be achieved. Below are the equations for F_{water} , F_{shear} , F_{oil} and F_{surf} which capture the water saturation, shear rate, oil saturation and surfactant concentration dependence, all lying in the range of 0 to 1.

The reduction of gas mobility due to the presence of water is defined as:

$$F_{water} = 0.5 + \frac{\alpha \tan[\text{epdry}(S_w - \text{fmdry})]}{\pi}. \quad (4)$$

The capillary number, N_c , describes the relative effect of capillary and viscous forces.

$$F_{shear} = \begin{cases} \left(\frac{\text{fncap}}{N_c}\right)^{\text{epcap}} & \text{if } N_c > \text{fncap} \\ 1 & \text{otherwise} \end{cases}. \quad (5)$$

The individual reduction by surfactant concentration indicates that low surfactant concentrations and weak foam results in a low F_{surf} , while higher surfactant concentrations result in a higher individual mobility reduction.

$$F_{surf} = \left(\frac{C_s}{C_s^r}\right)^{\text{epsurf}}, \quad (6)$$

where C_s is defined as the surfactant concentration, C_s^r is the surfactant concentration reference and epsurf indicated the rate change when $C_s = C_s^r$.

$$F_{oil} = \left(1 - \frac{S_o}{\text{fmoil}}\right)^{\text{epoil}}. \quad (7)$$

Foam model parameters (fmmob , fmdry and epdry) were obtained by fitting the empirical foam model to foam quality scan data through curve fitting regression [13,29]. The base values for fncap and epcap were obtained by fitting the empirical foam model to rate scan data, assuming fmmob , fmdry and epdry to be invariable for regression. Figure 5 shows the model fit to a foam quality and rate scan conducted on a reservoir core at 2500 psi and 104F. The complete experimental procedure for foam quality and rate scans is given in [30].

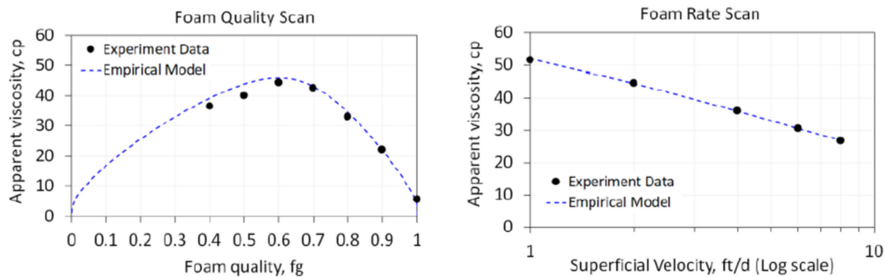


Figure 5. Foam quality scan (left) and foam rate scan (right) for the base case foam model. The empirical foam model (dashed lines) was fit to experimental data (black dots). Modified from [30].

The surfactant selected for the pilot had very low adsorption on the reservoir rock. Therefore, surfactant adsorption was not included in the model. The critical micellar concentration (CMC) was 0.01 wt% (0.035 lb/bbl) for the selected surfactant. The minimum concentration for foam generation was set at CMC, and the reference concentration for transition from weak to strong foam was assumed five times the CMC. The base value of fmsurf was therefore set as 0.05 wt% (0.175 lb/bbl). Due to unavailability of data to characterize the steepness in the change of mobility reduction due to surfactant concentration, the base value of epsurf was assumed 1. Based upon earlier CO₂ foam EOR experiments, the maximum oil saturation above which foam ceased to exit (fmoil) was 0.28 [18]. Due to unavailability of data to characterize the steepness in the change of mobility reduction due to oil saturation, the base value of epoil was assumed 1. To model foam dry-out during an SAG process near the injection well, the grid cells connected to the injector were assigned an fmmob of 0. This allowed modeling of a no foam region within a radius of 20 ft around injector to mimic foam dry out near the well.

5.2. Model Initialization

The model was initialized from the last step of the history matched sector model. The simulated injection schedule was identical to the observed injection from the pilot. Figure 6 shows an illustration of the injection schedule. Blue bars correspond to water injection, red to CO₂, and green to surfactant solution injection. The black bars indicate periods of observed field shutdowns that were also included in the simulation schedule. The pre-pilot period (1 April 2019–23 May 2019) included both the historical water injection and CO₂ injection periods. The pilot period (24 May 2019–23 August 2020) was the rapid SAG injection. The post-pilot injection period consisted of a one cycle WAG and then continuous water injection. The model did not capture the effect of nearby production wells on injection BHP because the model contained only the injection well.

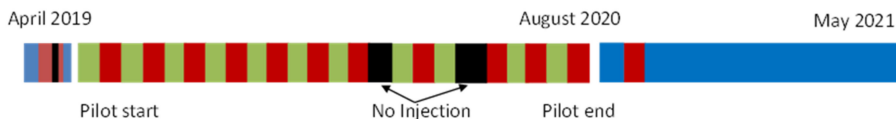


Figure 6. Injection overview of the radial model for East Seminole Field. Water injections (blue), CO₂ injections (red), surfactant injections (green), no injection periods (black).

5.3. Baseline Water Alternating Gas (WAG and Base Case Surfactant Alternating Gas (SAG)

A water-alternating-gas (WAG) case was set up to establish a baseline and to determine the CO₂ relative permeability reduction in a WAG process. The baseline WAG case injected only brine (no surfactant) and CO₂ at the targeted gas fraction of 0.70. The injection strategy consisted of 11 complete WAG cycles with alternating slugs of CO₂ for 20 days and water for 10 days. The simulation was run in history match mode where injection rates were set to the observed values from the pilot. The simulated BHP response was compared to the base rapid SAG and to the observed pilot values. The base case SAG was identical to the baseline WAG but included a surfactant component to model foam transport. Base foam model parameters were derived from foam quality and rate scans conducted on reservoir core at reservoir temperature and pressure [30].

5.4. Foam Model Sensitivity Study

The objective of the foam model sensitivity was to investigate the impact of different experimentally derived foam models on foam generation and CO₂ mobility reduction. Injection BHP results were compared to the observed BHP data to determine which foam model best represented foam behavior at the field-scale. All foam model parameters were derived from laboratory foam quality and rate scans as described previously. Three cases were set up with different foam models for the sensitivity study. The foam model parameters are shown in Table 4.

Table 4. Foam model parameters used in the sensitivity study. Foam model 2 was used in the base case.

Model Parameter	1	2 (Base)	3
<i>fmmob</i>	41.5	192	248
<i>fndry</i>	0.595	0.40	0.313
<i>epdry</i>	35	84	46.8
<i>fmcap</i>	2.14×10^{-6}	9.00×10^{-7}	8.50×10^{-7}
<i>epcap</i>	0.87	0.59	0.71

The base foam model was used in a sensitivity study of the foam model parameter, *fmmob*. As discussed previously, *fmmob* is the maximum gas mobility reduction that can be achieved with foam. Previous modeling results have shown that this parameter has the most impact on the simulated BHP [25].

6. Results and Discussion

6.1. Experimental: Unsteady-State CO₂ Foam Corefloods

Figure 7 shows apparent viscosity versus pore volume (PV) injected for the first seven cycles (2 PVs injected) of the baseline WAG (blue curve) and the base SAG (green curve). As mentioned previously, the first two cycles for both experiments were WAG cycles which generated no foam. The fluctuation in apparent viscosity between 0 cP and 2 cP during the first two cycles of each experiment was related to reduced CO₂ relative permeability in the presence of high water saturations in a WAG process [31]. The apparent viscosity of the baseline WAG stabilized at an average of 1.66 cP with a maximum value of 2.4 ± 0.2 cP. Therefore, an apparent viscosity of 2.4 cP was used as the foam generation limit for comparison to the SAG experiment (i.e., an apparent viscosity value higher than 2.4 cP indicated foam generation). Once surfactant was injected during the third cycle of the SAG experiment, the apparent viscosity increased above the WAG baseline, indicating foam generation. The apparent viscosity of the SAG continued to increase with each subsequent cycle indicating continued foam generation and propagation into the core.

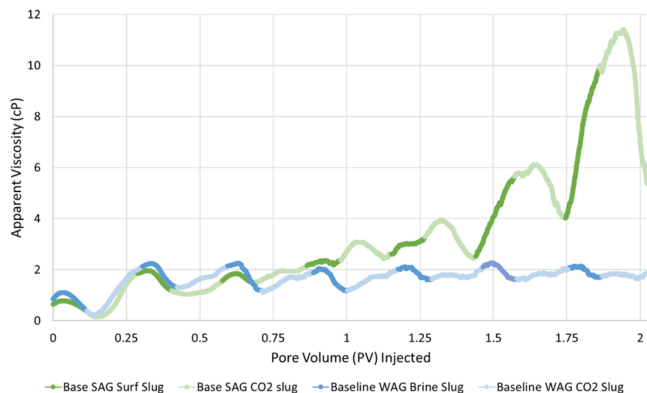


Figure 7. The first seven cycles for the Baseline WAG (blue curve) and Base SAG (green curve) experiments. Surfactant, or water, slugs are indicated with darker colors whereas the CO₂ slugs are lighter colored. The maximum apparent viscosity value of WAG is indicated with the dotted red line.

Figure 8 shows apparent viscosity versus pore volume (PV) injected for the baseline WAG (blue curve) and the base SAG (green curve) for the entire experiment. The apparent viscosity of the base SAG increased continuously from SAG cycle 4 until cycle 12, reaching a peak value of 146 ± 0.4 cP, whereas the baseline WAG had a peak apparent viscosity value of 2.4 ± 0.1 cP.

Foam is usually generated in a drainage-like process where higher capillary pressure results in a snap-off mechanism [32,33]. However, apparent viscosity also increased during surfactant injection (imbibition-like injection). This may be related to foam generation or the viscosity contrast between CO₂ and surfactant solution. The increasing apparent viscosity from cycles 3 until 12 indicated continued foam generation and propagation through the core. The final CO₂ slug was injected for 1 PV to investigate foam stability and foam dry out during a prolonged period of pure CO₂ injection. The highest apparent viscosity value was reached in this slug (146 cP) before foam collapsed due to an effective drainage process, resulting in foam dry-out.

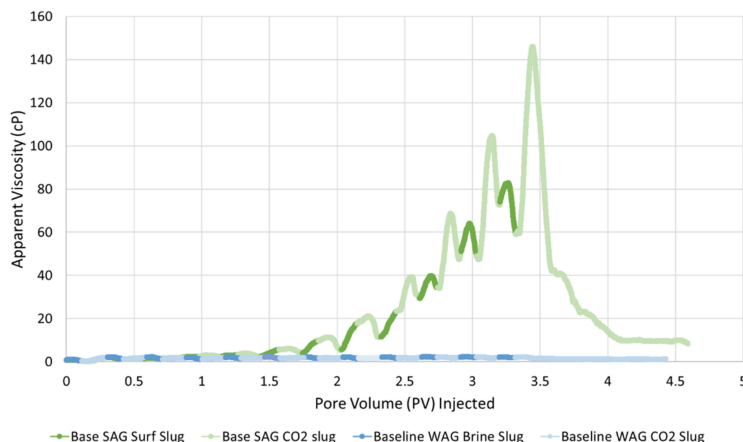


Figure 8. Apparent viscosity versus pore volume (PV) injected for 12 complete cycles for the Baseline WAG (blue curve) and the Base SAG (green curve). Surfactant solution, or water, slugs are indicated with darker colors whereas the CO₂ slugs are lighter colored.

6.2. Radial Model: Baseline WAG and Base Case SAG

The injection BHP of the baseline WAG and base case SAG simulation cases were used to evaluate foam generation and strength with surfactant present. The results were also compared to the observed BHP response from the foam pilot to determine the degree of CO₂ mobility reduction during the pilot. Figure 9 shows the simulated injection BHP through time for the baseline WAG (blue curve) and the base case SAG (green curve). The observed BHP is shown as the black circles. As discussed earlier, the injection well was run in history match mode at a set injection rate that was consistent with the observed injection rate.

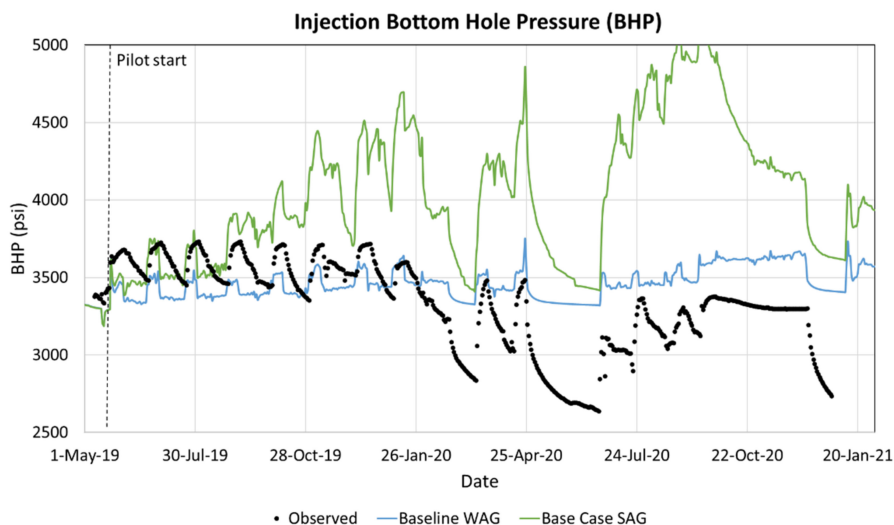


Figure 9. Injection bottom hole pressure (BHP) through time for the baseline WAG (blue curve) and the base case SAG (green curve). The observed BHP is shown as the black circles.

The simulated BHP values for the base case SAG (Figure 9, green curve) were higher than the baseline WAG (Figure 9, blue curve), indicating that foam was generated with surfactant present. Foam generation was also confirmed during the pilot based upon the higher observed BHP values compared to the baseline WAG [21]. However, the base case SAG's BHP values were significantly higher than the observed BHP, especially after the fourth SAG cycle. This suggests that the foam generated during the pilot was not as strong as in laboratory studies as also observed in [25]. In addition, the simulated BHP did not match the observed pressure fall-off after the seventh cycle because the model did not capture the effect of nearby production wells on injection BHP. As mentioned previously, the model contained only the injection well and did not include production that was observed in the field. The increase in BHP during surfactant solution slugs and subsequent decrease during CO₂ slug injection may be related to the viscosity difference between CO₂ and surfactant solution at these conditions. However, it may also be related to increased CO₂ injectivity due to water displacement in the near well area during CO₂ injection [34]. Indeed, the decreased BHP during CO₂ slugs, compared to surfactant solution slugs, at the same injection rates, increased CO₂ injectivity.

6.3. Foam Model Sensitivity Study

The foam model sensitivity study investigated the impact of different experimentally derived foam models on foam generation and CO₂ mobility reduction. Figure 10 shows the injection BHP for the simulation cases with three different experimentally derived foam models. See Table 4 for an overview of the foam model parameters.

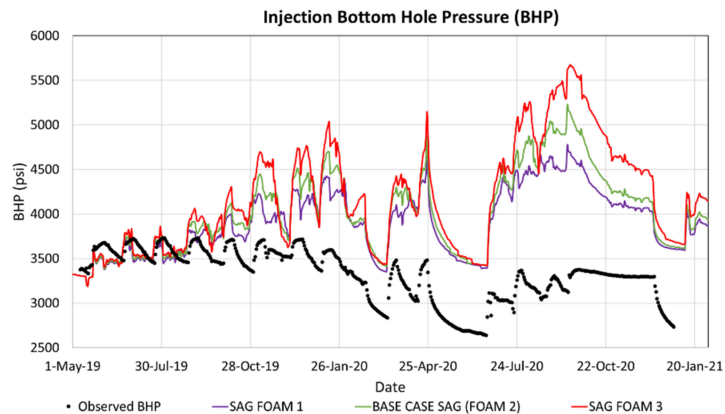


Figure 10. Injection bottom hole pressure (BHP) through time for the foam model sensitivity study. The red curve used foam model 1, the green curve is the base case SAG with foam model 2, and the purple curve used foam model 3. The observed BHP is shown as the black circles.

All three experimentally derived foam models generated foam which reduced CO₂ mobility and propagated foam into the reservoir based upon the increasing pressure build-up for each SAG cycle. Foam model 3 (Figure 10, red curve), with the highest value of *fmmob* generated the strongest foam whereas foam model 1 (Figure 10, purple curve), with the lowest *fmmob* value, generated the weakest foam relative to other cases. Thus, the most significant foam model parameter impacting injection BHP in the studied cases was *fmmob*. It was determined that the base case foam model *fmmob* parameter would be tuned to the observed BHP data to shed light on field-scale foam generation and propagation observed during the pilot. Figure 11 shows the injection BHP for the base foam model with the tuned *fmmob* value. The tuned foam model is shown at right.

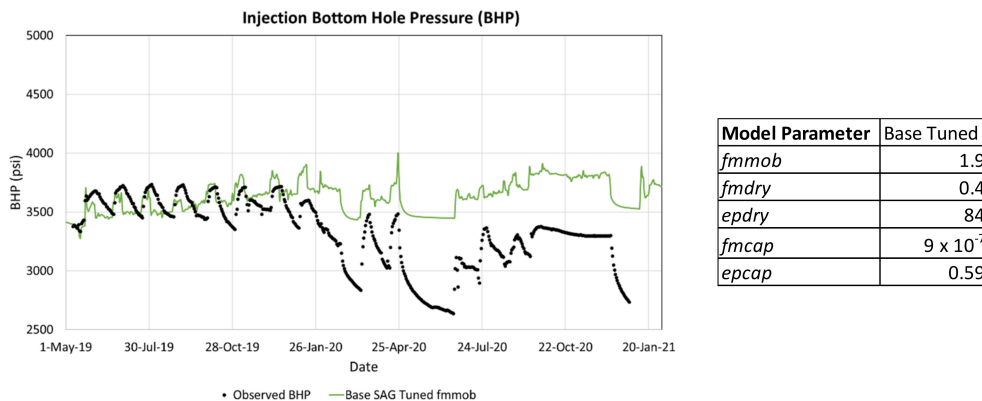


Figure 11. Injection bottom hole pressure (BHP) through time for the tuned base foam model (green curve). The observed BHP is shown as the black circles.

Reducing the *fmmob* value of the base case foam model brought the simulated BHP in closer agreement with the observed BHP response (Figure 11, black circles). Therefore, this case was used to evaluate field-scale foam propagation during the pilot. Figure 12 shows the simulated foam concentration in a 2D slice (*r-z*) of the radial model from before the pilot (Figure 12a), after the 1st SAG cycle (Figure 12b), after the 5th SAG cycle (Figure 12c), and after the 11th (final) SAG cycle (Figure 12d). Injection was from left to right in each figure. The permeability distribution is shown Figure 4b.

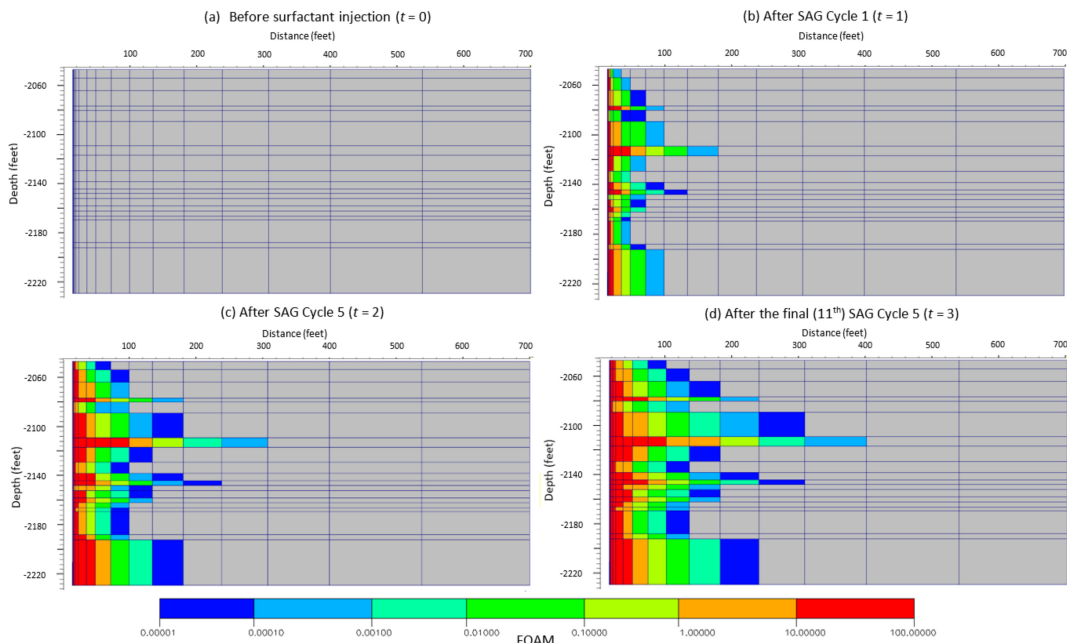


Figure 12. Foam concentration in a 2D slice (*r-z*) of the radial simulation model from (a) before surfactant injection, (b) after the 1st surfactant-alternating-gas (SAG) cycle, (c) after the 5th SAG cycle, and (d) after the 11th (final) SAG cycle. Injection was from left to right in each figure.

Figure 12b shows that foam propagated nearly 200 ft through the highest permeability layer after injection of the first SAG cycle. Foam continued to propagate as SAG injection continued, reaching a peak distance of 400 ft from the injection well (Figure 12d). Foam propagation distance was directly linked to permeability, with the highest permeability layers propagating foam the furthest. Foam more readily generates and propagates in higher permeability layers due to decreased capillary pressure.

7. Conclusions

This work presented a multiscale experimental and numerical investigation of CO₂ foam mobility control. CO₂ foam generation, strength, and propagation were evaluated at the core-scale at reservoir conditions and in a field-scale radial simulation model representing a recently completed CO₂ foam field pilot. The main objective of the experimental work was to evaluate foam generation, strength, and propagation during unsteady-state surfactant-alternating-gas (SAG) injection at reservoir conditions. The SAG injection rapidly generated foam upon the introduction of surfactant into the system. The apparent viscosity of the SAG continually increased with each subsequent SAG cycle indicating continued foam generation and propagation into the core. During a period of prolonged CO₂ injection, after SAG injection, the highest apparent viscosity value was reached before foam was destroyed in an effective drainage process, resulting in foam dry-out. Overall, the maximum apparent viscosity of the SAG was 146 cP, whereas the maximum apparent viscosity of an identical water-alternating-gas (without surfactant) injection was 2.4 cP. The laboratory methodology captured unsteady-state CO₂ foam flow and sheds light on field-scale CO₂ foam flow.

The radial reservoir simulation model investigated foam generation, strength, and propagation during a recently completed field pilot. The objective was to tune the model to match the observed bottom hole pressure (BHP) data from the foam pilot. The simulated BHP values for the base case SAG were higher than the baseline WAG, indicating that foam was generated with surfactant present. However, the base case SAG's simulated BHP values were significantly higher than the observed BHP from the pilot. This suggests that the foam generated during the pilot was not as strong as observed in laboratory studies. The foam model sensitivity study investigated the impact of different experimentally derived foam models on foam generation and strength. The most significant foam model parameter impacting injection BHP in the studied cases was the reference mobility reduction factor (*f_{nmob}*). A reasonable match was achieved by tuning the reference mobility reduction factor. The model included a method to capture foam dry-out in the near wellbore region and indicated that foam had propagated approximately 400 ft from the injection well, more than halfway to the nearest producer, at the end of pilot injection.

Author Contributions: Conceptualization, Z.P.A.; methodology, Z.P.A., A.S. and M.K.; investigation, Z.P.A., A.S. and M.K.; writing—original draft preparation, Z.P.A.; writing—review and editing, A.S., M.K. and A.G.; supervision, Z.P.A. and A.G.; funding acquisition, Z.P.A. and A.G. All authors have read and agreed to the published version of the manuscript.

Funding: This research was funded by The Norwegian Research Council project number 249742.

Institutional Review Board Statement: Not applicable.

Acknowledgments: The authors acknowledge industry partners: Shell Global Solutions, TOTAL E&P USA, Equinor ASA and Occidental Petroleum. The authors also thank the field operator.

Conflicts of Interest: The authors declare no conflict of interest.

Nomenclature

f_g	Gas fraction or foam quality
ft	Feet
cP	Centipoise
K	Permeability
mD	Millidarcy
D	Darcy
MPa	Megapascal
Psig	Pound per square inch, gauge
rb/day	Reservoir barrels per day
ft/day	Foot per day
t	Time
S_{or}	Residual oil saturation, fraction of pore volume
f_{mmob}	Foam model, maximum gas mobility reduction factor
f_{mdry}	Foam model parameter in Fwater
f_{pdry}	Foam model parameter in Fwater
f_{msurf}	Foam model parameter in Fsurf
f_{psurf}	Foam model parameter in Fsurf
f_{mcap}	Foam model parameter in Fshear
f_{pcap}	Foam model parameter in Fshear
FM	Foam model, mobility reduction factor
k_{rg}^{nf}	Gas relative permeability with no foam

Abbreviations

CCUS	Carbon capture, utilization, and storage
CCS	Carbon capture and storage
EOR	Enhanced oil recovery
SAG	Surfactant-alternating gas
WAG	Water-alternating gas
DHPG	Down-hole pressure gauge
BHP	Bottom hole pressure
wt%	Weight percentage
IWTT	Interwell CO ₂ tracer test
HCPV	Hydrocarbon pore volume

References

- Bernard, G.G.; Holm, L.W.; Harvey, C.P. Use of Surfactant to Reduce CO₂ Mobility in Oil Displacement. *SPE J.* **1980**, *20*, 281–292. [[CrossRef](#)]
- Blaker, T.; Aarra, M.G.; Skauge, A.; Rasmussen, L.; Celius, H.K.; Martinsen, H.A.; Vassenden, F. Foam for gas mobility control in the Snorre field: The FAWAG project. *SPE Reserv. Eval. Eng.* **2002**, *5*, 317–323. [[CrossRef](#)]
- Enick, R.M.; Olsen, D.K.; Ammer, J.R.; Schuller, W. Mobility and Conformance Control for CO₂ EOR via Thickeners, Foams, and Gels—A Literature Review of 40 Years of Research and Pilot Tests; SPE-154122-MS. In Proceedings of the SPE Improved Oil Recovery Symposium, Tulsa, OK, USA, 14–18 April 2012. [[CrossRef](#)]
- Føyen, T.; Brattekkås, B.; Fernø, M.A.; Barrabino, A.; Holt, T. Increased CO₂ storage capacity using CO₂-foam. *J. Greenh. Gas Control* **2020**, *96*, 103016. [[CrossRef](#)]
- Falls, A.H.; Hirasaki, G.J.; Patzek, T.W.; Gauglitz, D.A.; Miller, D.D.; Ratulowski, T. Development of a Mechanistic Foam Simulator: The Population Balance and Generation by Snap-Off. *SPE Res. Eng.* **1988**, *3*, 884–892. [[CrossRef](#)]
- Rossen, W.R. Foams in Enhanced Oil Recovery. In *Foams Theory, Measurements, and Applications*; Prud'homme, R.K., Khan, S.A., Eds.; Marcel Dekker, Inc.: New York, NY, USA, 1996; Volume 57, Chapter 11; pp. 414–464.
- Friedmann, F.; Jensen, J.A. Some Parameters Influencing Formation and Propagation of Foam in Porous Media. In Proceedings of the SPE California Regional Meeting, Oakland, CA, USA, 2–4 April 1986. [[CrossRef](#)]
- Rossen, W.R.; Gauglitz, P.A. Percolation Theory of Creation and Mobilization of Foam in Porous Media. *AIChE J.* **1990**, *36*, 1176. [[CrossRef](#)]
- Ashoori, E.; Marchesin, D.; Rossen, W.R. Roles of transient and local equilibrium foam behavior in porous media: Traveling wave. *Colloids Surf. A Physicochem. Eng. Asp.* **2011**, *377*, 228–242. [[CrossRef](#)]
- Holm, L.W.; Garrison, W.H. CO₂ Diversion with Foam in an Immiscible CO₂ Field Project. *SPE Res. Eng.* **1988**, *3*, 112–118. [[CrossRef](#)]
- Huh, D.G.; Handy, L.L. Comparison of Steady and Unsteady-State Flow of Gas and Foaming Solution in Porous Media. *SPE Res. Eng.* **1989**, *4*, 77–84. [[CrossRef](#)]

12. Castillo, R.O.S. Scale up of Surfactant Alternating Gas Foam Processes. Ph.D. Thesis, Delft University of Technology, Delft, The Netherlands, 2019. [\[CrossRef\]](#)
13. Ma, K.; Lopez-Salinas, J.L.; Puerto, M.C.; Miller, C.A.; Biswal, S.L.; Hirasaki, G.J. Estimation of Parameters for the Simulation of Foam Flow through Porous Media. Part 1: The Dry-Out Effect. *Energy Fuels* **2013**, *27*, 2363–2375. [\[CrossRef\]](#)
14. Hoefner, M.L.; Evans, E.M. CO₂ Foam: Results from Four Developmental Field Trials. *SPE Res. Eng.* **1995**, *10*, 273–281. [\[CrossRef\]](#)
15. Chou, S.I.; Vasicek, S.L.; Pisio, D.L. CO₂ Foam Field Trial at North Ward-Estes. In Proceedings of the SPE Annual Technical Conference and Exhibition, Washington, DC, USA, 4–7 October 1992. [\[CrossRef\]](#)
16. Shan, D.; Rossen, W.R. Optimal Injection Strategies for Foam IOR. *SPE J.* **2004**, *9*, 132–150. [\[CrossRef\]](#)
17. Leeftink, T.N.; Latooi, C.A.; Rossen, W.R. Injectivity errors in simulation of foam EOR. *J. Petrol. Sci. Eng.* **2015**, *126*, 26–34. [\[CrossRef\]](#)
18. Alcorn, Z.P.; Fredriksen, S.B.; Sharma, M.; Rognmo, A.U.; Føyen, T.L.; Fernø, M.A.; Graue, A. An Integrated CO₂ Foam EOR Pilot Program with Combined CCUS in an Onshore Texas Heterogeneous Carbonate Field. *SPE Res. Eval. Eng.* **2019**, *22*, 1449–1466. [\[CrossRef\]](#)
19. Jian, G.; Puerto, M.C.; Wehowsky, A.; Dong, P.; Johnston, K.P.; Hirasaki, G.J. Static Adsorption of an Ethoxylated Nonionic Surfactant on Carbonate Minerals. *Langmuir* **2016**, *32*, 10244–10252. [\[CrossRef\]](#) [\[PubMed\]](#)
20. Jian, G.; Alcorn, Z.P.; Zhang, L.M.; Biswal, L.S.; Hirasaki, G.; Graue, A. Evaluation of a Nonionic Surfactant Foam for CO₂ Mobility Control in a Heterogeneous Carbonate Reservoir. *SPE J.* **2020**, *25*, 3481–3493. [\[CrossRef\]](#)
21. Alcorn, Z.P.; Sharma, M.; Fredriksen, S.B.; Rognmo, A.U.; Fernø, M.A.; Graue, A. CO₂ Foam Field Pilot Test for EOR and CO₂ Storage in a Heterogeneous Carbonate Reservoir: Operational Design, Data Collection and Pilot Monitoring Program. In Proceedings of the 80th EAGE Annual Conference and Exhibition, Copenhagen, Denmark, 11–14 June 2018. [\[CrossRef\]](#)
22. Alcorn, Z.P.; Karakas, M.; Graue, A. CO₂ Foam Pilot in a Heterogeneous Carbonate Reservoir: Analysis and Results. In Proceedings of the SPE Improved Oil Recovery Conference, Virtual, 25–28 April 2022. [\[CrossRef\]](#)
23. Al-Menhali, A.; Krevor, S. The Impact of Crude Oil Induced Wettability Alteration on Remaining Saturations of CO₂ in Carbonates Reservoirs: A Core Flood Method. In Proceedings of the 2016 SPE Europec featured at 78th EAGE Conference and Exhibition, Vienna, Austria, 30 May–2 June 2016.
24. Jones, S.A.; Laskaris, G.; Vincent-Bonnieu, G.; Farajzadeh, R.; Rossen, W.R. Surfactant Effect on Foam: From Core Flood Experiments to Implicit-Texture Foam-Model Parameters. In Proceedings of the SPE Improved Oil Recovery Conference, Tulsa, OK, USA, 11–13 April 2016.
25. Karakas, M.; Alcorn, Z.P.; Graue, A. Pressure Measurements for Monitoring CO₂ Foam Pilots. *Energies* **2022**, *15*, 3035. [\[CrossRef\]](#)
26. Sharma, M.; Alcorn, Z.; Fredriksen, S.; Fernø, M.; Graue, A. Numerical Modeling Study for Designing CO₂-foam Field Pilot. In Proceedings of the IOR 2017—19th European Symposium on Improved Oil Recovery, Stavanger, Norway, 24 April 2017.
27. Cheng, L.; Reme, A.; Shan, D.; Coombe, D.; Rossen, W. Simulating Foam Processes at High and Low Foam Qualities. In Proceedings of the SPE/DOE Improved Oil Recovery Symposium, Tulsa, OK, USA, 3 April 2000.
28. Farajzadeh, R.; Andrianov, A.; Krastev, R.; Hirasaki, G.; Rossen, W. Foam–oil interaction in porous media: Implications for foam assisted enhanced oil recovery. *Adv. Colloid Interface Sci.* **2012**, *183–184*, 1–13. [\[CrossRef\]](#) [\[PubMed\]](#)
29. Sharma, M.; Alcorn, Z.P.; Fredriksen, S.B.; Fernø, M.A.; Skjæveland, S.; Graue, A. Model Calibration for Forecasting CO₂-Foam EOR Field Pilot Performance in a Carbonate Reservoir. *Pet. Geosci.* **2020**, *26*, 141–149. [\[CrossRef\]](#)
30. Rognmo, A.U.; Fredriksen, S.B.; Alcorn, Z.P.; Sharma, M.; Føyen, T.; Eide, G.A.; Fernø, M. Pore-to-Core EOR Upscaling for CO₂ Foam for CCUS. *SPE J.* **2019**, *24*, 2793–2803. [\[CrossRef\]](#)
31. Lake, L.W. *Enhanced Oil Recovery*; Society of Petroleum Engineers: Richardson, TX, USA, 2010.
32. Chou, S.I. Conditions for Generating Foam in Porous Media. In Proceedings of the SPE Annual Technical Conference and Exhibition, Dallas, TX, USA, 6–9 October 1991.
33. Ransohoff, T.C.; Radke, C.J. Mechanisms of Foam Generation in Glass-Bead Packs. *SPE Res. Eng.* **1988**, *3*, 573–585. [\[CrossRef\]](#)
34. Patzek, T.W. Field Applications of Steam Foam for Mobility Improvement and Profile Control. *SPE Res. Eng.* **1996**, *11*, 79–86. [\[CrossRef\]](#)



Graphic design: Communication Division, UIB / Print: Skjipes Kommunikasjon AS



uib.no

ISBN: 9788230847176 (print)
9788230849866 (PDF)